2017

Advanced liquid crystal displays with supreme image qualities

Haiwei Chen
University of Central Florida

ADVANCED LIQUID CRYSTAL DISPLAYS WITH SUPREME IMAGE QUALITIES

by

HAIWEI CHEN
B.S. Beihang University, 2013

A dissertation submitted in partial fulfillment of the requirements
for the degree of Doctor of Philosophy
in the College of Optics and Photonics
at the University of Central Florida
Orlando, Florida

Fall Term
2017

Major Professor: Shin-Tson Wu

ABSTRACT

Several metrics are commonly used to evaluate the performance of display devices. In this dissertation, we analyze three key parameters: fast response time, wide color gamut, and high contrast ratio, which affect the final perceived image quality. Firstly, we investigate how response time affects the motion blur, and then discover the 2-ms rule. With advanced low-viscosity materials, new operation modes, and backlight modulation technique, liquid crystal displays (LCDs) with an unnoticeable image blur can be realized. Its performance is comparable to an impulse-type display, like cathode ray tube (CRT). Next, we propose two novel backlight configurations to improve an LCD's color gamut. One is to use a functional reflective polarizer (FRP), acting as a notch filter to block the unwanted light, and the other is to combine FRP with a patterned half-wave plate to suppress the crosstalk between blue and green/red lights. In experiment, we achieved 97.3% Rec. 2020 in CIE 1976 color space, which is approaching the color gamut of a laser projector. Finally, to enhance an LCD's contrast ratio, we proposed a novel device configuration by adding an in-cell polarizer between LC layer and color filter array. The CR for a vertically-aligned LCD is improved from 5000:1 to 20,000:1, and the CR for a fringe field switching LCD is improved from 2000:1 to over 3000:1. To further enlarge CR to fulfill the high dynamic range requirement, a dual-panel LCD system is proposed and the measured contrast ratio exceeds 1,000,000:1. Overall speaking, such an innovated LCD exhibits supreme image qualities with motion picture response time comparable to CRT, vivid color to laser projector, and contrast ratio to OLED. Along with other outstanding features, like high peak brightness, high resolution density, long lifetime, and low cost, LCD would continue to maintain its dominance in consumer electronics in the foreseeable future.

To my beloved family.

ACKNOWLEDGMENTS

First and foremost, I would like to express my sincerest gratitude to my Ph.D. advisor, Prof. Shin-Tson Wu. He is a visionary leader and an eminent expert in the field. Being his student is truly a great honor. During the past four years, he has been supportive and has given me the freedom to explore various projects. This is the basis and foundation to enable the high productivities in my 4-year-long Ph.D. program. In addition to that, Prof. Wu is always positive, and willing to help us out anytime for anything. He would be my first choice to go, whenever I need help or guidance. He is and will be my best role model for a scientist, mentor, and teacher.

Also, I would like to thank Prof. Wu's better-half Cho-Yan Hiseh. She is our beloved Shimu. As a student studying far from my homeland, I have felt LCD group as a big warm family, mainly thanks to the delicious food Shimu prepares for us almost every Friday.

I am also very grateful to my committee members, Prof. M. G. "Jim" Moharam, Prof. Boris Y. Zeldovich, Prof. Patrick L. LiKamWa, and Prof. Yajie Dong. They have been helpful in providing insightful discussions during my Ph.D. pursuit and invaluable advises for my candidacy, proposal and thesis preparation. Besides, they wrote strong recommendation letters for me when I applied for society awards. It is their strong support that makes my applications smooth and successful.

I am also indebted to all the LCD group members. It is my great privilege to work and study together with so many talents. They have been helpful and supportive in too many ways. First of all, a special acknowledgement goes to my office mate of many years: Dr. Fenglin Peng. She is humble, helpful and friendly. When I firstly joined LCD group, it is she who taught me the basis of LC mixtures and display devices. Also, she led me to go through multiple experiments with great patience. I greatly appreciate everything she has done for me. Then I would like to thank

Dr. Daming Xu and Dr. Zhenyue Luo. They are quite knowledgeable, from whom I learned a lot, including the valuable techniques to do LCD simulations. Besides, I would like to show my appreciation to former and present group members, particularly Prof. Minggang Hu, Dr. Yifan Liu, Ruidong Zhu, Yun-Han Lee, Guanjun Tan, Juan He, Fangwang Gou, Yuge Huang, Ziqian He, Tao Zhan, Kun Yin, Jianghao Xiong, and Md Javed Rouf Talukder. I will never forget those happy memories we created together in the last four years.

Apart from my group members, I am also very grateful to my other friends from both academia and industry. Dr. Martin Schadt is a respectable scientist, who invented the well-known twisted nematic LCDs. I feel so honored to have Martin and his wife Helga as my dear friends. We had uplifting conversations many times. Prof. Jiun-Haw Lee from National Taiwan University is another trustable friend. I know I could always ask him for advice and opinions on OLED related questions. Also, I would like to thank Dr. Nelson V. Tabiryan and Dr. Haiqing Xianyu from Beam Company. They kindly provided us a cycloidal diffractive waveplate, and offered us necessary technical guidance. Our collaborations went quite well. Also, I value the friendship and support from Prof. Yanqing Lu, Prof. Wei Hu, and Wei Duan. They have a beautiful research lab in Nanjing University. Dr. Michael Wand from LC Vision developed ultra-low viscosity LC mixtures, and we had nice collaborations on fast-response LCDs. David Wyatt from PixelDisplay has an amazing LED technology with super narrow bandwidth. Working with him is superb and filled with inspirations. Besides, I appreciate the help and teaching from Prof. Chih-Lung Lin, National Cheng Kung University, about TFT driving.

I also thank those who kindly accepted our invitations to visit us and give wonderful technical seminars when I was the president of SID student chapter in UCF. They are Dr. K. Käläntär from Japan Global Optical Solutions, Dr. Fang-Cheng Lin from National Chiao Tung

University, Dr. Jiahui Wang from Sun Yat-sen University, Prof. Liang-Chy Chien from Kent State University, Prof. Kristiaan Neyts from Ghent University, Prof. Sung Tae Shin from KyungHee University, and Dr. Michael Wittek from Merck Performance Materials. I appreciated their scientific advice and knowledge, and many insightful discussions and suggestions.

I also thank Ming-Chun Li, Daniel Lee, Yi-Fen Lan, Cheng-Yeh Tsai, Weng-Ching Tsai, Norio Sugiura, and many other engineers from AU Optronics. Their dedications and enthusiasm to developing advanced LCDs give me a lot of motivations in research.

Also, I would like to thank Victor Yin, Dr. Cheng Chen, Dr. Mark Son, Dr. Zhibing Ge, Dr. Xinyu Zhu, Dr. Young-Cheol Yang, Dr. Kay Tai, Dr. Jin Yan, Dr. Yuan Chen, and many other engineers from Apple. We had very fruitful discussions about display and many others. They have always been an inspiration on how to make things "perfect".

Lastly I would like to thank my parents, my parents-in-law, and my younger brother, for all their tremendous support and encouragement. My hard-working parents have sacrificed their lives for my brother and myself and provided unconditional love and care. I love them so much, and I would not have made it this far without them.

And most of all, I want to thank my loving, supportive and cheerful better-half Qing Xue. She has been a true and great supporter and has unconditionally loved me during my good and bad times. She let me know I always have my family to count on when times are rough. She and my family is the primary reason for me to work hard and pursue a better life.

TABLE OF CONTENTS

LIST OF FIGURES

LIST OF TABLES

CHAPTER ONE: INTRODUCTION

1.1 LCD configuration and working principle

Thin-film transistor liquid crystal displays (TFT-LCDs) are ubiquitous in our daily life; their applications span from smartphones, pads, computer screens, to TVs [1-3]. Unlike other display technologies, e.g. cathode ray tube (CRT), plasma display panel (PDP) or organic light-emitting diode (OLED), LCD is a non-emissive display, thus, a backlight unit (BLU) is mostly needed (except for reflective displays) to illuminate the display panel [4].

In general, there are two types of BLU configurations: direct-lit and edge-lit. Just as the name indicates, direct-lit backlight means the light source (i.e. an array of LED chips) is placed right behind the display panel. However, this configuration is bulky and the hot-spot issue due to separated LED illumination may arise, which degrades the backlight uniformity. In contrast, the edge-lit backlight consists of several light sources placed along the edge of display, as depicted in Figure 1.1. The incident light from LED chips passes through the light-guide plate (LGP) and is steered upward toward the LCD panel. Thanks to the thin profile of LGP, the total thickness of whole display device is reduced dramatically. Also, with a strong diffuser right above LGP (not shown here), the light uniformity is greatly enhanced.

To confine the backlight profile and boost the brightness at normal direction, a brightness enhancement film (BEF) is commonly used [5]. But the tradeoff is decreased brightness at large oblique angles. Thus, for large-sized TV applications, only single BEF is used to enable wide view at horizontal direction. Whereas for small-sized displays, like smartphones or tablets, two crossed BEFs are typically employed to maximize the normal view.

So far, the light after BEFs is mostly unpolarized. When traversing through an absorptive linear polarizer, about 50% of the light is absorbed and lost. Thus, to make full use of these lights, a reflective polarizer (or known as dual brightness enhancement film: DBEF) is commonly used to recycle the unused polarization [6]. It means light with desired polarization (say s-wave) could pass through, while another polarization (p-wave) is reflected back. With the help of DBEF, ~60% optical enhancement could be realized.

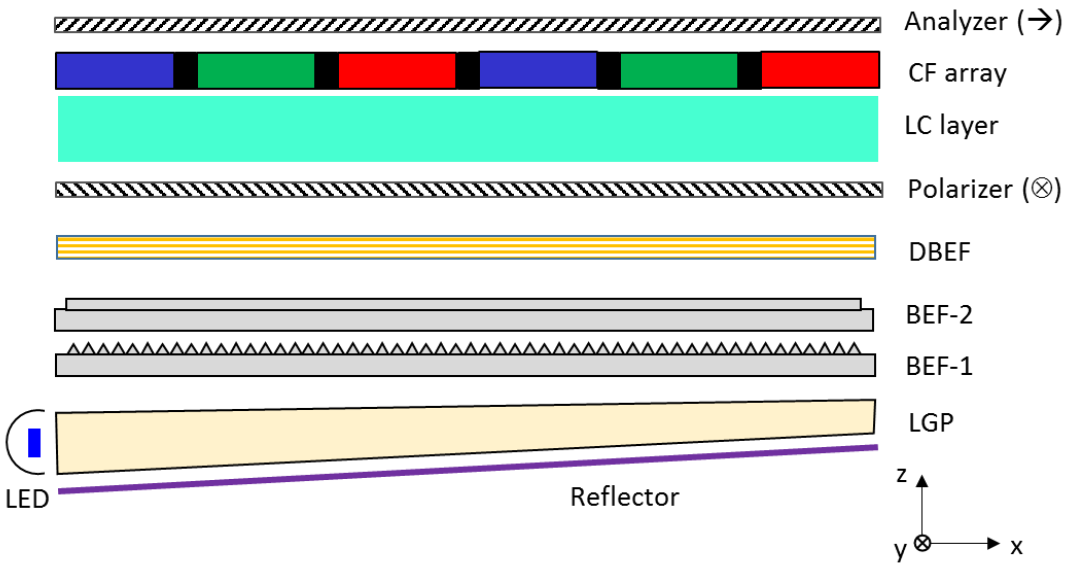

Figure 1.1. Schematic diagram of a LCD. (LGP: light guide plate; BEF: brightness enhancement film; DBEF: dual brightness enhancement film; BLU: backlight unit; TFT: thin-film transistor; LC: liquid crystal; CF: color filter)

After passing through a stack of optical sheets, the backlight then enters the LCD panel. In the panel, the liquid crystal layer is sandwiched between two crossed polarizers. By controlling the applied voltage to LC layer, transmittance could be modulated precisely. At the same time, the color filter array transmits the designated red, green and blue (RGB) primary colors, to form a color image.

Generally, LCD could be categorized into four types, depending on the molecular alignments and electrode configurations [7-10]: 1) twisted nematic (TN) mode, 2) multi-domain vertical alignment (MVA) mode, 3) in-plane switching (IPS) mode and 4) fringe-field switching (FFS) mode. All of them have their own pros and cons. For example, TN mode has simple structure, high transmittance and low cost, but its viewing angle is somewhat limited [11-14]. Thus it is mostly used in wristwatches, signage, and laptop computers, in which wide view is not absolutely necessary. For MVA mode, it shows high on-axis contrast ratio, wide viewing angle and fast response time, it is a good candidate for TVs with good image quality [15-19]. Recently, curved MVA LCD TVs are popular, as VA mode enables a smaller bending curvature as compared to other LCDs [20, 21]. While for IPS and FFS modes, they share quite similar working mechanisms [22-29]. That is, LC directors are mainly reoriented in horizontal plane, as a result, it exhibits high transmittance, wide viewing angle, weak color shift and robust to touch pressure. IPS/FFS mode finds good match for mobile displays, where low power consumption for long battery life and pressure-resistance for touch screens are critical.

1.2 Display metrics

To evaluate the performance of display devices, multiple metrics have been proposed and practiced [1], such as response time, contrast ratio, color gamut, panel flexibility, viewing angle, resolution density, peak brightness, lifetime, etc. Here, we will mainly focus on three of them: fast response time, wide color gamut, and high contrast ratio. As will be discussed later, these three metrics are the key parameters governing the final perceived image quality.

The first one is response time, which is mostly defined as the time interval between 10% and 90% transmittance difference. For a typical LCD device, its response time is around 5-10 ms,

depending on different LCD modes. However, this performance is not satisfactory, especially compared to other competing display technologies. For example, organic light-emitting diode (OLED) shows average gray-to-gray response time as fast as 0.1 ms [30]. It is almost 100x faster than LCD.

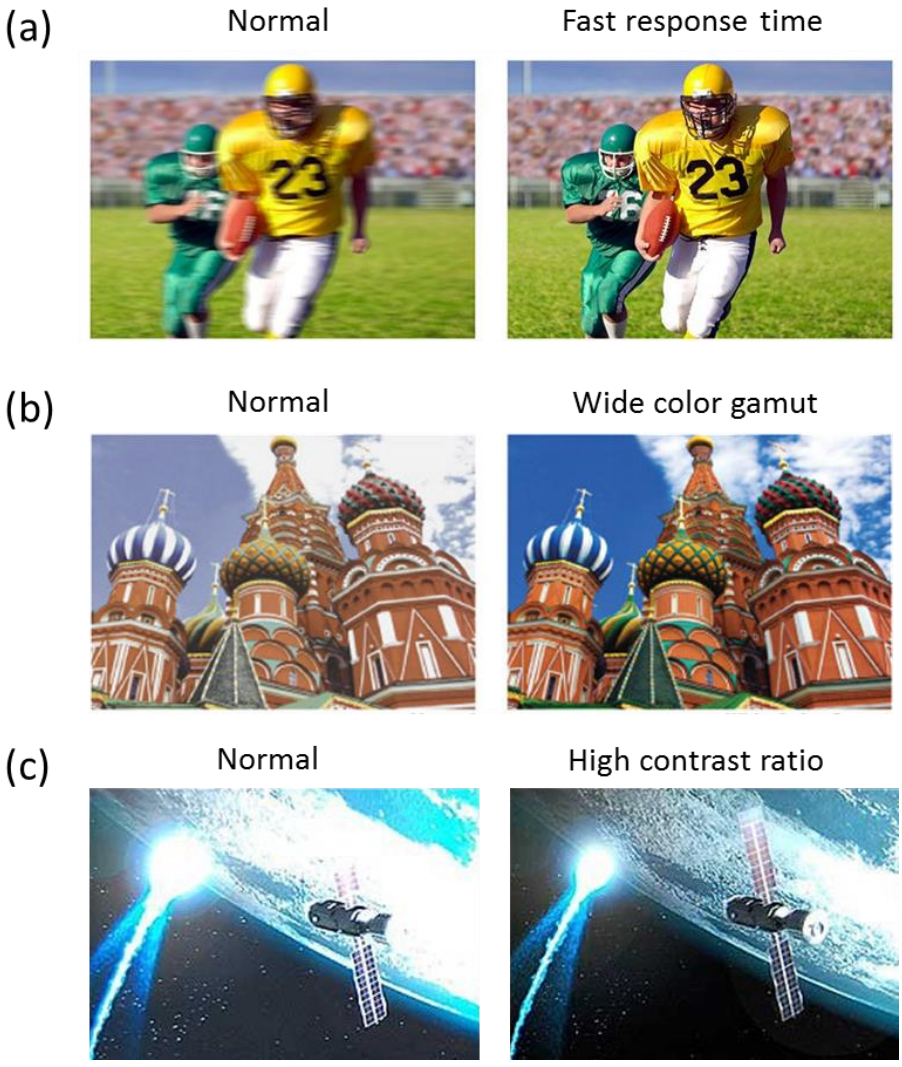

Figure 1.2. Comparison of image qualities with different (a) response time; (b) color gamut; and (c) contrast ratio.

Slow response results in a severe issue called image motion blur, as depicted in Figure 1.2(a). When displaying fast-moving objects (i.e. a running football player), the conventional LCD

is too slow to show the crisp images, or namely, the image is blurred. This will deteriorate the viewing clarity significantly. On the other hand, a fast-response display could generate sharp images, enriching the image quality with great details. As a result, improving the response time becomes an urgent need. In CHAPTER TWO, we will discuss three possible solutions using: 1) ultra-low viscosity LC mixtures; 2) single-rubbing vertical alignment fringe in-plane switching mode; and 3) high performance polymer-stabilized blue phase liquid crystal.

Color is another key metric affecting the image quality. As shown in Figure 1.2(b), displays with wider color gamut could enable more realistic viewing experience. However, for conventional LCDs employing white light-emitting diode (WLED) as backlight [31, 32], its color gamut is limited to ~70% NTSC or ~50% Rec. 2020. The reason is that WLED uses blue LED to pump YAG:Ce^{3+} yellow phosphor, whose emission spectrum is relatively broad. As a result, it cannot get highly saturated RGB primary colors.

To improve that, more advanced backlight units have been developed, including two phosphor-converted WLED (2pc-WLED) and quantum dot (QD) [33-35]. Due to the reduced bandwidth, these two light sources could provide well-separated green and red lights, leading to a much wider color gamut. More details will be presented in CHAPTER THREE. There, we will propose two novel backlight configurations to further enhance the color performance.

The last but not the least, contrast ratio (CR) is an important parameter determining the image quality. It is defined as the luminance ratio between white and black states. As shown in Figure 1.2(c), low contrast image is unable to produce the true dark state; instead, the whole background is more bluish, resulting from the annoying light leakage. Moreover, its peak brightness is limited, thus a lot of details are disguised within the white regions. Whereas for high contrast image, it exhibits noticeable improvement. In general, its black state is much darker and

white state is much brighter. As a result, abundant gray scales could be realized between these two extremes, and more details in the satellite and planet could be clearly observed.

However, for a non-emissive LCD, its CR is inherently limited. For examples, the typical CR for commercial MVA LCD TVs is only ~5000:1, and it drops to ~2000:1 and ~1000:1 for the FFS-based and TN-based LCDs, respectively [4]. To improve CR, in CHAPTER FOUR, we propose a new device structure by adding a thin in-cell polarizer between LC layer and CF array. The corresponding depolarization effect could be suppressed, leading to a much improved CR. To further enhance CR, a dual-panel LCD system is studied and demonstrated. In experiment, exceedingly high contrast ratio (> 1,000,000:1) and high bit-depth (> 14 bits) were realized at merely 5 volts.

CHAPTER TWO: FAST RESPONSE TIME

2.1 Motion picture response time

As mentioned earlier, image motion blur issue will arise as the display response is not fast enough. To characterize image blurs, motion picture response time (MPRT) has been proposed and commonly practiced [36-39], which is jointly determined by the LC (or OLED) response time, TFT frame rate, and backlight duty ratio.

Previously, calculating the MPRT of an active matrix display was rather difficult, because several effects are involved, like sample-and-hold effect, image motion, and human vision effect. But this task becomes incredibly simple, as *Peng et al.* derived an analytical equation to describe the MPRT [40, 41]:

$$MPRT = \sqrt{\tau^2 + (0.8T_f)^2}, \tag{2.1}$$

where T_f is the frame time (e.g. T_f = 16.67 ms for 60 fps). Using this equation, we can easily obtain MPRT as long as LC response time and TFT frame rate are known.

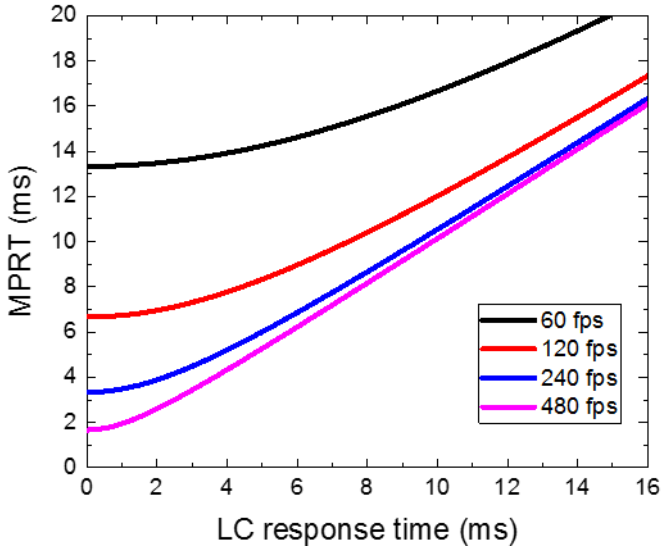

Figure 2.1. Calculated MPRT as a function of LC (or OLED) response time at different frame rates.

Figure 2.1 is a plot of simulated MPRT at different TFT frame rates. From Figure 2.1, we can get three important trends: 1) At a given frame rate, say 120 fps, as the LC response time decreases, MPRT decreases almost linearly and then gradually saturates. Note that the MPRT for $\tau = 2$ ms is only 4% longer than that of $\tau = 0$. Therefore, if an LCD's response time is 2 ms or less, then its MPRT is comparable to that of an OLED display, even if the OLED's response time is assumed to be 0. (2) As the TFT frame rate increases, the limiting MPRT (assuming $\tau = 0$) decreases linearly, because the limiting MPRT = $0.8T_f$. (3) If the LC response time is not fast enough, say $\tau = 5$ ms, then increasing the frame rate from 60 fps to 120 fps makes a big improvement in MPRT, but further increasing the frame rate to 240 fps and 480 fps the improvement is less obvious.

The first finding is extremely important, as it guides the development for future LCDs. That is, we don't need to keep pushing LC response time to 0; rather, 2 ms is good enough from the theoretical predications as shown in Figure 2.1. To achieve this goal ($\tau \leq 2$ ms), in the following sections, we will introduce three options by using 1) ultra-low viscosity LC mixtures; 2) single-rubbing vertical alignment fringe in-plane switching; and 3) high performance polymer-stabilized blue phase liquid crystal.

2.2 Fast-response VA with ultra-low viscosity LC mixtures

2.2.1 Material characterizations

In experiment, we prepared an ultra-low viscosity LC mixture with negative dielectric anisotropy ($\Delta\varepsilon < 0$), called MX-40593 [41]. Firstly, we characterized its physical properties including birefringence (Δn), visco-elastic coefficient (γ_1/K_{33}), and dielectric anisotropy.

Table 2.1. Measured physical properties of MX-40593. T = 22°C and λ = 633 nm.

Δn	$\varepsilon_{//}$	$\varepsilon_{\perp}$	$\Delta\varepsilon$	K_{33} (pN)	γ_1/K_{33} (ms/μm^2)	γ_1 (mPas)	T_c (°C)
0.098	3.41	5.88	-2.47	11.9	5.0	59.5	79.3

(a) Birefringence

Birefringence of an LC is mainly governed by the conjugation length and order parameter. To measure Δn, we filled the LC mixture into a VA test cell with cell gap d = 9.0 μm. A 1 kHz square-wave AC voltage signal was applied to the LC cell, and a He-Ne laser (λ = 633 nm) was used as the probe beam. The cell was then sandwiched between two crossed linear polarizers. By measuring the voltage dependent transmittance through LabVIEW system, we can obtain Δn easily. Detailed method has been described in [42]. From Table 2.1, the measured birefringence at room temperature is Δn = 0.098.

Next, we measured the temperature dependent birefringence. We placed the LC cell on a Linkam heating stage controlled by the temperature program (Linkam TMS94). Results are shown in Figure 2.2(a), where dots stand for measured data and solid lines for the fittings using Haller's semi-empirical equation [43]:

$$\Delta n = \Delta n_0 S = \Delta n_0 (1 - T/T_c)^{\beta}, \tag{2.2}$$

where Δn_0 is the extrapolated birefringence at T = 0K, S is the order parameter, T_c is the clearing point, and β is a material parameter. Through fitting, we obtained Δn_0 = 0.168, and β = 0.262.

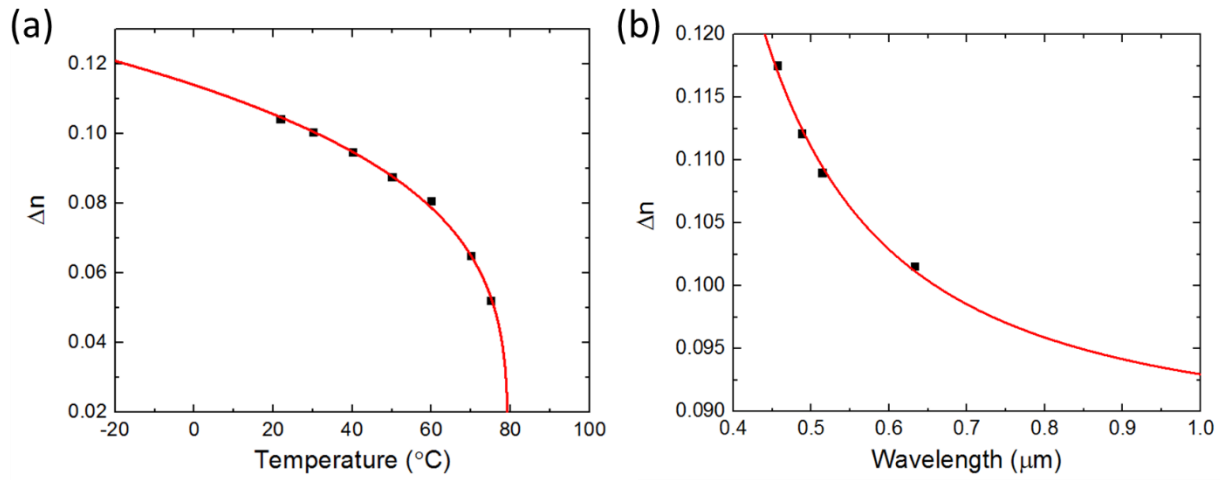

Figure 2.2. (a) Temperature dependent birefringence and (b) dispersion curve at T = 22°C of MX-40593.

Also, we measured the birefringence at different wavelengths. Results are plotted in Figure 2.2(b). Similarly, we fitted the measured Δn using a single-band dispersion equation [44]:

$$\Delta n = G\frac{\lambda^2 \cdot \lambda^{*2}}{\lambda^2 - \lambda^{*2}}, \tag{2.3}$$

where G is a proportionality constant and λ^* is the mean resonance wavelength. Good agreement is realized.

(b) Visco-elastic coefficient

In an LCD, the response time is proportional to the visco-elastic coefficient (γ_1/K_{ii}), where K_{ii} is the corresponding elastic constant depending on the LC alignment. For example, here, in a VA cell, $K_{ii} = K_{33}$ is the bend elastic constant. To measure this visco-elastic coefficient, we recorded the free relaxation (decay) process for a controlled phase change, and then γ_1/K_{33} could be extracted using the following equation [45, 46]:

$$\frac{\gamma_1}{K_{33}} = A \cdot \frac{\exp(E_a / K_B T)}{(1 - T/T_c)^{\beta}}, \tag{2.4}$$

where A is the proportionality constant, E_a is the activation energy of molecular rotation, and K_B is the Boltzmann constant. Figure 2.3 depicts the measured data (dots) and fitted curves (solid lines), from which we can tell the measured data fit quite well with Eq. (2.4).

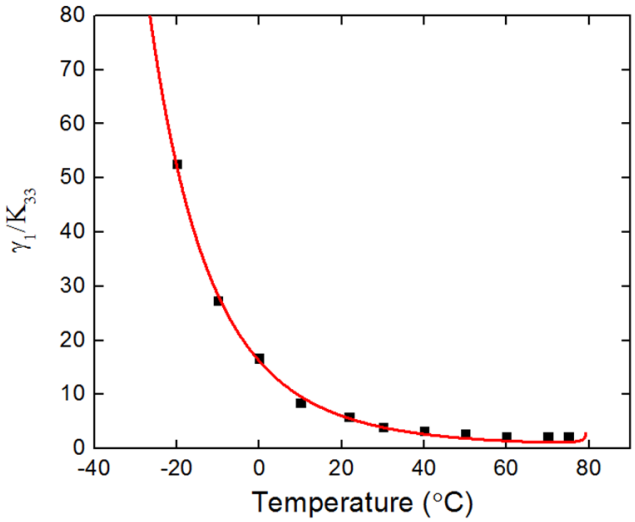

Figure 2.3. Temperature dependent visco-elastic coefficient of MX-40593.

(c) Dielectric anisotropy

Next, we measured the dielectric constants of MX-40593 using the capacitance method. Detailed procedures have been reported in Ref. [47], and the measured results are listed in Table 2.1. From Table 2.1, the $\varepsilon_{//}$ and $\varepsilon_{\perp}$ are 3.41 and 5.88, respectively, i.e., $\Delta\varepsilon$ = -2.47. Compared to the conventional negative materials used in VA mode, this $\Delta\varepsilon$ is relatively small, leading to a fairly large operation voltage. This may increase the electrical power consumption slightly.

2.2.2 Device performance

After characterizations of MX-40593, we injected this LC mixture into a commercial VA cell with cell gap d = 3.3 μm. The measured threshold voltage is 2.1 V_{rms} and peak transmittance voltage is 6.7 V_{rms} at λ = 550 nm. To study GTG response time, we divided the voltage-

transmittance curve into eight gray levels equally, and measured the response time between different gray levels. As usual, the response time is defined as the time interval between 10% and 90% transmittance. During the measurement, we applied overdrive and undershoot voltages to accelerate the transition process [48].

Table 2.2. Measured GTG response time of our VA cell with overdrive and undershoot. d = 3.3 μm, λ = 633 nm and T = 22°C.

	1	**2**	**3**	**4**	**5**	**6**	**7**	**8**
1		0.58	0.70	0.72	0.93	0.96	1.02	1.37
2	2.73		0.12	0.23	0.34	0.51	0.70	1.14
3	2.81	1.14		0.12	0.27	0.41	0.62	1.05
4	3.56	1.44	0.55		0.13	0.28	0.49	1.01
5	3.73	2.07	1.09	0.54		0.13	0.34	0.98
6	4.07	2.49	1.54	0.92	0.40		0.22	0.87
7	4.23	2.94	2.01	1.41	0.82	0.33		0.69
8	4.61	3.24	2.40	1.84	1.28	0.82	0.39	

Table 2.2 lists the obtained results. According to Table 2.2, the average GTG response time is 1.29 ms, which is 4.4X faster than the commercial product (5.69 ms) reported in Ref. [30]. Such a fast response time mainly originates from the ultra-low viscosity of our LC mixture. What's more, low viscosity implies to a low activation energy, which leads to a mild increase in response time even at low temperature, say –20°C [26].

As aforementioned discussions, the MPRT of an LCD is comparable to that of an OLED, as long as LC response is 2 ms or less. Now we have demonstrated a fast response VA LCD with

average GTG response time ~ 1.29 ms [41]. To validate the above finding, we measured the GTG MPRT using our MX-40593 at f = 120 Hz, and the results are listed in Table 2.3. The obtained average GTG MPRT is 6.88 ms at 120 Hz, while it is 6.66 ms for OLED. In other words, LCD and OLED indeed show comparable motion image blur, except some slower gray level transitions, e.g. 8 to 1.

Table 2.3. Measured GTG MPRT of our VA LCD at f = 120 Hz. d = 3.3 μm, λ = 633 nm and T = 22°C.

	1	**2**	**3**	**4**	**5**	**6**	**7**	**8**
1		6.70	6.70	6.72	6.72	6.72	6.78	6.78
2	7.16		6.68	6.70	6.70	6.72	6.74	6.78
3	7.22	6.72		6.68	6.70	6.72	6.72	6.76
4	7.72	6.76	6.68		6.68	6.70	6.72	6.76
5	7.76	6.80	6.74	6.70		6.68	6.70	6.72
6	7.84	6.86	6.82	6.72	6.70		6.68	6.72
7	7.90	7.04	6.82	6.78	6.76	6.70		6.70
8	7.96	7.28	7.00	6.82	6.96	6.92	6.86	

To reduce the MPRT, as shown in Figure 2.1, increasing the TFT frame rate is an effective approach. Presently, large-sized TVs are driven at mostly 120 fps. If we increase the TFT frame rate to 240 fps, both LCD and OLED show ~ 2X faster but still similar MPRT (3.71 ms vs. 3.34 ms), as shown in Table 2.4. LCD is a voltage-driven device, whereas OLED is current driven. Thus, LCD only needs one TFT per pixel, but OLED requires multiple TFTs per pixel [49]. For example, in some commercial OLED products, 5 TFTs are employed in one pixel to stabilize the dark current

variations. As a result, increasing the frame rate is more difficult for OLED TFT driving, but obviously it is less a burden for single-TFT driven LCD.

Table 2.4. Measured GTG MPRT of our VA LCD at f = 240 Hz. d = 3.3 μm, λ = 633 nm and T = 22°C.

	1	**2**	**3**	**4**	**5**	**6**	**7**	**8**
1		3.38	3.40	3.40	3.40	3.42	3.44	3.50
2	4.52		3.34	3.36	3.38	3.40	3.42	3.46
3	4.58	3.44		3.34	3.36	3.38	3.40	3.44
4	5.34	3.52	3.38		3.34	3.36	3.40	3.44
5	5.36	3.76	3.40	3.38		3.34	3.38	3.42
6	5.52	4.02	3.54	3.42	3.36		3.36	3.40
7	5.64	4.32	3.76	3.50	3.34	3.36		3.40
8	5.70	4.68	4.20	3.82	3.48	3.44	3.36	

2.2.3 Discussion

So far, our goal is 2 ms response time for an LCD device, to enable comparable MPRT as an OLED. This is a big milestone. However, there should be one more step further. As depicted in Figure 2.1, even if LC (or OLED) response time is 0, its MPRT is still 6.66 ms at 120 fps. This is determined by TFT sample-and-hold effect. For a cathode ray tube (CRT), it is impulse-type display, so that its MPRT could be as short as 1.5 ms. This is why image blur is not an issue for CRT. But for LCD and OLED, they are both holding-type displays, meaning brightness will maintain in the whole frame. Therefore, their MPRT will be limited by the TFT frame time [40].

To suppress image blur to unnoticeable level (MPRT < 2 ms), as discussed above, increasing frame rate is an option, but the electrical power would increase substantially. In fact, for most fast-response gaming monitors, its driving frequency is around 144 fps. Then to mitigate image blur, another approach called backlight modulation (sometimes it is called scanning backlight or blinking backlight) is mostly adopted [50-52].

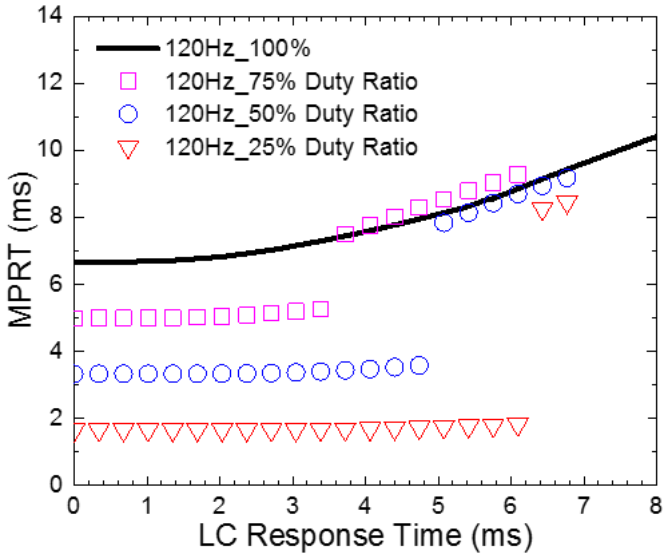

Figure 2.4. Duty ratio effects on MPRT at 120 Hz frame rate.

As plotted in Figure 2.4, the effective MPRT decreases almost linearly when the LCD backlight duty ratio decreases. For example, when the duty ratio is 50%, the effective MPRT is reduced to 3.34 ms. Then it is further reduced to < 2 ms when 25% duty ratio is employed. In fact, such an LCD with scanning backlight or blinking backlight is more like a CRT, working as an impulse-type display [53].

Also, as shown in Figure 2.4, the MRPT is less sensitive to the LC response time when duty ratio decreases. That is, MPRT is saturated within a much longer time range. For example, when there is no backlight modulation (i.e. 100% duty ratio), the saturation of MPRT occurs at LC response time < 2 ms. But this time is lengthened to ~ 5 ms at 50% duty ratio. Under such a

condition, the requirement on LC response time is much relaxed. However, the major tradeoff for the lower duty ratio is reduced brightness. One way to compensate for the lost brightness is to boost the current of the LED backlight.

Another thing worth mentioning here is for the proposed fast-response VA, we only focus on the average GTG response time. In fact, for some grayscale transitions, like 8 to 1, it is still more than twice slower than the requirement (4.61 ms vs. 2 ms). This may introduce image motion blur for fast-moving objects. Thus, advanced materials and device structures with faster response for all the grayscale transitions are urgently needed.

2.3 Fast-response vertical alignment fringe in-plane switching mode

Recently, vertical alignment fringe in-plane switching (VA-FIS) mode was proposed and fast response was obtained even at -30°C [54]. Its driving scheme is simple and there is no TFT charging issue. But the trade-offs are twofold: increased operation voltage and decreased transmittance. Here, we modify this VA-FIS mode by removing the bottom alignment layer. Such a structure helps to increase the transmittance and reduce the operation voltage significantly. Meanwhile, sub-millisecond response time is realized. To achieve good dark state, we can apply a small biased voltage to the common electrode at bottom substrate.

2.3.1 Structure design

Figure 2.5 depicts the schematic diagram of proposed single-rubbing VA-FIS mode. As the name indicates, there is only one alignment layer on the top glass substrate, which induces vertical alignment at voltage-off state. Meanwhile, on the top substrate, there is a planar electrode with a fixed voltage (or biased voltage V_{bias}). Combined with the bottom common electrode (V_{com} = 0), a strong vertical electric field is produced in the whole panel. This has two effects: 1) LC

directors are vertically aligned along the electric field, leading to a high contrast ratio; 2) the LC directors are pulled back by the longitudinal field to their initial state when the horizontal electric field is removed, leading to a fast decay time.

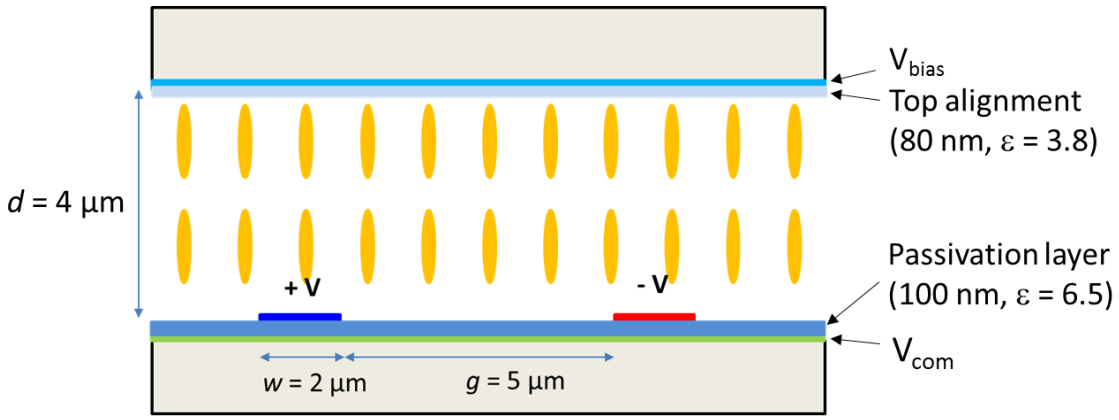

Figure 2.5. Schematic diagram of the proposed single-rubbing VA-FIS mode.

For the interdigitated pixel electrodes on the bottom substrate, the applied voltages are in different polarities, thus, the strength of horizontal electric field is doubled. This structure is called fringe in-plane switching (FIS) mode [55], since fringe electric field and in-plane electric field coexist. However, it requires 2 TFTs so that the aperture ratio would be reduced slightly.

2.3.2 Simulation results

The electro-optic properties of the single-rubbing VA-FIS are calculated by a commercial LCD simulator DIMOS.2D and the extended Jones matrix [56]. The cell parameters are: electrode width w = 2 µm, electrode gap g = 5 µm, and cell gap d = 4 µm. A 100-nm-thick Si_3N_4 (dielectric constant ε =6.5) is employed as the passivation layer. The LC material used here is a positive $\Delta\varepsilon$ LC material, which has following physical properties: K_{11} = 12.7 pN, K_{22}=6.4 pN, K_{33}= 14.0 pN, Δn = 0.125, $\Delta\varepsilon$ = 6.7, and γ_1 = 53 mPas. Also, as discussed above, a biased voltage (V_{bias} = 4 V) is applied to the top electrode to generate vertical electric field.

(a) Voltage-transmittance (VT) and time-transmittance (VT) curves

Firstly, conventional VA-FIS with double rubbing is investigated and its voltage-dependent (VT) and time-dependent (TT) curves are plotted in Figure 2.6 (black lines). The response time is pretty fast [rise time: 1.07 ms, decay time: 0.61 ms], but from Figure 2.6(a), the on-state voltage is higher than 20 V, and transmittance at 15 V is only 58.0%, which is too low for practical applications.

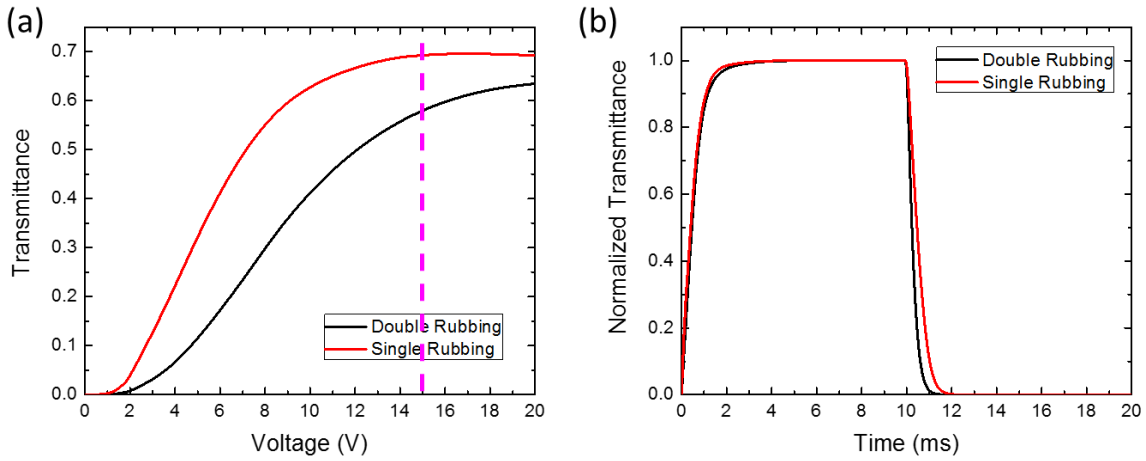

Figure 2.6. Simulated (a) VT and (b) TT curves for VA-FIS with and without bottom alignment layer. (λ=550 nm. Here, polyimide alignment layer is used with 70 nm thick)

Table 2.5. Simulated VA-FIS device performance with different rubbing conditions.

	V	T @ 15 V	Rise time	Decay time
Double rubbing	> 20 V	58.0%	1.07 ms	0.61 ms
Top rubbing	15 V	69.3%	0.91 ms	0.93 ms
Bottom rubbing	> 20 V	58.7%	1.14 ms	0.62 ms
No rubbing	15.4 V	66.5%	1.05 ms	0.95 ms

On the other hand, the newly proposed single-rubbing VA-FIS shows significant improvement. For example, its VT curve increases much earlier and faster. The corresponding on-state voltage is only 17 V, and transmittance at 15 V is as high as 69.3%. As listed in Table 2.5, the rise time of top-rubbing VA-FIS cell is τ_{on} = 0.91 ms and decay time τ_{off} = 0.93 ms.

To better understand the underlying physical mechanism, the LC director distributions for both cases are plotted in Figure 2.7. Clearly, for conventional case [Figure 2.7(a)], the LC directors near bottom substrate stay still due to the strong anchoring energy. But for the single-rubbing case [Figure 2.7(b)], these LC directors reorient freely and easily along the electric field. As a result, the phase retardation is larger and the required voltage is lower.

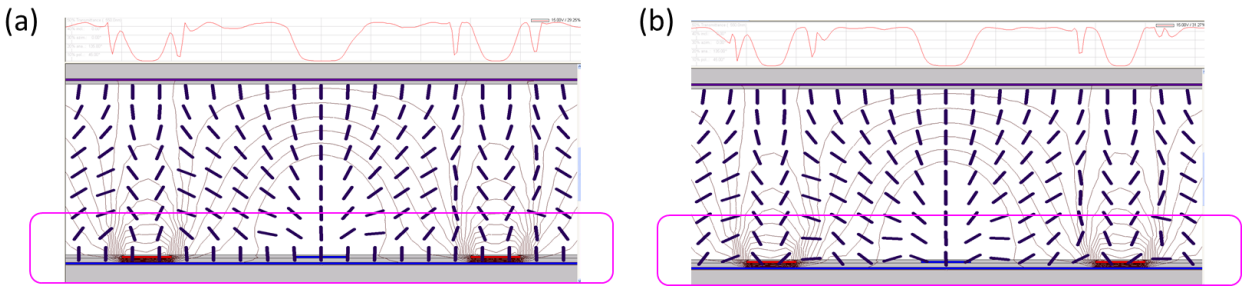

Figure 2.7. Simulated LC director distribution for (a) VA-FIS with double-side rubbing, and (b) VA-FIS with single-side rubbing.

(b) Rubbing condition

Next, we investigate two more rubbing conditions, i.e. single alignment layer on bottom substrate and no alignment layer on both substrates. Results are shown in Figure 2.8, and data are summarized in Table 2.5. Interestingly, the bottom-rubbing case shows almost the same performance as that of double-rubbing, although the top alignment layer is removed. This is because the LC molecular reorientations mainly happen near the bottom substrate (i.e. lower side of LC region), which are governed by the bottom alignment layer. Then as expected, once we

remove this bottom alignment layer, the device performance would be improved noticeably, as the top-rubbing case (red line) and no-rubbing case (pink line) shown in Figure 2.8.

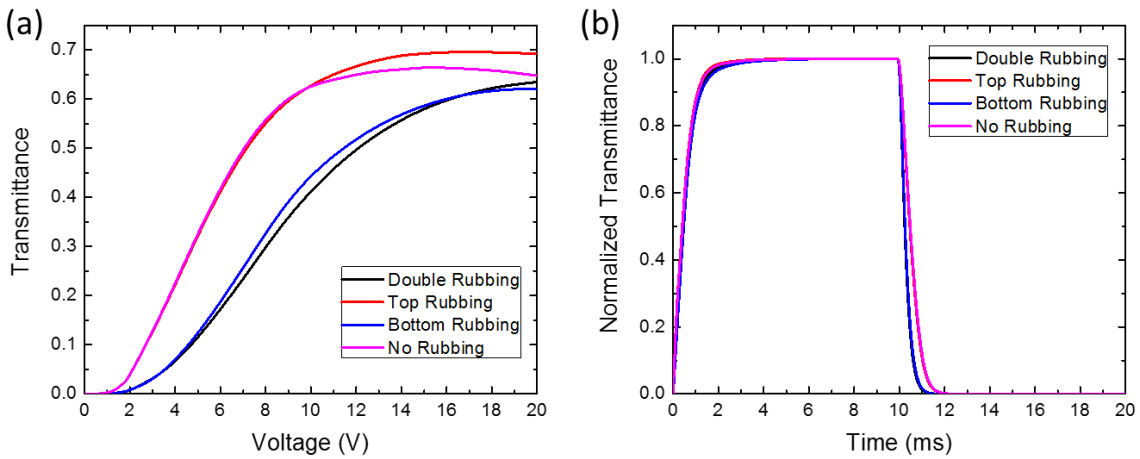

Figure 2.8. Simulated (a) VT and (b) TT curves for different rubbing conditions. (Double rubbing: two alignment layers; top rubbing: one alignment layer on top substrate; bottom rubbing: one alignment layer on bottom substrate; no rubbing: no alignment layers)

(c) Biased voltage effect

So far, the biased voltage applied to the top electrode is kept at 4 V. Here, we tune this voltage to investigate how it affects the E-O properties. Results are shown in Figure 2.9. When the biased voltage increases from 3 V to 5 V, the response time becomes much faster as the vertical electric field gets stronger. But the trade-offs are increased on-state voltage (from 14 V to 20 V) and slightly decreased transmittance (from 70.4% to 65.8% at 15 V). To balance all the desired properties, V_{bias} = 4 V would be a good choice, depending on the $\Delta\varepsilon$ of the LC employed.

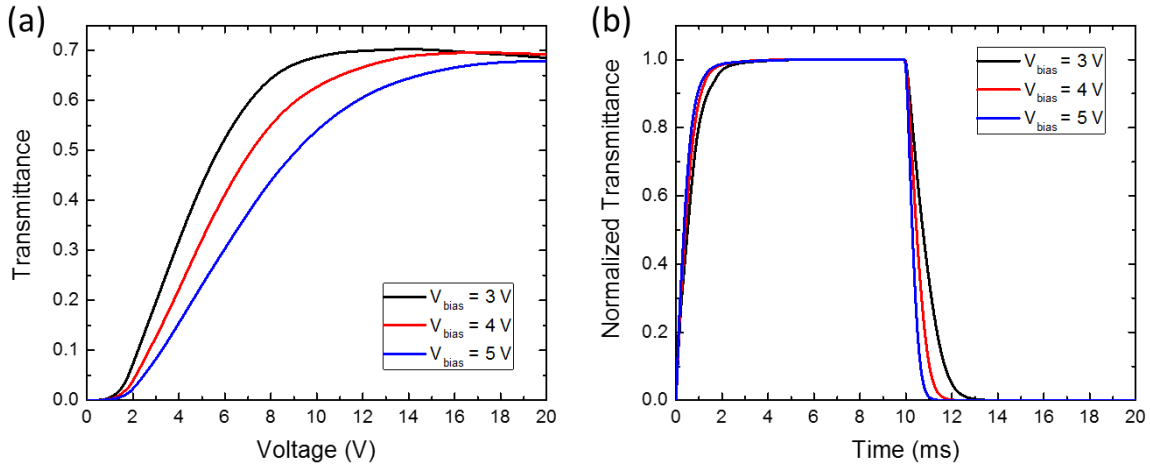

Figure 2.9. Simulated (a) VT and (b) TT curves for different biased voltages.

(d) Cell gap effect

Figure 2.10 shows the cell gap effect of single-rubbing VA-FIS mode. As usual, thin cell gap is more favorable for fast response time, as $\tau \sim d^2$ [4]. But voltage and transmittance would be sacrificed simultaneously. From Figure 2.10, cell gap d = 4.5 μm shows the lowest operation voltage (V_{on} = 11.7 V), but its response time is also the slowest [rise time: 1.27 ms, decay time: 0.99 ms]. For practical applications, we have to choose the cell gap carefully. Here, we keep d = 4 μm for further optimizations.

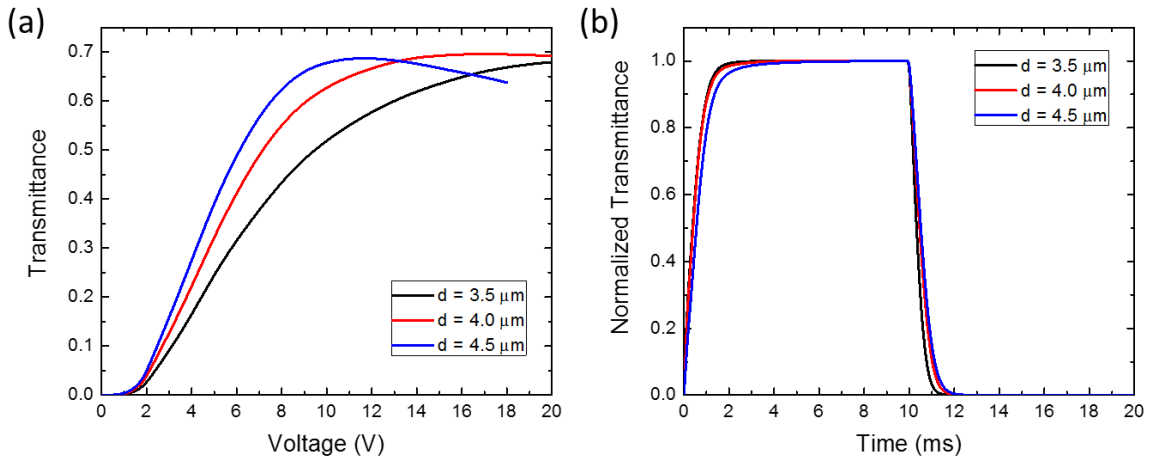

Figure 2.10. Simulated (a) VT and (b) TT curves for different cell gaps.

(e) Electrode gap effect

Larger electrode gap leads to a higher peak transmittance, but also higher on-state voltage. As shown in Figure 2.11, when we increase the electrode gap from 4 μm to 6 μm, peak transmittance is increased from 64.2% to over 70%, but the on-state voltage is also increased from 12.8 V to over 20 V. Here, we set 15 V as the maximum driving voltage and found that electrode gap g = 5 μm is the optimum.

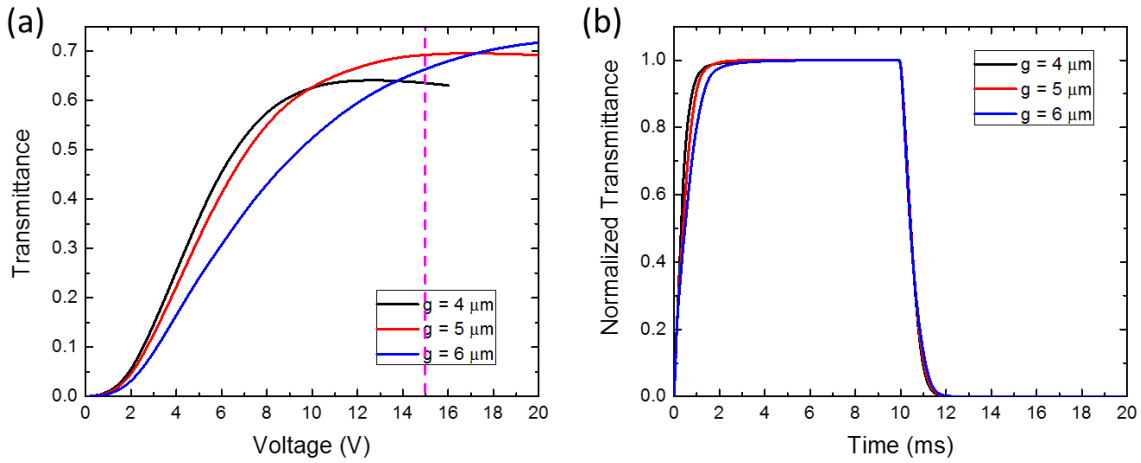

Figure 2.11. Simulated (a) VT and (b) TT curves for different electrode gaps.

(f) Passivation layer effect

For conventional fringe field switching (FFS) mode, passivation layer should be as thin as possible to mitigate the voltage shielding effect, so that operation voltage could be reduced. But in VA-FIS, it is totally different. As depicted in Figure 2.12, when the passivation layer gets thicker, the operation voltage becomes lower, e.g. V_{on} = 9.6 V for t_{pass} = 0.5 μm. This is because of the unique VA-FIS structure, where two forces (vertical and horizontal electric fields) are competing each other. For a thick passivation layer, the corresponding vertical electric field becomes weaker.

As a result, horizontal electric field would dominate and the LC directors would be reoriented more easily, leading to a much lower operation voltage.

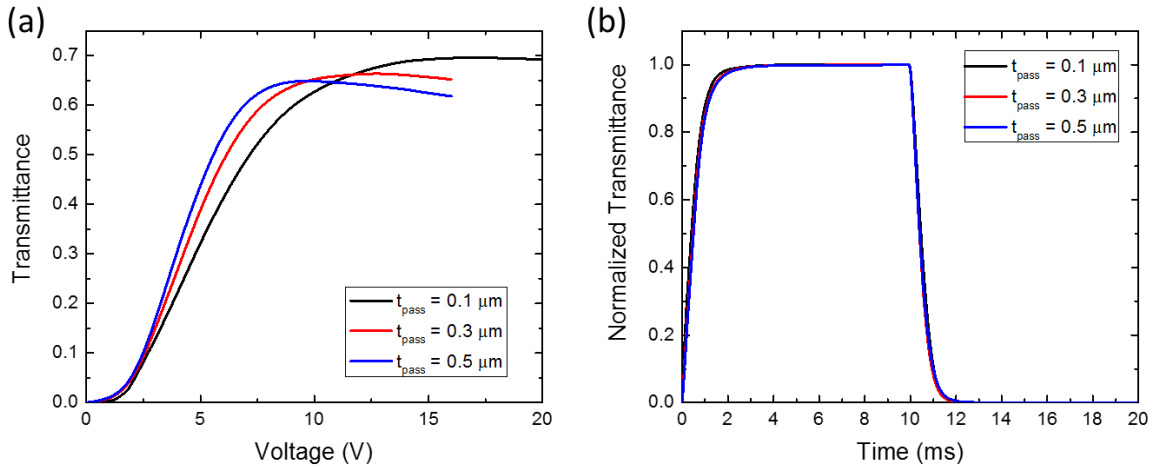

Figure 2.12. Simulated (a) VT and (b) TT curves for different passivation layer thicknesses.

As discussed above, increasing the passivation layer thickness seems to be a good approach to reduce the operation voltage. But unexpectedly, the dark state and threshold voltage are sacrificed, as shown in Figure 2.13. In conventional VA-FIS with double-rubbing, no biased voltage is applied (black line), it shows the best dark state and the highest threshold voltage. This is more favorable after taking TFT fluctuations into consideration. But when a biased voltage is applied (red line), threshold voltage is greatly reduced. This is because the threshold state of LC directors is already broken by the vertical electric field. Then a very small horizontal electric field would cause these molecules to reorient. Similarly, for the single-rubbing case, threshold voltage is further reduced.

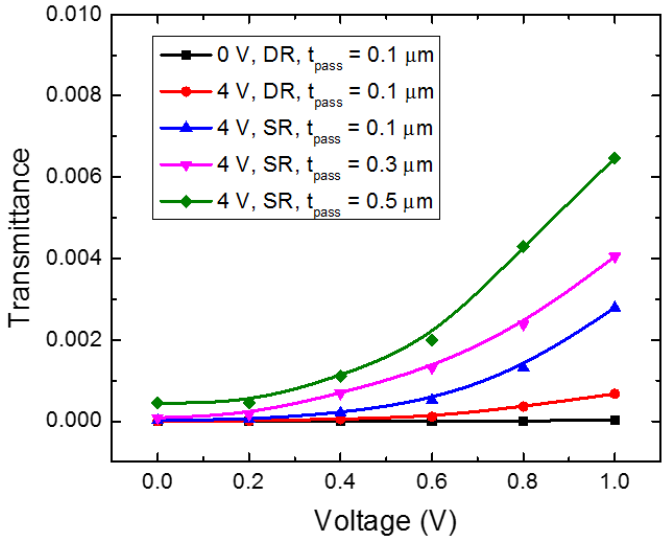

Figure 2.13. Simulated dark state and threshold voltage for different thicknesses of passivation layer. (DR: double rubbing; SR: single rubbing)

This effect could be visualized more clearly in Figure 2.14. For double-rubbing case without biased voltage [Figure 2.14(a)], no electric field exists and LCs are vertically aligned, showing the best dark state. When a biased voltage is applied [Figure 2.14(b)], in theory, there should be vertical electric field. Nevertheless, this field is not perfectly vertical due to the shielding effect of passivation layer. As shown in Figure 2.14(b), the electric field is slightly slanted. In this case, some LC molecules have already been reoriented, meaning threshold state is broken. If we further remove the bottom alignment and increase the thickness of passivation layer [Figures 2.14(c) – 2.14(d)], this effect is magnified. The non-uniformity of vertical electric field would induce more LC molecules to reorient, and finally, dark state and threshold voltage would be compromised.

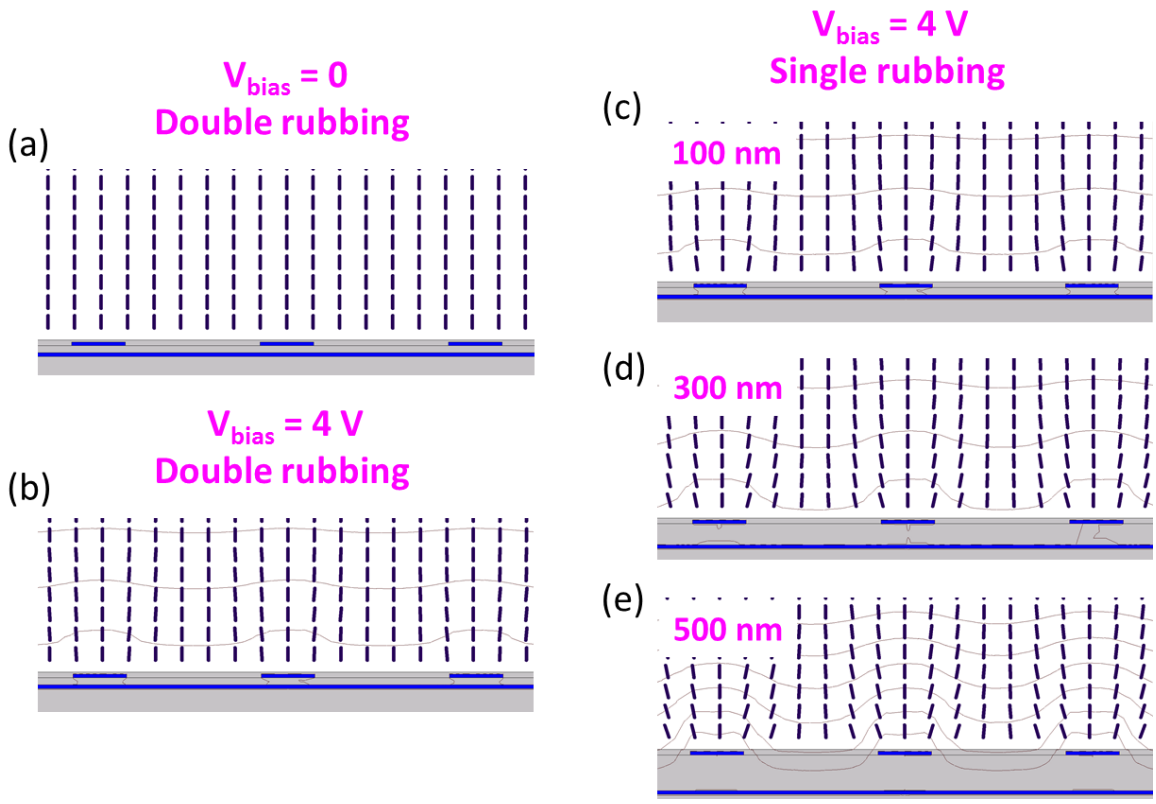

Figure 2.14. Simulated LC director and equipotential line distribution for (a) double rubbing without biased voltage; (b) double rubbing with biased voltage; (c) single rubbing with 100 nm thick passivation layer; (d) single rubbing with 300 nm thick passivation layer; and (e) single rubbing with 500 nm thick passivation layer. (All single rubbing cases have a biased voltage)

To overcome this light leakage issue, we propose to apply a small biased voltage to the bottom common electrode to compensate the voltage shielding effect of passivation layer. For example, the common electrode has a small biased voltage, e.g. V_{com} = -0.8 V, then at voltage-off state, the resultant electric field is quite uniform, as plotted in Figure 2.15(b). Therefore, both dark state and threshold voltage are improved significantly, as shown in Figure 2.15(c). Here, it is illustrated using the worst case: single rubbing with thick passivation layer (t_{pass} = 0.5 μm). Undoubtedly, this approach works as well for other conditions, like thin passivation layer and

double-rubbing case. A side effect of this approach is increased operation voltage, as the threshold voltage increases slightly.

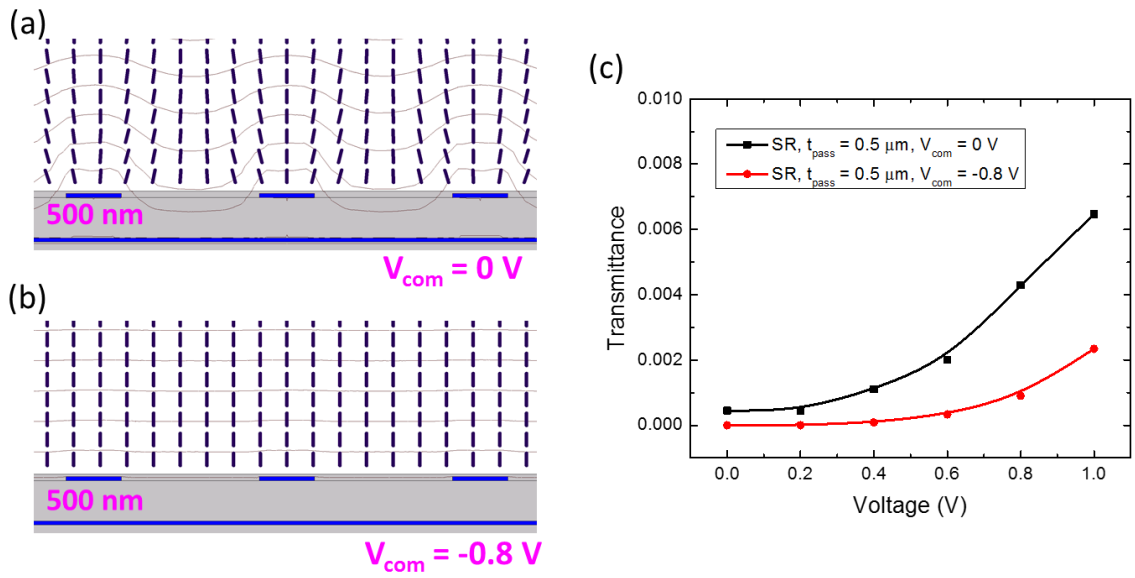

Figure 2.15. Simulated LC director and equipotential line distribution for (a) single rubbing with V_{com} = 0 V; (b) single rubbing with V_{com} = -0.8 V; and (c) Simulated dark state and threshold voltage for these two conditions. (SR: single rubbing; V_{bias} = 4 V)

(g) Anchoring energy effect

For the above discussions, we focus on the single-rubbing condition, where bottom alignment layer is totally removed, i.e. the bottom anchoring energy is zero. But for some cases, bottom alignment layer is still preferred to get better vertical alignment and then higher contrast ratio. With that, we carry out more investigations on the anchoring energy effect. Results are summarized in Figure 2.16. It is seen that with weak anchoring energy (W = 10^{-6} ~ 10^{-5} N/m), it performs almost the same as that of zero anchoring energy, which means we can still keep the bottom alignment layer, as long as its anchoring energy is weak. Also, as expected, high voltage and low transmittance is obtained with strong anchoring energy (W = 10^{-3} ~ 10^{-2} N/m).

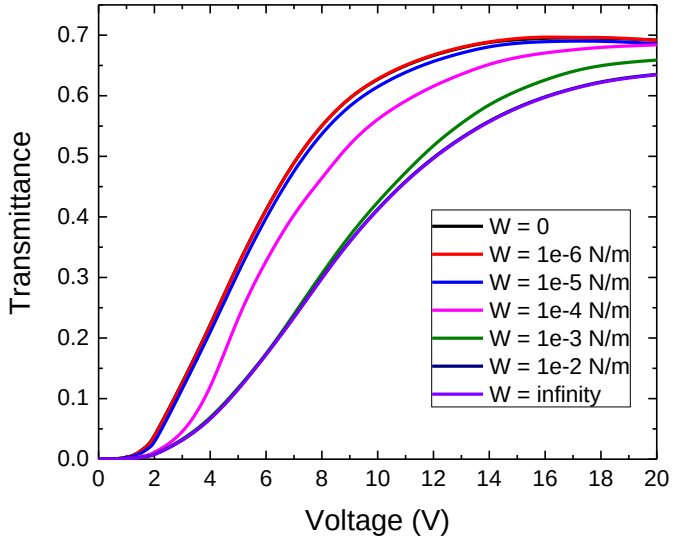

Figure 2.16. Simulated VT curves for different anchoring energies of bottom substrate. (Top substrate is fixed with strong anchoring energy)

2.3.3 Discussion

In general, single-rubbing VA-FIS mode exhibits several advantages: high transmittance (~70%), low operation voltage (15 V), and fast response time (< 1 ms). This is much faster than the required 2 ms. In fact, if overdrive and undershoot driving method is adopted [48, 57, 58], the average GTG response time of VA-FIS is only ~0.4 ms. Moreover, all gray scale transitions are below 1 ms, which is highly desirable for suppressing motion blurs.

Another thing worth mentioning here is VA-FIS is also a perfect candidate for field sequential color (FSC) LCDs. It is known that FSC LCD exhibits two major advantages: 3x higher resolution density and 3x higher optical efficiency, as the absorptive spatial color filters are removed [59]. However, to suppress the color breakup of FSC LCD, the required response time is quite challenging [60]; typically it should be less than 1 ms. Hopefully, VA-FIS has sub-millisecond response time, and is a strong contender for next-generation FSC LCDs.

However, before practical applications, several hurdles of VA-FIS should be addressed satisfactorily. For example, gamma shift at large oblique angles should be well compensated by multi-domain electrode configurations [61]. Also, its contrast ratio and threshold voltage should be treated carefully. The requirements of 15 V and 2-TFT driving are still manageable, but if the on-state voltage could be further reduced to 7.5 V with single TFT, then such a single-rubbing VA-FIS would be more competitive and has widespread applications in the near future.

2.4 Fast-response polymer-stabilized blue phase liquid crystal

Blue phase liquid crystal (BPLC) was first discovered in 1888, but it didn't gain many popularities until early 2000s, when polymer-stabilized BPLC was proposed [62]. Briefly speaking, PS-BPLC exhibits several outstanding features, such as sub-millisecond response time, no need for surface alignment, optically isotropic dark state, and cell gap insensitivity [63]. Fast response time enables FSC displays with negligible color breakup, just like aforementioned VA-FIS. In fact, after about 15 years of extensive efforts, most of the problems impeding the commercialization of BPLC have been gradually overcome, such as long term stability, protrusion fabrication, slow TFT charging time, etc. [64, 65] However, the on-state voltage (V_{on}) is still too high to be addressed by a single TFT per pixel.

To lower operation voltage, enlarging the Kerr constant (K) of BPLC mixture seems to be a straightforward approach because $V_{on} \sim 1/\sqrt{K}$ [66]. Indeed, this is where material efforts have been devoted in the past few years [67, 68]. Some high birefringence BPLC hosts with dielectric anisotropy $\Delta\varepsilon$ >100 have been developed [66-69]. However, the major trade-offs for such a huge-$\Delta\varepsilon$ BPLC material are: 1) increased response time (>1 ms) due to its high viscosity, 2) prolonged TFT charging time due to its large capacitance, and 3) compromised long term stability and voltage

holding ratio (VHR). For a high resolution and high frame rate (≥120 Hz) display, the maximum $\Delta\varepsilon$ of the BPLC should not exceed 100. With that, slow charging issue can still be managed by the bootstrapping driving scheme [64, 65], while its VHR could reach as high as 99%, depending on the charging time (governed by the frame rate and resolution density) and working temperature [68]. Moreover, its long-term stability has been verified experimentally, as reported in Ref. [67]. Actually, such a BPLC mixture ($\Delta\varepsilon$ < 100) has already been experimentally proven by AUO in a 10" prototype [70]. Indeed, its overall performance is quite impressive except that V_{on} is still as high as 32 V_{rms}. As a result, two TFTs per pixel is required. The power consumption of a display driver IC (excluding backlight) is proportional to $(V_{on})^2$. Therefore, it is essential to lower the V_{on} to ≤ 15 V to enable single TFT driving with this practical BPLC material ($\Delta\varepsilon \leq 100$). Such a burden falls on the new device structure.

In this part, we propose a new protruded diamond-shape in-plane-switching (DIPS) electrode configuration to lower the operation voltage. By optimizing the device parameters, we can boost the peak transmittance to over 75% at 15 V. It enables single-TFT driving and lower the power consumption, and more importantly, this is achieved using a practical BPLC material with mild $\Delta\varepsilon$.

2.4.1 Structure design

The induced birefringence Δn_i of an optically isotropic BPLC can be described by the extended Kerr model [71]:

$$\Delta n_i(E) = \Delta n_s \left\{1 - \exp\left[-(E/E_s)^2\right]\right\}, \tag{2.5}$$

where Δn_s stands for the saturated induced birefringence, E is the applied electric field, and E_S represents the saturation field. However, above the electrode the generated electric field is along

vertical direction so that little phase retardation is produced, leading to low transmittance (known as dead zones). In order to boost transmittance, a large electrode gap is often employed, which in turn increases the operation voltage.

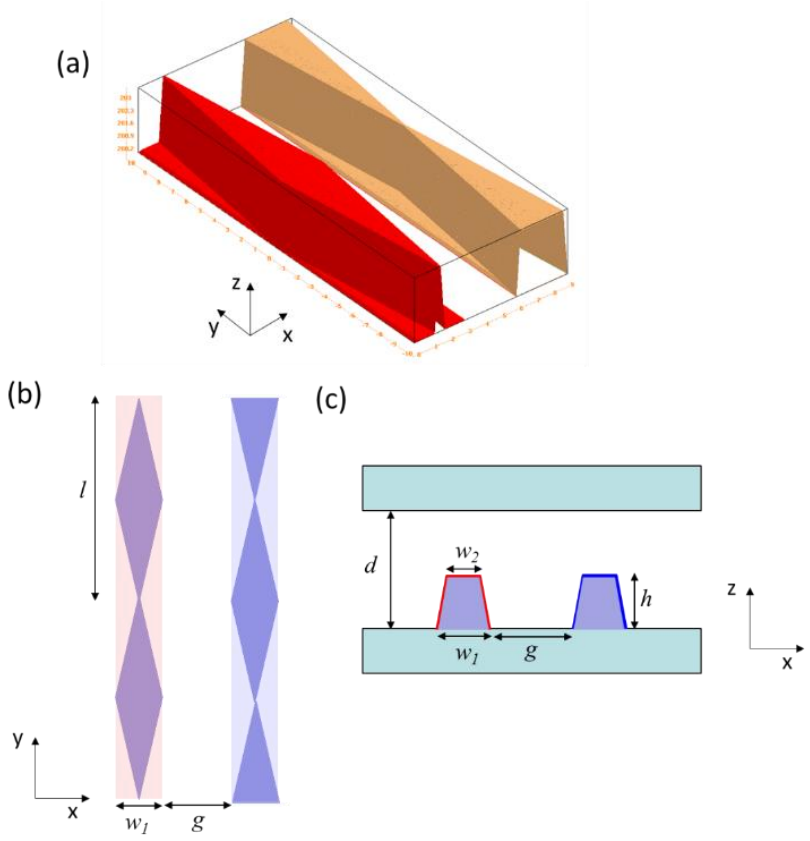

Figure 2.17. (a) Schematic 3D diagram of the proposed DIPS structure; (b) top view and (c) cross-section view.

Figure 2.17(a) depicts the DIPS electrode structure. The conventional strip protrusion is modified to diamond shape [Figure 2.17(b)], so that the effective dead zone area can be greatly reduced. From the cross-section view [Figure 2.17(c)], it is almost the same as traditional protruded IPS [70, 72]. Here, the electrode width and protrusion height is fixed as w_1 = 3 μm and h = 3.5 μm, respectively, to be compatible with current fabrication technology [70]. As Figure 2.17 shows,

there is a spatial shift between adjacent pixel and common electrodes. This helps boost the total transmittance, as will be discussed later.

From fabrication viewpoint, our DIPS structure shares the same procedures as conventional protruded IPS, as reported in Ref. [70]. Although we have not actually fabricated the DIPS device, its procedures are outlined as follows: The first step is to form diamond-shape protrusions (e.g. SiO_2, Si_4N_3, organic materials, etc.) on the bottom substrate by photolithography. The width of top side (Figure 2.17) is controlled to be w_2 = 2.5 μm and the protrusion height is h = 3.5 μm. The second step is to over-coat the protrusion surface with a thin indium tin oxide (ITO) layer. A strong and deep penetrating horizontal electric field between the neighboring electrodes is thus generated. No surface alignment layer is needed.

2.4.2 Simulation results

Next, we investigate the electro-optic performance of the proposed DIPS structure using a commercial software TechWiz LCD 3D (Sanayi, Korea). As discussed above, the protruded electrodes are designed with w_1 = 3 μm, w_2 = 2.5 μm, and h = 3.5 μm, which is compatible with current fabrication facility [70]. The electrode gap is set as g = 3 μm, and the cell gap is d = 9 μm. Another important factor is diamond length (l), which is assumed to be 20 μm.

To obtain the BPLC parameters, we first fit the voltage-dependent transmittance (VT) curve reported by AUO, as Figure 2.18 shows, using Eq. (2.5). Good agreement between experiment and simulation is obtained. The small difference is attributed to different light sources employed: for experiment it is white light, while in our fitting we use λ = 550 nm. Through fitting, we obtained Δn_s = 0.16 and E_s = 5.7 V/μm, which corresponds to K = 9.28 nm/V^2 at λ = 550 nm. From here on, we will use these BPLC material parameters in our device optimization.

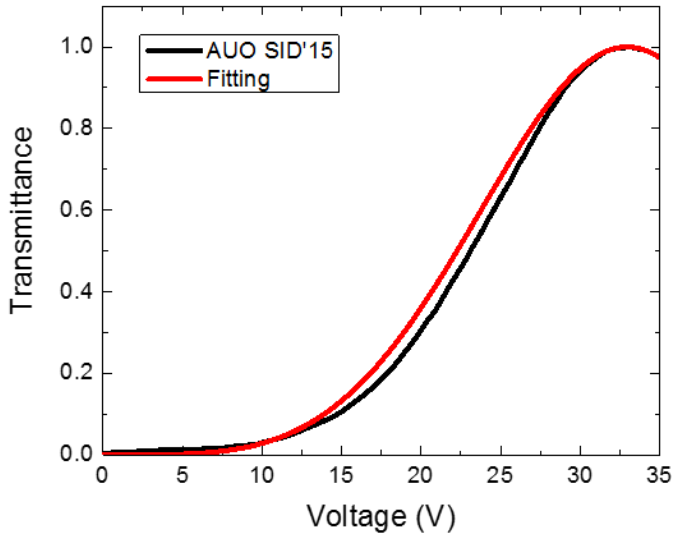

Figure 2.18. Numerical fitting for the VT curve reported in Ref. [70] using extended Kerr model. (λ = 550 nm)

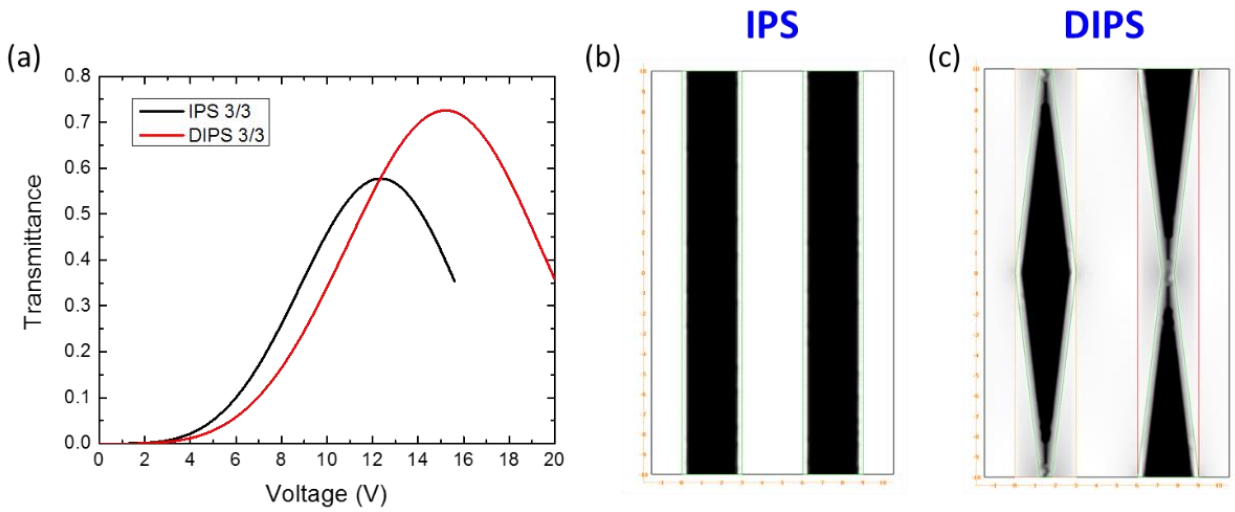

Figure 2.19. (a) Simulated VT curves for conventional protruded IPS and DIPS; Brightness profile at on-state voltage for (b) conventional IPS and (c) DIPS. (w_1 = 3 μm, w_2 = 2.5 μm, g = 3 μm, h = 3.5 μm, and d = 9 μm for both IPS and DIPS. l = 20 μm for DIPS only)

Figure 2.19(a) shows the simulated VT curves for conventional IPS and newly proposed DIPS. As expected, the peak transmittance of DIPS is much higher than that of IPS (72.6% vs. 57.8%), due to the reduced dead zone area. This effect could be virtualized more clearly from

Figures 2.19(b) and 2.19(c). For conventional IPS, a large strip dead zone exists above the electrode, while for DIPS, the protrusion size is reduced, along with the reduced dark region. As a result, the transmittance is improved significantly. But the trade-off is slightly increased voltage (15.2 V vs. 12.4 V), since the effective electrode gap is larger.

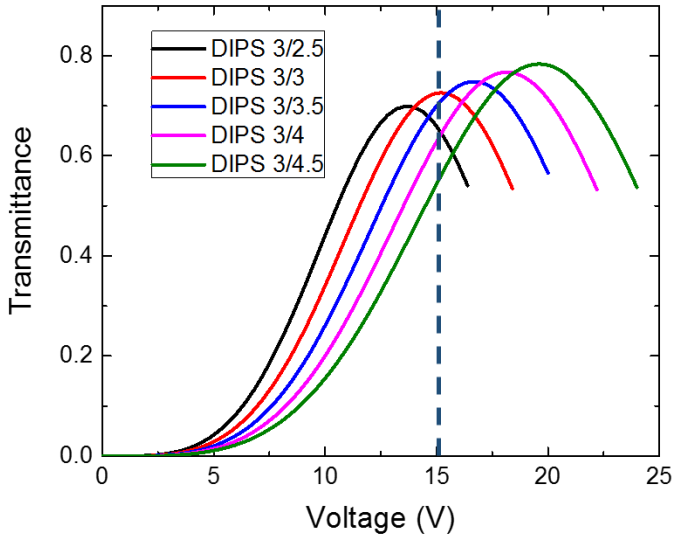

Figure 2.20. Simulated VT curves for different electrode gaps. (w_1 = 3 μm, w_2 = 2.5 μm, h = 3.5 μm, d = 9 μm, and l = 20 μm)

Next, we tune the electrode gap from 2.5 μm to 5 μm, and their corresponding VT curves are depicted in Figure 2.20. Both operation voltage and peak transmittance keep increasing as the electrode gap gets larger. If we set V_{on} =15 V, the highest transmittance (72.5%) is obtained when the electrode gap g = 3 μm. For further optimizations, we will keep g = 3 μm.

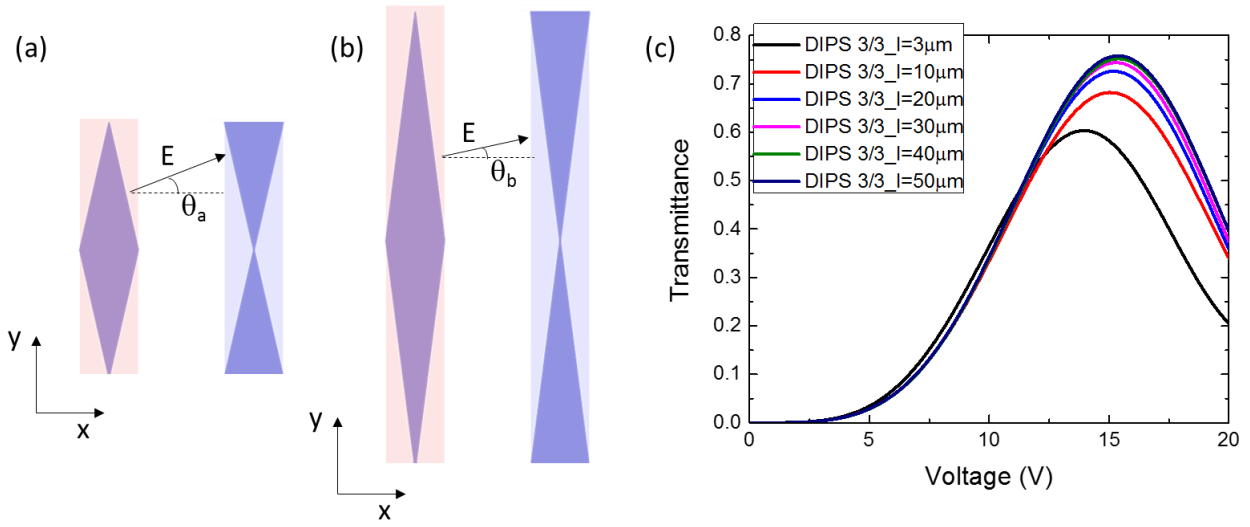

Figure 2.21. Schematic diagram for (a) short diamond electrode and (b) long diamond electrode; (c) simulated VT curves for different diamond lengths. (w_1 = 3 μm, w_2 = 2.5 μm, g = 3 μm, h = 3.5 μm, and d = 9 μm)

Due to the specially designed diamond shape, the generated electric field is not parallel to the x-axis, instead, there is a small slanted angle (θ), as Figure 2.21(a) shows. Therefore, the phase retardation is not fully utilized if the linear polarizer is oriented at 45° with respect to x-axis. To reduce this slant angle, an efficient approach is to increase the diamond length (l). As it gets longer [Figure 2.21(b)], this angle gets smaller (i.e. $\theta_a > \theta_b$), leading to larger phase retardation. Figure 2.21(c) depicts the simulated VT curves as a function of diamond length. As expected, peak transmittance increases with l, but gradually saturates when $l \geq 40$ μm. A similar trend is found for operation voltage: it increases first and then gradually saturates. Please note that when l = 50 μm, the transmittance at 15 V is as high as 75.5%, which is good enough for practical applications.

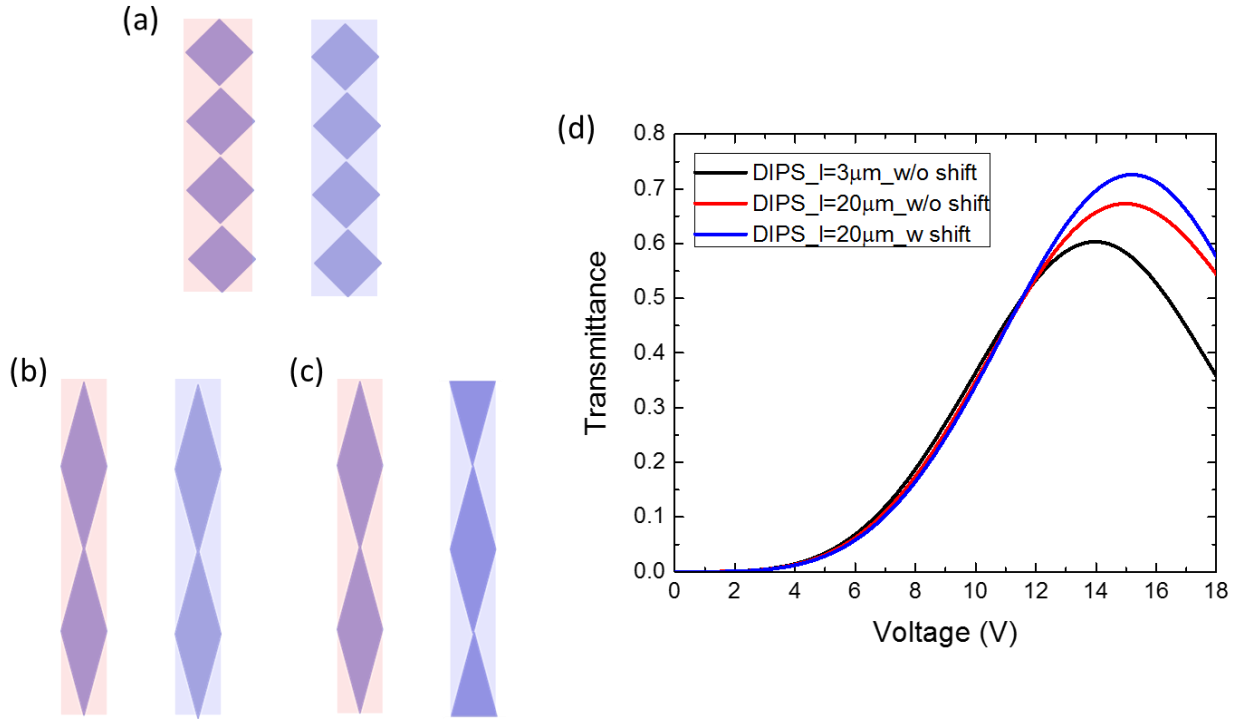

Figure 2.22. Schematic diagram for (a) unshifted electrode with short diamond, (b) unshifted electrode with long diamond and (c) shifted electrode with long diamond; (d) Simulated VT curves for the structures in (a) to (c). (w_1 = 3 μm, w_2 = 2.5 μm, g = 3 μm, h = 3.5 μm, and d = 9 μm)

As Figure 2.22(c) shows, there is a spatial shift between adjacent pixel and common electrodes. In this case, the electric field is uniformly distributed. While for the unshifted structures [Figures 2.22(a) and 2.22(b)], the generated electric filed is distorted: stronger in the bulging region but weaker in the hollow region, resulting in a decreased transmittance. Figure 2.22(d) plots the simulated VT curves for these three cases, where the shifted configuration [Figure 2.22(c)] shows the highest transmittance. Its transmittance is 14.2% higher than that of unshifted one with smaller diamond length, i.e. square shape in Figure 2.22(a) [73].

2.4.3 Discussion

We investigate the electro-optic performance of DIPS structure and the influencing factors. With some optimizations, we have achieved 75.5% transmittance at 15 V. For conventional protruded IPS, it exhibits much larger dead zone [Figure 2.19(b)]. As a result, to improve transmittance a wider electrode gap (g = 7.5 μm) is needed, which in turn increases the operation voltage [Figure 2.23]. Compared to conventional protruded IPS, the on-state voltage of our DIPS is lowered by 41.4% (15.3 V vs. 26.1 V) while keeping the same transmittance. Our design enables BPLCDs to be driven by a single TFT.

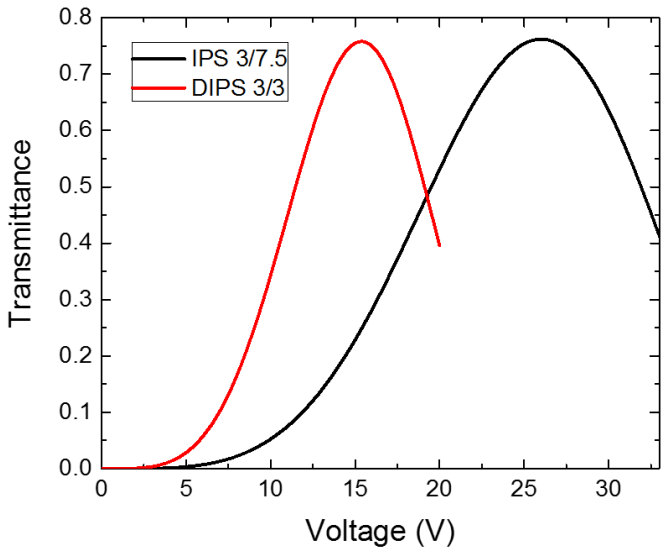

Figure 2.23. Simulated VT curves for conventional IPS and DIPS. (w_1 = 3 μm, w_2 = 2.5 μm, g = 7.5 μm, h = 3.5 μm, and d = 9 μm for IPS; w_1 = 3 μm, w_2 = 2.5 μm, g = 3 μm, h = 3.5 μm, d = 9 μm, and l = 20 μm for DIPS)

To obtain wide view and suppress gamma shifts, two-domain configuration is commonly employed [74]. Here, we simulate the performance of zigzag DIPS structure. Results are plotted in Figure 2.24. From Figure 2.24(a), the isocontrast ratio remains over 100:1 in the entire viewing zone. Also, the calculated gamma shift (D) is only 0.1634, which is smaller than 0.2, i.e. it is

unnoticeable to the human eye [61]. Moreover, since we are using IPS structure, the electro-optic properties are insensitive to the cell gap. Thus, BPLCD should work well for touch panels.

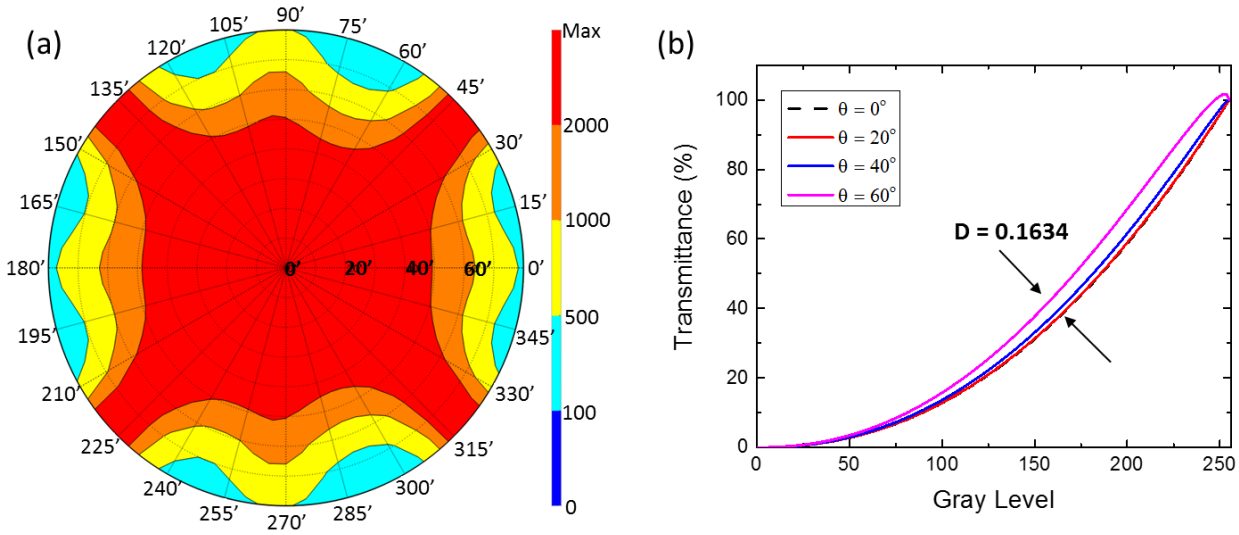

Figure 2.24. (a) Simulated isocontrast contour and (b) viewing angle dependence of gamma curves for biaxial film-compensated 2-domian DIPS.

2.5 Summary

In this chapter, we firstly introduce an important concept called motion picture response time to quantify the image motion blur. According to the analysis, we found that if LC response time is less than 2 ms, its MPRT is comparable to that of OLED, although OLED's response is 100x faster. Then we developed an ultra-low viscosity LC mixture with negative dielectric anisotropy, and demonstrated a fast-response VA LCD with average GTG response time less than 2 ms. The corresponding MPRT is indeed comparable to OLED at the same frame rate. The validity of this 2-ms rule is confirmed.

Also, we propose a novel single-rubbing VA-FIS mode to achieve sub-millisecond response time while keeping high transmittance and low operation voltage. A potential concern is

the degraded dark state and much reduced threshold voltage due to non-uniform vertical electric field. To improve that, we propose to add a small biased voltage to the bottom common electrode, to compensate the voltage shielding effect of passivation layer. Good performance is obtained.

Finally, in the last part, we investigate fast response PS-BPLC. Our new diamond-shape protruded IPS structure helps to lower the operation voltage of a BPLCD to 15V by using an industrially proven blue phase material, while keeping a relatively high transmittance (75.5%). This is an important step toward enabling single-TFT driving using a practical BPLC material with a mild $\Delta\varepsilon$ without compromising other desirable features, including sub-millisecond response time, long-term stability, no TFT charging issue, high voltage holding ratio, etc. As for the fabrications, DIPS shares the same fabrication process as conventional protruded IPS. Our DIPS structure would help to accelerate the emergence of the long-awaited blue phase LCDs for widespread applications.

CHAPTER THREE: WIDE COLOR GAMUT

Vivid color is a critical requirement of all display devices. In the past two decades, LCD backlight technology has evolved from cold cathode fluorescence lamp (CCFL) to phosphor-converted white light emitting diode (WLED) [31, 32]. The latter employs a blue LED to pump YAG:Ce^{3+} yellow phosphor to generate white color. The major advantages of WLED are high efficiency, long lifetime, low cost and simple optical configuration. However, its broad yellow spectrum leads to a relatively narrow color gamut (~70% NTSC or ~ 50% Rec. 2020).

To widen color gamut, quantum dot (QD)-enhanced backlight and two phosphor-converted WLED (2pc-WLED) have been developed [33-35]. Each technology has its pros and cons. For examples, the cadmium-based QDs offer a narrow emission bandwidth (full width at half maximum FWHM ~20-30 nm) and large freedom for selecting peak wavelengths to match the transmittance of color filters [75-78]. The resultant color gamut can reach 108% NTSC in CIE 1931 color space, or ~90% Rec. 2020 color standard. However, cadmium is a toxic heavy metal and its maximum allowable level is limited to 100 ppm according to the European Union's Restriction of Hazardous Substances (RoHS). Some heavy-metal-free QDs have been developed, such as InP/ZnS, but their efficiency and bandwidth are compromised [79, 80]. Moreover, these QDs are often present as a film, known as quantum dot enhancement film (QDEF) [81]. For a large screen LCD TV, the QDEF should match the TV size, thus the cost issue needs to be taken into consideration as well.

On the other hand, 2pc-WLED can be easily integrated into on-chip configuration and it offers advantages in low cost, high brightness, excellent stability, and long lifetime. But the bottleneck is its relatively wide emission bandwidth, e.g. the state-of-the-art green phosphor (β-

sialon:Eu^{2+}) still exhibits FWHM ~55 nm [35, 82, 83]. While for red phosphor ($K_2SiF_6:Mn^{4+}$) with five emission peaks, its individual FWHM is quite narrow but the effective peak wavelength centers at 625 nm [35, 84-86], which is slightly short from an ideal red color of 638 nm [77]. Therefore, red (R), green (G) and blue (B) lights still show a large crosstalk after passing through the color filters, which in turn degrades the color purity.

3.1 Enlarging an LCD's color gamut with a functional reflective polarizer

To enlarge color gamut, here we propose to add a functional reflective polarizer (FRP) in the backlight unit to suppress the color crosstalk [87]. Such a FRP works as a notch filter to reflect the unwanted spectrum, while transmitting the remaining wavelengths with high efficiency. By optimizing the FRP bandwidth, we can boost the color gamut from 96.7% to 108.6% NTSC in CIE 1931, or from 112.9% to 133.9% NTSC in CIE 1976, which is comparable to the Cd-based QDs. The incurred 16% optical loss results from the blocking of unwanted colors. Our design is completely compatible to the current backlight configuration; it simply replaces the conventional reflective polarizer with our new FRP. No extra modification or cost is required.

3.1.1 Structure design

Figure 3.1(a) shows the transmission spectrum of commonly employed color filters (dashed lines) and the emission spectrum of a 2pc-WLED (solid line). The RGB color filters exhibit severe crosstalks in the blue-green and yellow spectral regions. Figures 3.1(b) to 3.1(d) show the transmitted spectra after RGB color filters. Here, the fringe field switching (FFS) LCD with a negative dielectric anisotropy ($\Delta\varepsilon < 0$) LC mixture is employed in our simulation and the wavelength dependent refractive indices are considered. Clearly, there is some light leakage for

each channel, especially for blue, where a fairly large bump leaks through the green color filters, deteriorating the final color purity.

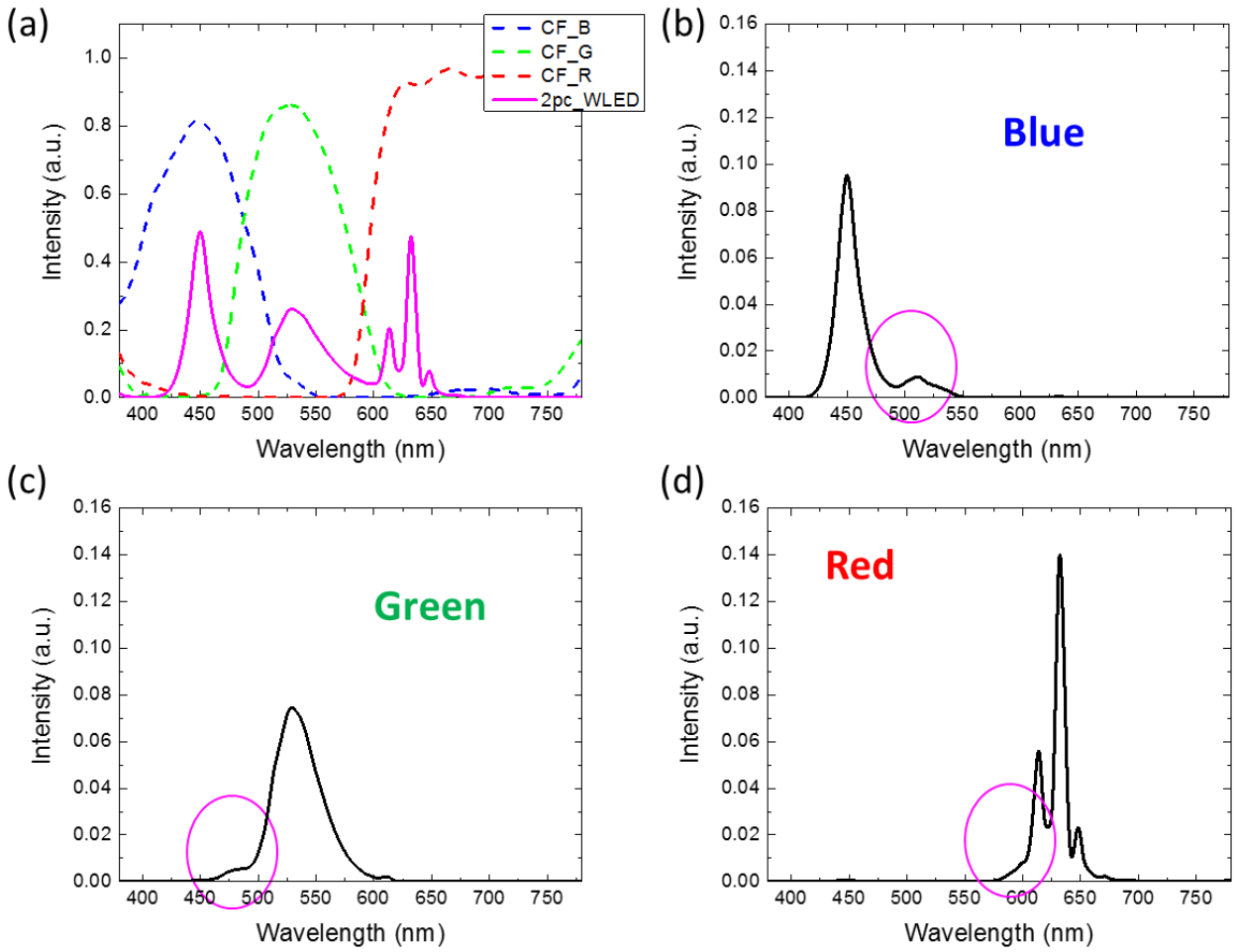

Figure 3.1. (a) Transmission spectrum for commercial color filters and 2pc-WLED with green (β-sialon:Eu^{2+}) and red (K_2SiF_6:Mn^{4+}) phosphors; (b)-(d) Output spectrum for the blue, green and red sub-pixels, respectively.

To suppress the color crosstalk, we propose to replace the conventional reflective polarizer [88, 89] with a functional reflective polarizer [90] in the backlight unit. Figure 3.2 shows the panel configuration with an edge-lit 2pc-WLED as an example. Different from QDEF or QD rail-based backlight, the 2pc-WLED can be packed into a chip without thermal stability issue. Therefore, the

whole system is compact. The light guide plate (LGP) together with an inverted prism film forms a directional backlight [91], and a front diffuser spreads the incident light to achieve wide viewing angle [92]. Such a system possesses advantages in wide view and negligible color shift and gamma shift [93]. Our FRP is laminated on top of LGP. The design principles and working mechanisms of FRP are discussed as follows.

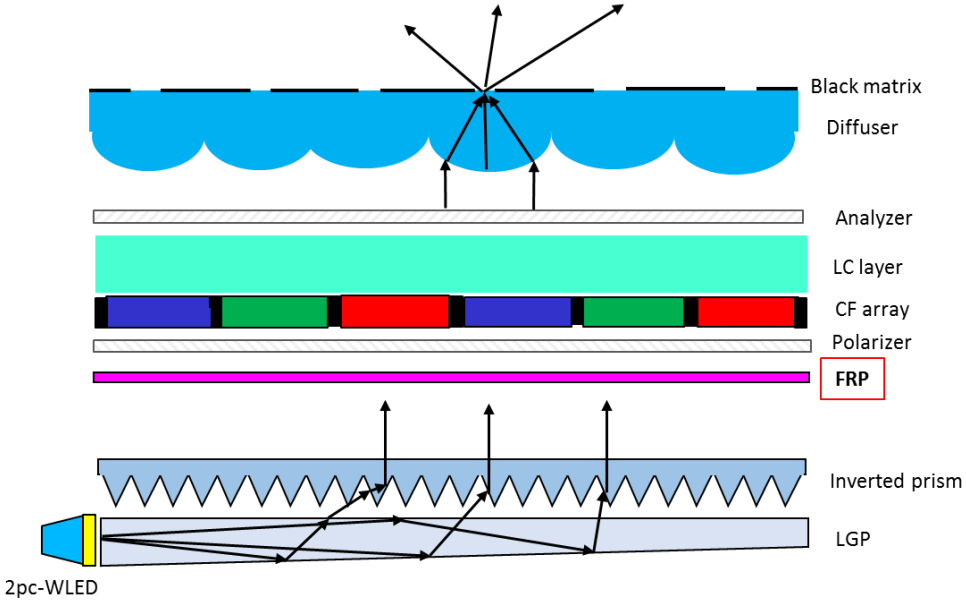

Figure 3.2. Schematic diagram of the system design with a functional reflective polarizer. (LC: liquid crystal, CF: color filter, FRP: functional reflective polarizer, and LGP: light guide plate)

Figure 3.3(a) shows the schematic diagram of a conventional reflective polarizer [89], where in *x*-axis the refractive index alternates between n_1 and n_2. This multi-layered structure exhibits broadband reflection due to the constructive/destructive interferences. While in *y*-axis, there is no change in refractive index, enabling 100% transmittance for the *y*-polarized backlight [Figure 3.3(b)]. Such a reflective polarizer has been widely used in LCD backlight system to enhance the optical efficiency by recycling the disallowed polarization. Here, we modify this structure slightly. As Figure 3.3(c) depicts, it is a multi-layered structure in both axes. In *x*-axis, it

works as a broadband reflector, but in *y*-axis it is designed to function as a notch filter. The transmission spectrum is shown in Figure 3.3(d), where the reflection bands could be tuned to block the unwanted spectrum. The detailed design principle of FRP has been reported in Ref. [90]. Generally speaking, transfer matrix is employed to calculate the transmission and reflection spectra based on multi-layer constructive/destructive theory.

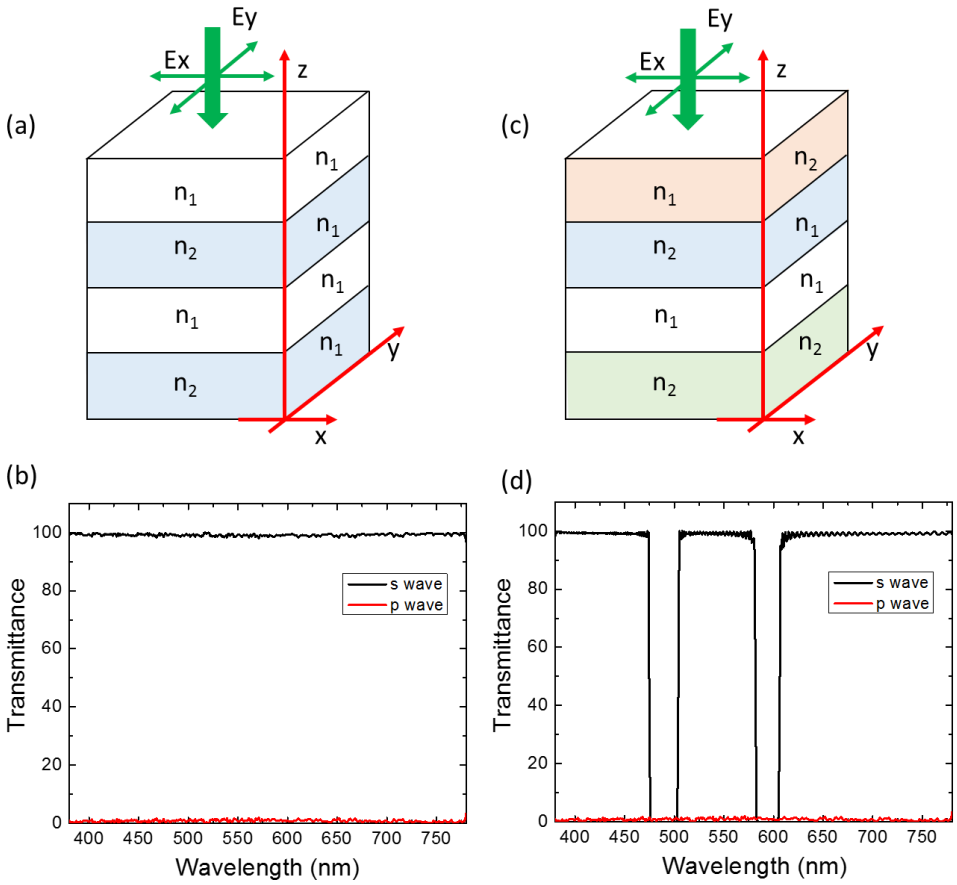

Figure 3.3. Schematic diagram of (a) conventional reflective polarizer and (b) functional reflective polarizer; Transmission spectrum of (b) conventional reflective polarizer and (d) functional reflective polarizer.

Regarding device fabrication, for conventional reflective polarizers two polymeric materials are commonly used: one is an isotropic film with refractive index n_1 (e.g. NOA81; n_1

=1.57) and another is a uniaxial film with $\Delta n = n_2 - n_1$ (e.g. BL038 LC polymer; n_2 = 1.82 and n_1 = 1.57) [89, 90]. For the proposed FRP, we need one more isotropic material with refractive index n_2. In our calculations, we choose polyferrocenes with n = 1.82 [90, 94].

3.1.2 Simulation results

Next, we integrate our FRP with 2pc-WLED backlight, and the output spectrum is plotted in Figure 3.4(a). The reflection band of FRP is specifically designed to block the crosstalk regions originated from 2pc-WLED and RGB color filters. For simplicity, here we assume the bandwidth of two reflection bands is equal, i.e. $\Delta\lambda_1 = \Delta\lambda_2 = 30$ nm. Of course, they can be different for practical applications, depending on the 2pc-WLED spectrum employed. After passing through FRP, the red, green and blue lights are well separated [Figure 3.4(a)]. Then we calculate the output spectrum considering the LC layer dispersion and color filter absorption, the obtained results are plotted in Figures 3.4(b) to 3.4(d) [33, 76, 77]. As expected, the crosstalk for each color is greatly reduced; especially for green and red, the light leakage is almost completely eliminated. Even for blue light, the crosstalk bump in the green region is partially blocked. It could be further improved by tuning the reflection band or enlarging the reflection bandwidth. As will be discussed later, the trade-off is lower transmittance.

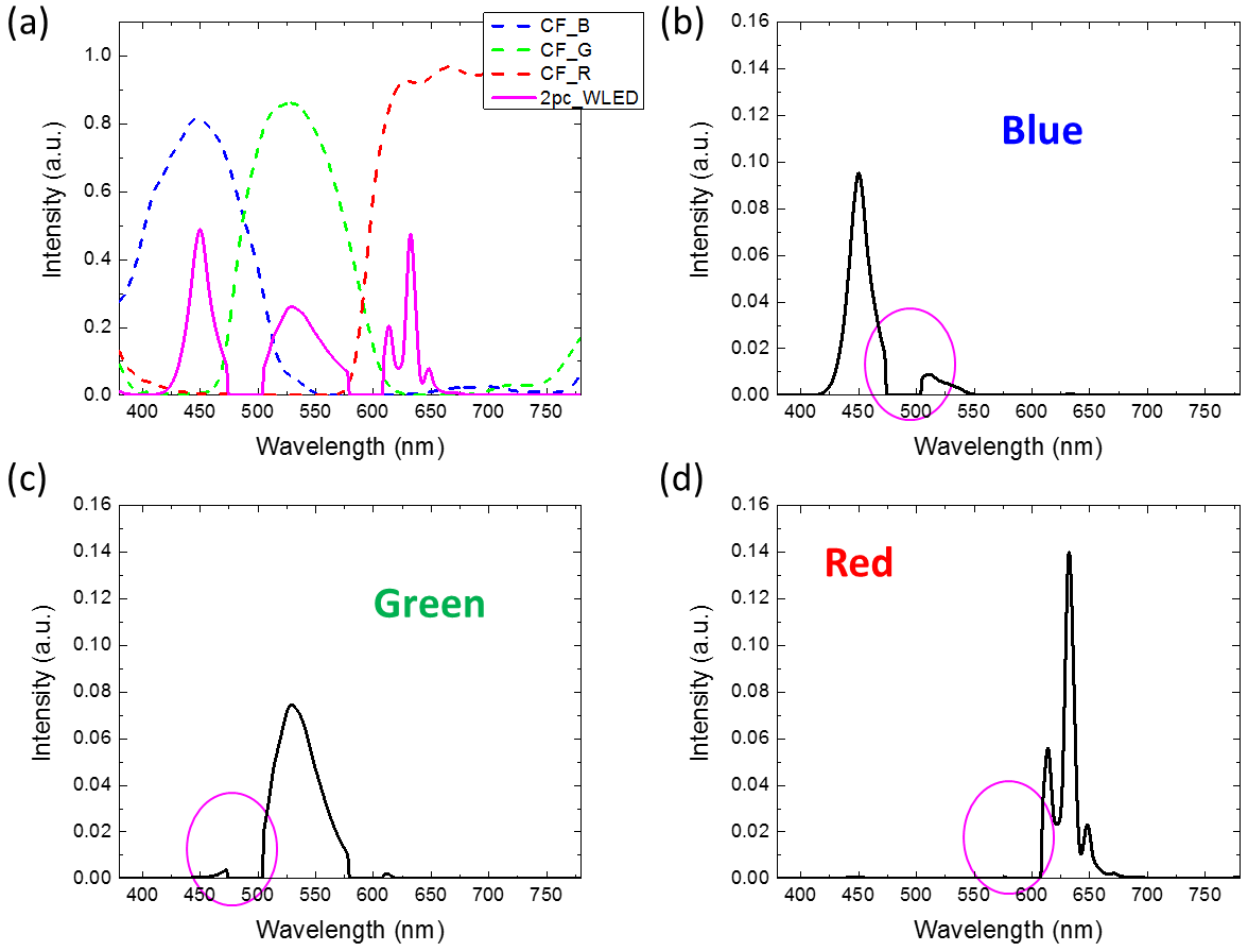

Figure 3.4. (a) Output spectrum after FRP; (b)-(d) Output spectrum for blue, green and red sub-pixels, respectively.

Figures 3.5(a) and 3.5(b) show the simulated color gamut at CIE 1931 and CIE 1976 color space, respectively. From these two figures, we can see clearly that color gamut is widened because of purer three primary colors. As usual, NTSC is adopted as the evaluation matric, and the calculated color gamut increases from 96.7% to 105.0% in CIE 1931 color space, and from 112.9% to 125.4% in CIE 1976 color space. This is a record high color gamut for the 2pc-WLED based backlight. However, the optical efficiency is decreased by 8.1% because our FRP blocks some unwanted spectrum.

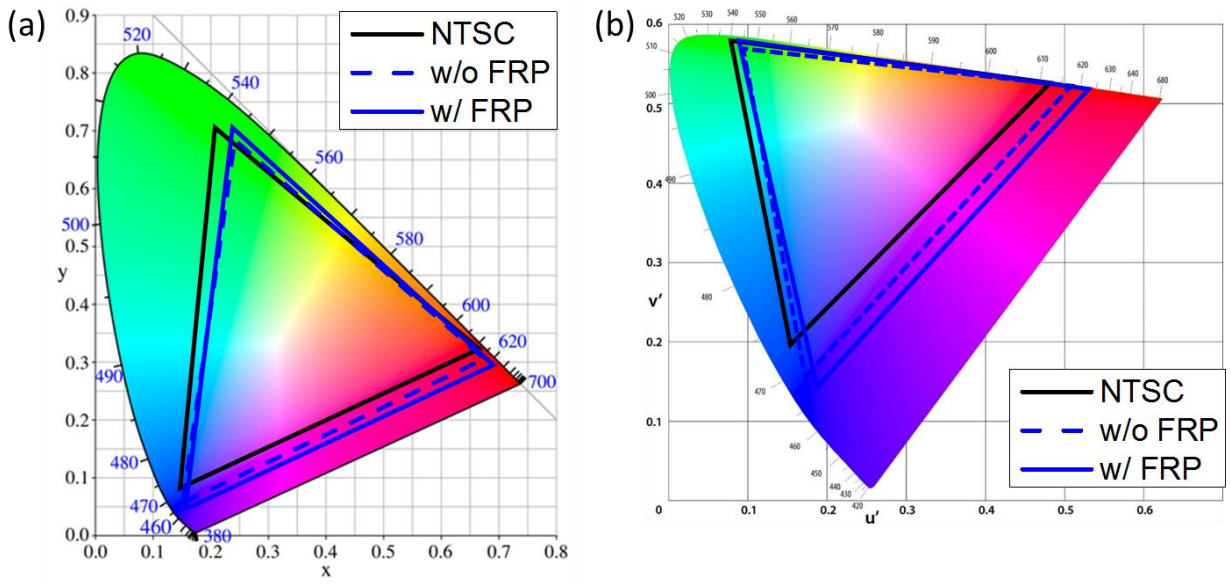

Figure 3.5. Simulated color gamut for 2pc-WLED with and without FRP in (a) CIE 1931 and (b) CIE 1976 color space.

For practical applications, both color gamut and optical efficiency need to be optimized. The optical efficiency is mainly governed by the output spectra power density (SPD). The SPD directly determines the luminous efficacy of radiation (*LER*) of the system [33, 76]:

$$LER = \frac{K_m \int S_{out}(\lambda) V(\lambda) d\lambda}{\int S_{out}(\lambda) d\lambda}, \tag{3.1}$$

where $S_{out}(\lambda)$ is the SPD of the output light, $V(\lambda)$ is the standard luminosity function, and K_m = 683 lm/W is the *LER* of the ideal monochromatic 555-nm source. As the *LER* is only determined by the light spectra, it sets the theoretical limit for the total efficiency of a display.

For a non-emissive display such as LCD, the SPD of the backlight ($S_{in}(\lambda)$) and the actual output light ($S_{out}(\lambda)$) can be modulated dramatically, depending on the transmission characteristics of the system. To quantify the transmission characteristics of the system, we introduce the transfer efficiency (*TE*) of the system as:

$$TE = \frac{\int S_{out}(\lambda)d\lambda}{\int S_{in}(\lambda)d\lambda}. \tag{3.2}$$

Then the total light efficiency (*TLE*) of the system is:

$$TLE = LER \cdot TE = \frac{K_m \int S_{out}(\lambda)V(\lambda)d\lambda}{\int S_{in}(\lambda)d\lambda}. \tag{3.3}$$

In our analysis, *TLE* is used as the main evaluation metric to quantify the optical efficiency. To make it more representative, all the efficiencies are normalized to the original 2pc-WLED backlight without FRP. It is worth mentioning that the decreased optical efficiency is mainly from blocking the unwanted light. The main red, green and blue spectra remain unchanged.

Table 3.1. Simulated color gamut and optical efficiency for the 2pc-WLED based LCDs with different FRPs.

$\Delta\lambda_1 = \Delta\lambda_2$	Color Gamut (NTSC)		Efficiency
	CIE 1931	CIE 1976	
Original 2pc-WLED	96.7%	112.9%	1
10 nm	98.8%	117.0%	0.973
20 nm	101.9%	121.0%	0.952
30 nm	105.0%	125.4%	0.919
40 nm	108.6%	133.9%	0.839
50 nm	109.8%	141.3%	0.738
QD	108.0%	124.6%	NA

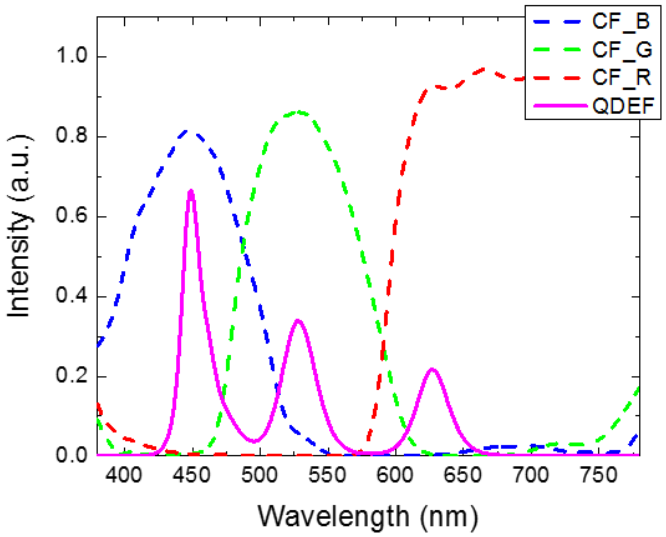

Figure 3.6. Measured spectrum of a quantum dot enhancement film (QDEF) from EFUN Technology (Taiwan).

Next, we investigate how the reflection bandwidth of FRP affects color gamut and optical efficiency. Table 3.1 lists the simulated results. In our calculations, we assume the same reflection bandwidth, i.e. $\Delta\lambda_1 = \Delta\lambda_2$. As the bandwidth increases, the RGB colors are separated farther, leading to less crosstalk and wider color gamut. As a comparison, here, a quantum-dot enhanced backlight is also considered. Its spectrum is plotted in Figure 3.6, and calculated color gamut using the same color filter is summarized in Table 3.1.

For 2pc-WLED with $\Delta\lambda_1 = \Delta\lambda_2 = 40$ nm, a color gamut of 108.6% NTSC in CIE 1931 is realized, which is comparable to that of Cd-based QD. If CIE 1976 is considered, the obtained color gamut is boosted to 133.9%, which even outperforms the QD-enhanced backlight. However, the incurred optical loss is about 16%. This is because the FRP blocks some unwanted spectrum from the 2pc-WLED. From Table 3.1, $\Delta\lambda_1 = \Delta\lambda_2 = 30$ nm seems to be a good compromise.

3.1.3 Discussion

For all the multi-layered films using constructive/destructive interferences, angular dependence is a big issue. Our FRP shares the same concern [89, 90]. As the incident light deviates from normal, the transmission spectrum of FRP would shift toward the shorter wavelength region, as Figure 3.7 shows. Thus, it is preferred to use a directional backlight in our design. Such a backlight (with FWHM~20°, i.e. ±10°) has been developed and commercialized successfully. The backlight power is confined within ±20°. From Figure 3.7, the reflection band shifts ~2 nm when the incident angle is 10°, and it increases to 7 nm as the incident angle increases to 20°. Such a small band shift is still tolerable for a directional backlight.

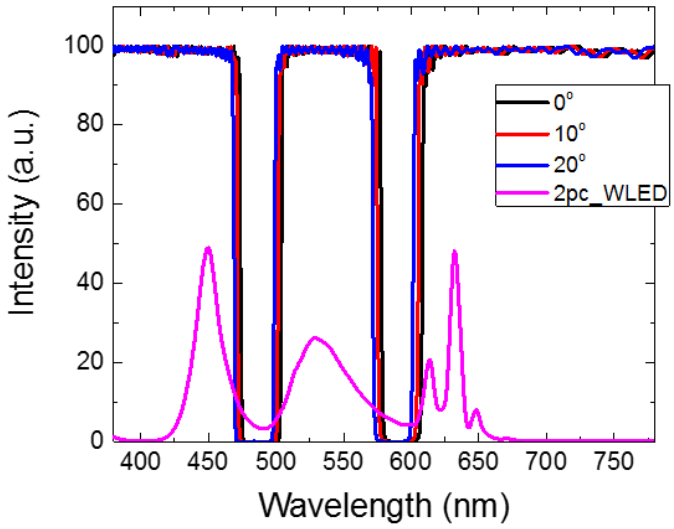

Figure 3.7. Transmission spectrum of FRP for different incident angles.

Figure 3.8(a) depicts the color gamut as a function of incident angle. In the CIE 1931 color space, color gamut increases by 1.7% (from 105.0% to 106.7% NTSC) as the incident angle increases from 0° to 20°. While in CIE 1976, it is slightly decreased from 125.4% to 122.4% NTSC. As for the efficiency, it decreases slightly from 91.9% to 91.0% [Figure 3.8(b)]. Therefore,

our FRP works quite well for a directional backlight. If a front diffuser is employed, wide viewing angle, and unnoticeable color shift and gamma shift can be achieved [93].

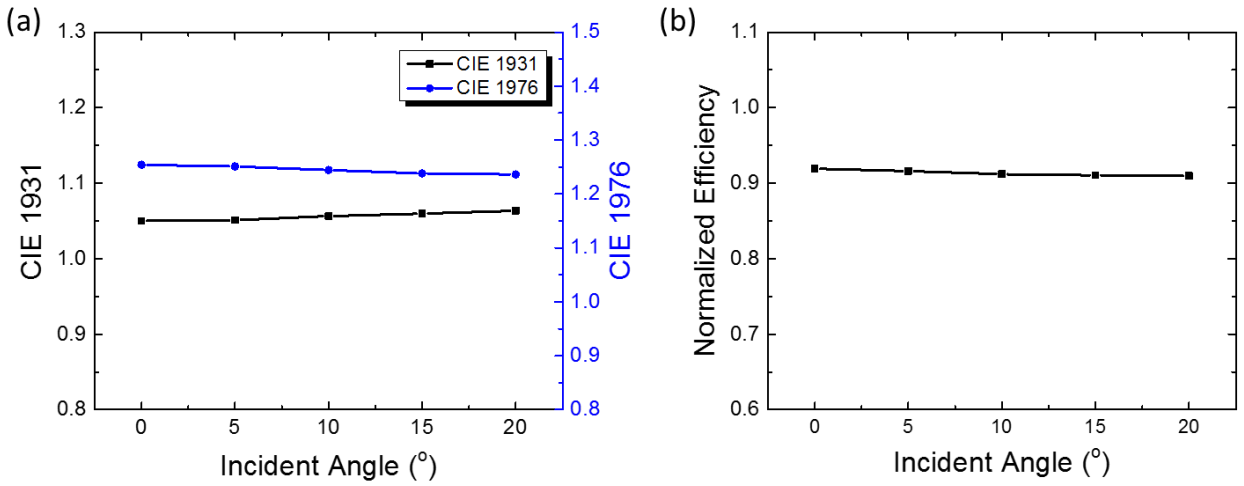

Figure 3.8. (a) Color gamut and (b) optical efficiency as a function of incident angle.

3.2 Going beyond the limit of an LCD's color gamut

As discussed above, reducing the bandwidth of light source is an effective approach to widen the color gamut. This is indeed what LCD industry adopts in the past two decades, from 1pc-WLED (FWHM ~ 120 nm) to 2pc-WLED (FWHM ~ 50 nm), and then to QDs (FWHM ~ 25-30 nm) [33]. Recently, organic-inorganic perovskite (OIP) is found to have a narrower FWHM (~ 18-20 nm) than QDs [95, 96]. As a result, it holds potential to further enhance the color gamut of an LCD. But an interesting question to ask is: Is there a theoretical limit in LCD's color gamut even if the light-emitter's FWHM is approaching zero, or < 1 nm like lasers?

Besides backlight, narrow-band color filter (CF) is another option to enlarge color gamut, except that the optical efficiency is compromised [77]. The state-of-the-art QD-enhanced backlight, along with specially designed narrow-band CFs, could achieve 92% Rec.2020 [97], but the tradeoff is ~25% reduced efficiency. For a battery-powered display, this 25% light efficiency loss

is hardly acceptable. Therefore, new approach to achieve wide color gamut while keeping high optical efficiency is urgently needed.

In this part, we first investigate how the FWHM of a light source affects LCD's color gamut, and find a theoretical limit even if FWHM approaches 1 nm [98]. Next, we propose a new backlight system incorporating a functional reflective polarizer and a patterned half-wave plate to suppress the crosstalk originated from color filters, which in turn significantly widens the color gamut [98]. In experiment, we prepared a white-light source using a blue LED to pump green OIP-polymer composite film and red QD, and demonstrated an exceedingly wide color gamut: 95.8% Rec. 2020 in CIE 1931 color space, and 97.3% Rec. 2020 in CIE 1976 color space, with commercial high-efficiency color filters. Our result is comparable to that of laser projection displays, but with direct-view LCD panels. Besides quantum dots and perovskites, our design also works well for other light sources, like 2pc-WLED.

3.2.1 Gaussian fitting effect

Figure 3.9 shows the measured spectra of blue LED, green OIP and red QD. All of them exhibit Gaussian-like profiles. Thus, Gaussian fitting is commonly conducted to extract the peak emission wavelength and FWHM [76, 77]. These fitted curves are then employed to calculate the color gamut by neglecting the fitting discrepancy. Through fittings, we obtained the [peak wavelength, FWHM] of three primary colors as follows: [λ_B = 450.4 nm, $\Delta\lambda_B$ = 20.3 nm], [λ_G = 531.6 nm, $\Delta\lambda_G$ = 19.7 nm] and [λ_R = 630.8 nm, $\Delta\lambda_R$ = 24.4 nm]. From Figure 3.9, a noticeable discrepancy is observed, especially for the blue LED. As for red QD and green OIP, they present longer emission tails than the fitted Gaussian functions. As will be shown later, it is these tails aggravate the color crosstalk, which in turn shrinks the color gamut.

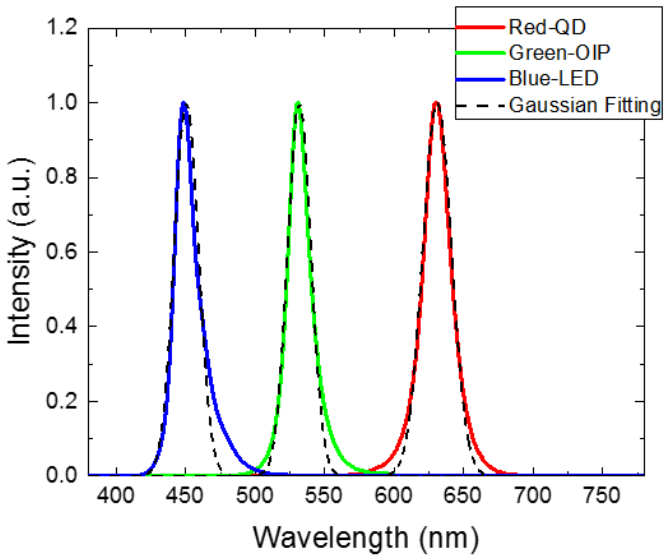

Figure 3.9. Emission spectra for blue LED, green perovskite and red QD. Solid lines are measured data, and dashed lines are from Gaussian fittings.

In an LCD, the backlight passes through the LC layer and color filters before reaching the viewer. Therefore, we have to incorporate the backlight spectra [Figure 3.9] into the LCD panel in order to calculate the output spectral power distribution (SPD). In our simulation, we chose a fringe field switching (FFS) LCD with negative dielectric anisotropy ($\Delta\varepsilon < 0$) LC and a commercial color filter array as an example [Figure 3.10(a)]. Such an LCD has been widely used in smartphones and pads [4, 29]. The wavelength dependent refractive indices of the employed LC are also considered in the simulation. Figures 3.10(b) to 3.10 (d) depict the obtained SPD for the RGB primary colors with or without Gaussian fitting. In both cases, light leakage for all three channels are observed clearly; especially for the blue channel, where a fairly large bump leaks through the green color filter. For the real spectrum without Gaussian fitting, the light leakage is even worse, owing to the long emission tails, which would further deteriorate the color purity.

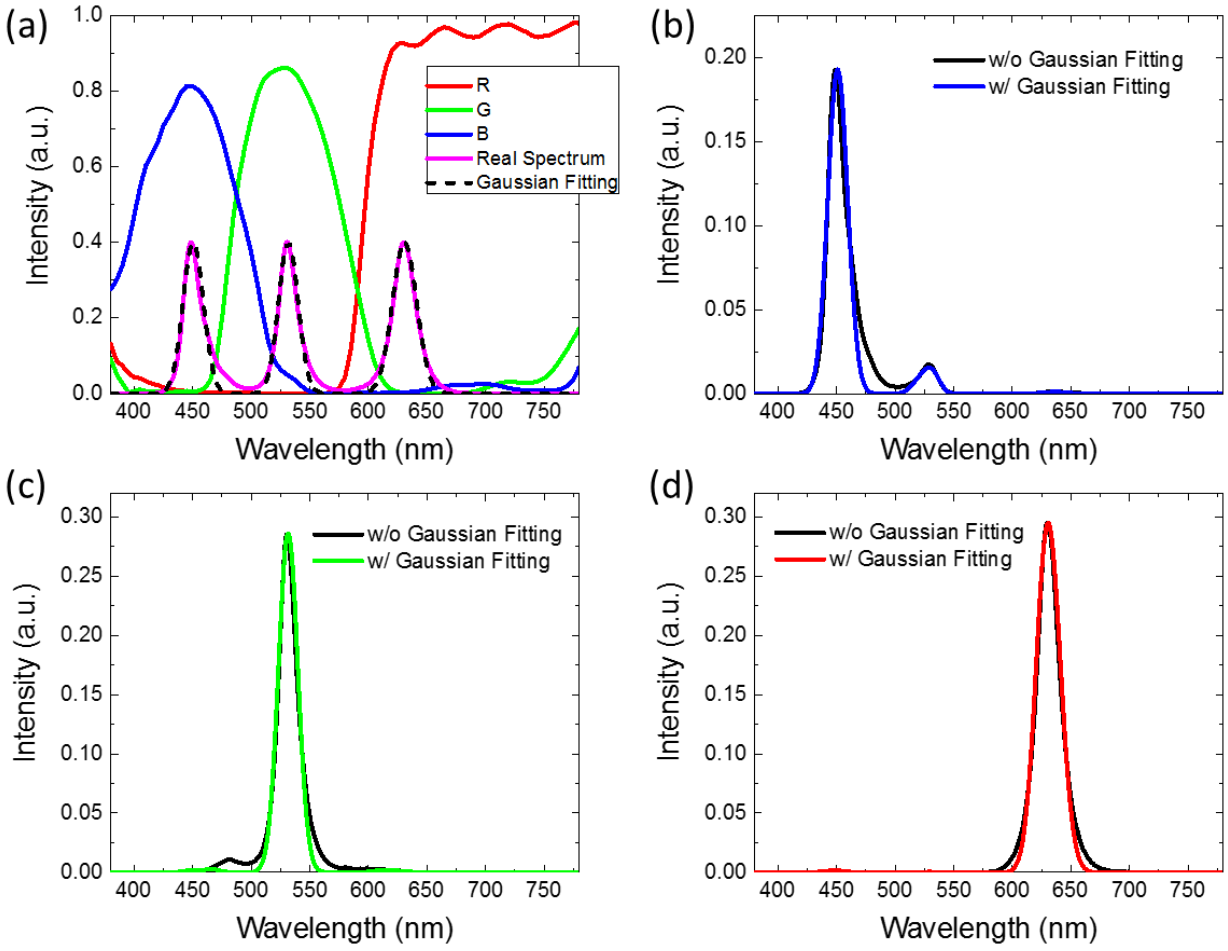

Figure 3.10. (a) Transmission spectra for a commercial color filter array; Output SPDs for (b) blue, (c) green and (d) red primary colors with and without Gaussian fitting.

Figure 3.11 illustrates the color gamut shrinkage more clearly. In both color spaces, green and blue color coordinates with Gaussian fitting expand outwards, representing high purity primary colors. The obtained color gamut results are summarized in Table 3.2.

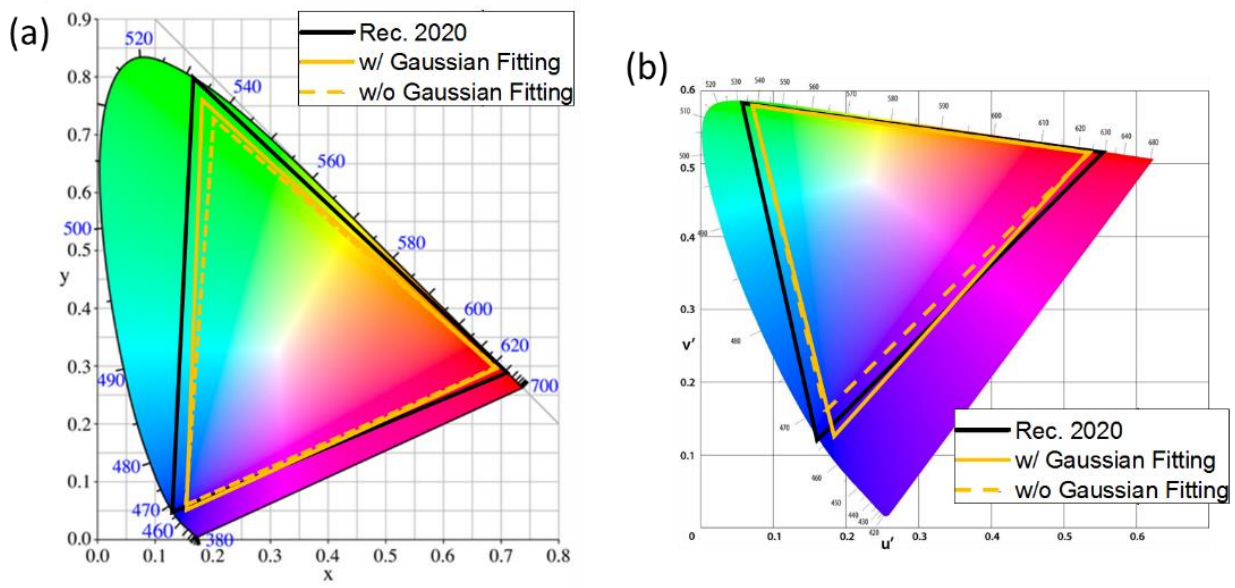

Figure 3.11. Color gamut in (a) CIE 1931 color space and (b) CIE 1976 color space.

In CIE 1931 color space, the color gamut with Gaussian fittings is 6.6% wider than that using the real spectra, while in CIE 1976 this difference is 6%. For different color filters and light sources, this discrepancy varies. But it is for sure that Gaussian fitted curves lead to a wider color gamut than using the real emission spectra. Therefore, to establish the theoretical limit of an LCD's color gamut, we choose to use the Gaussian-fitted spectra.

Table 3.2. Simulated color gamut for the light source with and without Gaussian fitting.

	Rec. 2020	
	CIE 1931	CIE 1976
w/ Gaussian Fitting	89.4%	89.9%
w/o Gaussian Fitting	82.8%	83.9%

3.2.2 Pareto front for the color gamut and light efficiency

From Table 3.2, the color gamut without Gaussian-fitted spectra is ~ 83% Rec. 2020. To improve that, we need to fine-tune the emission spectrum of QD and OIP to match the transmission bands of color filters, as Figure 3.12 shows. However, tuning the peak emission wavelength would influence the light efficiency, because human eye has different sensitivities to different colors. This is governed by the human eye sensitivity function $V(\lambda)$, which peaks at 555 nm. Therefore, we choose total light efficiency (*TLE*), described by Eq. (3.3), to characterize how much input light transmits through the LCD panel and finally gets converted to the brightness perceived by the human eye [33, 76].

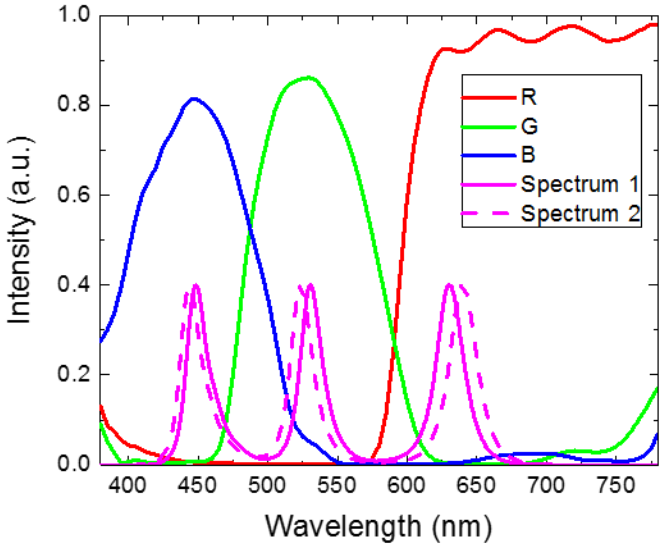

Figure 3.12. Transmission spectra of commercial color filters and different white light sources.

Both color gamut and *TLE* are important parameters for a display device. For such a multi-objective problem, different objectives may be mutually exclusive. That means, any further improvement of one objective (e.g. color gamut) is likely to be compromised by the degradation of another objective (e.g. *TLE*). Therefore, a Pareto front is commonly employed, and all the

solutions will fall either on or below this Pareto front [99]. Figure 3.13 is a plot of the calculated Pareto fronts of the LCD using backlight with different FWHM values.

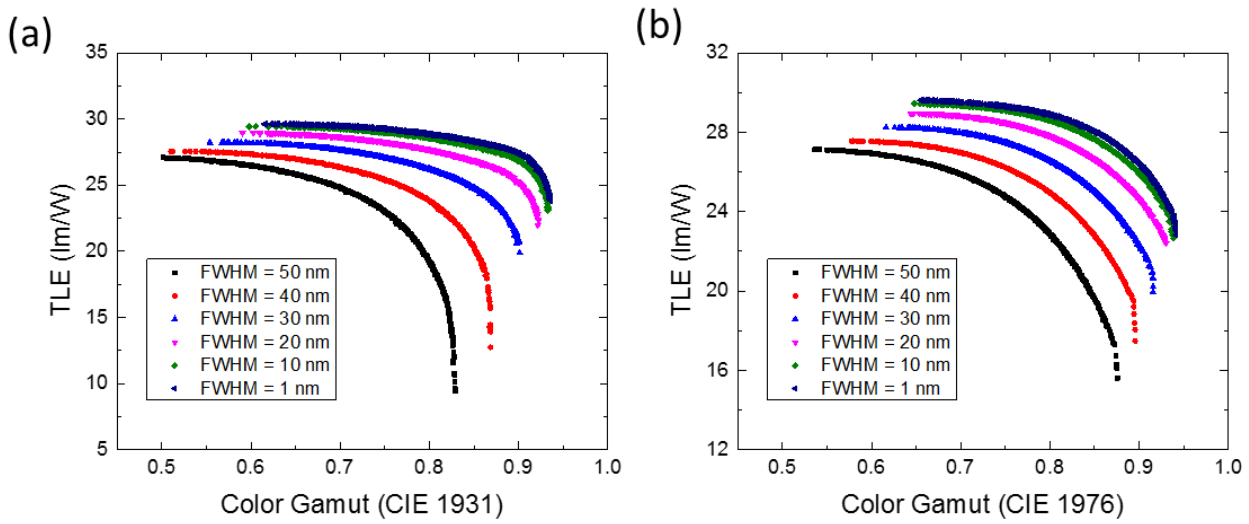

Figure 3.13. Pareto front defined in (a) CIE 1931 and (b) CIE 1976 with different FWHM light sources.

From Figure 3.13, several interesting phenomena are found. Firstly, there exists an inherent tradeoff between light efficiency and color gamut. Thus, a delicate balance should be chosen in practical applications. Secondly, for backlight with the same FWHM, there is indeed a theoretical limit for the color gamut regardless of the RGB central wavelengths. For example, when the FWHM of QD or OIP emission spectrum is 30 nm, the largest achievable color gamut is 90.1% Rec. 2020 in CIE 1931 [Figure 3.13(a)], or 91.5% Rec. 2020 in CIE 1976 [Figure 3.13(b)]. Next, we find that as the light source becomes more saturated (i.e. narrower FWHM), the maximum color gamut increases and then gradually saturates. Currently, the commercial Cd-based QD-enhanced backlight exhibits a 30-nm FWHM, and it could reach 25 nm in the next few years. Let us assume that 20 nm can obtained someday. According to Figure 3.13, the color gamut improvement is only 2%. Even if the FWHM of the light emitters were laser-like (≤ 1 nm), the

maximum color gamut is ~93.5% Rec. 2020. This limits the color gamut that an LCD can possibly achieve. Please note that this limit is obtained with Gaussian fitted spectra; it would be lower if real spectra are used.

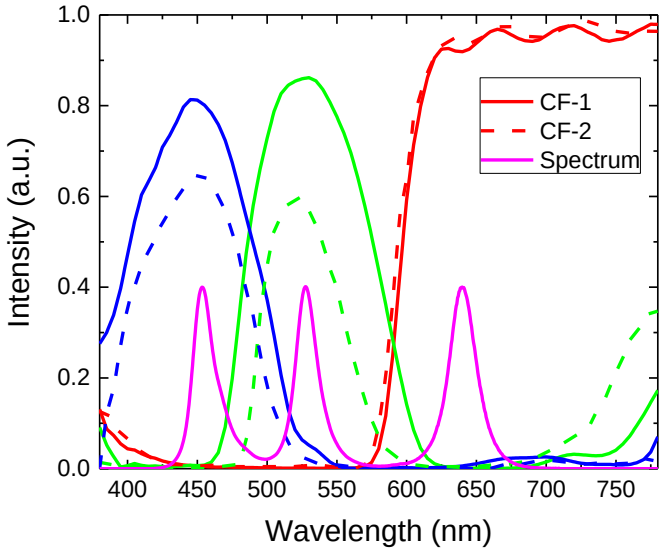

Figure 3.14. Transmission spectra of two commercial color filters and a white light source.

Next, we examine the color filter effect, as shown in Figure 3.14. The results shown in Figure 3.13 are based on CF-1; it has high transmittance, but a relatively large overlap in the blue/green and green/red regions. On the other hand, CF-2 possesses a smaller crosstalk, but its transmittance is about 25% lower in the blue and green regions. Again, we carry out the optimizations using CF-2 and plot the Pareto front results in Figure 3.15. The trend is similar to that in Figure 3.13, but with a wider color gamut. Due to the suppressed light leakage, its color gamut reaches 93.1% Rec. 2020 when a 30-nm FWHM backlight is employed. If we reduce the FWHM to 20 nm, this limit is increased to 94.9% Rec. 2020. However, when the real spectrum is employed, the color gamut should be narrower due to the abovementioned Gaussian fitting effect. In comparison with CF-1 [Figure 3.13], CF-2 suffers 25% in optical efficiency but only gains 2.7%

in color gamut. Such a tradeoff may not be worth taking, especially for the battery-powered mobile display devices.

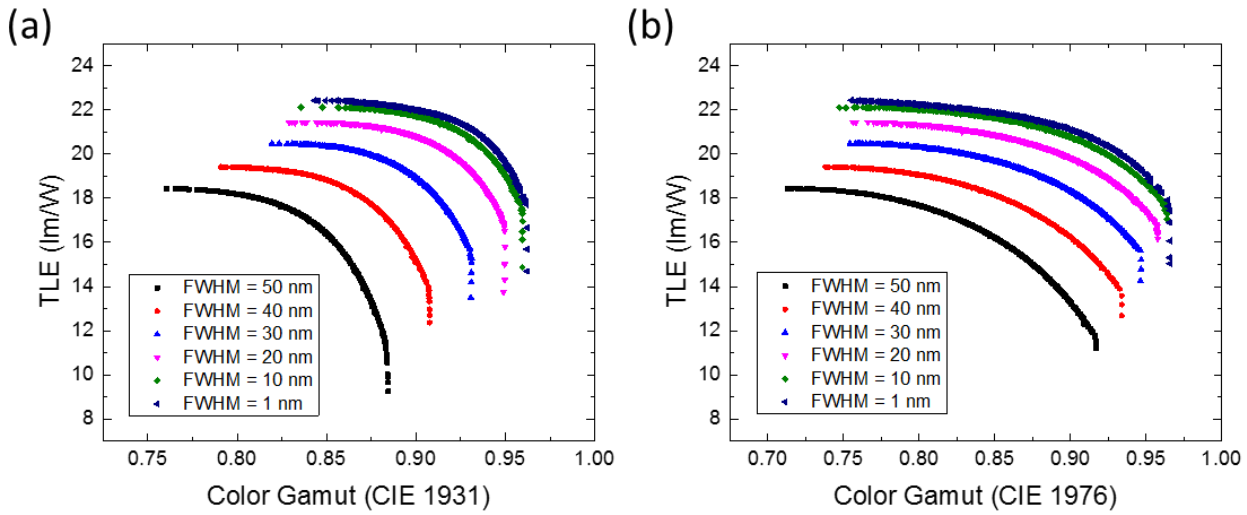

Figure 3.15. Pareto front defined in (a) CIE 1931 and (b) CIE 1976 using CF-2.

So far, we have found the theoretical limit of an LCD's color gamut, as shown in Figure 3.13 and Figure 3.15. It is jointly determined by the light source (central wavelength and FWHM) and the color filters (crosstalk). Even if we reduce the backlight's FWHM to 1 nm, the color gamut is still limited by the crosstalk of the blue/green and green/red color filters [Figure 3.10]. Narrowing the transmission bands (CF-2) could mitigate this issue, but not completely. Meanwhile, the optical efficiency is compromised substantially. This tradeoff may not be worth taking. Therefore, as long as the color filter technology makes no disruptive progress, the color gamut of an LCD will be limited, even if the backlight source exhibits laser-like narrow emission spectra.

3.2.3 Structure design

From above discussions, keep narrowing the emission spectrum of QD or OIP would eventually reach the theoretical limit, based on the predictions in Figure 3.13 and Figure 3.15. To overcome the barrier resulted from color filters, we propose a new backlight configuration, as

depicted in Figure 3.16. The key components are a functional reflective polarizer (FRP) and a patterned half-wave plate. They work together to suppress the unwanted light leakage caused by color filters [98].

From Figure 3.16, a high power blue LED is used to excite the quantum rail, consisting of red QD and green OIP-polymer composite film. Then, the advanced LCD system incorporating a directional backlight and a front diffuser is used again, just as the discussion in previous section [93]. Our FRP and patterned half-wave plate can be laminated on the top surface of the inverted prism film.

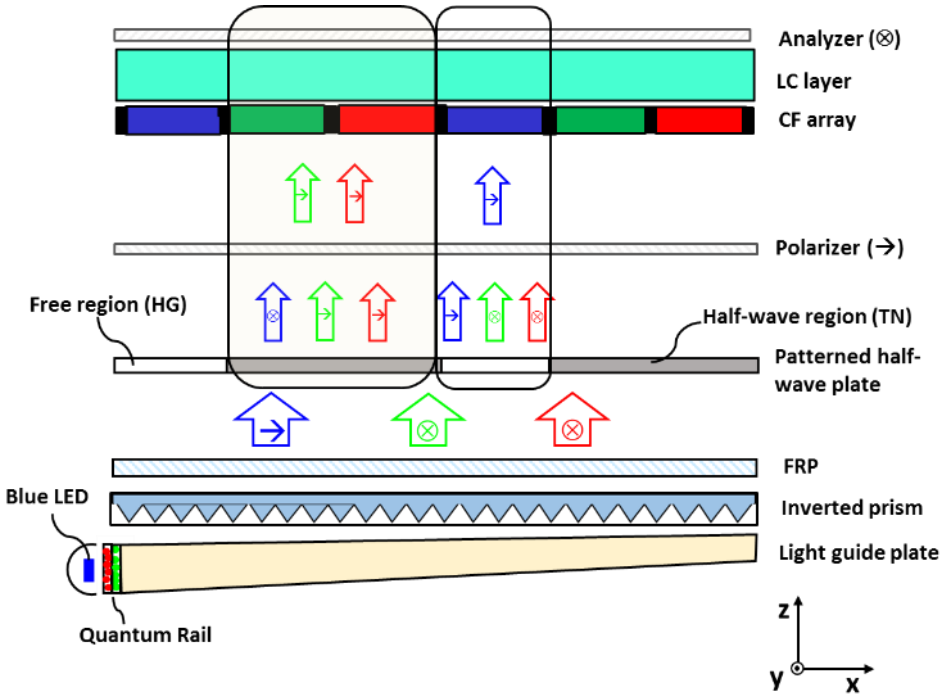

Figure 3.16. Schematic diagram and working principle of the proposed backlight with a functional reflective polarizer (FRP) and a patterned half-wave plate. (TN: twisted nematic alignment; HG: homogeneous alignment)

As discussed above, FRP is a multi-layer structure with alternative refractive indices (n_1 and n_2), as shown in Figure 3.3(c) [90]. Due to the constructive/destructive interferences, it

functions as a band-pass filter for both polarization directions (i.e. x-polarized and y-polarized). Here, in this design, its functions are designed as follows: For x-polarized incident light [Figure 3.17(a)], only short wavelength light (blue) could pass, whereas the rest is reflected. For y-polarized incident light [Figure 3.17(b)], it is reversed: only green and red lights could pass through FRP, while blue light is reflected. As a result, after FRP the polarization state of blue light is orthogonal to that of green/red lights [Figure 3.16]. Also, we study the angular dependent transmission of FRP. Results are shown in Figures 3.17(a) and 3.17(b). Within ±30° incidence, FRP could still separate the blue and green/red regions effectively. For a commercial directional backlight (with FWHM ~ 20°, i.e. ±10°), its optical power is mostly confined within ±20°. Therefore, our FRP works quite well regardless of the small band shift.

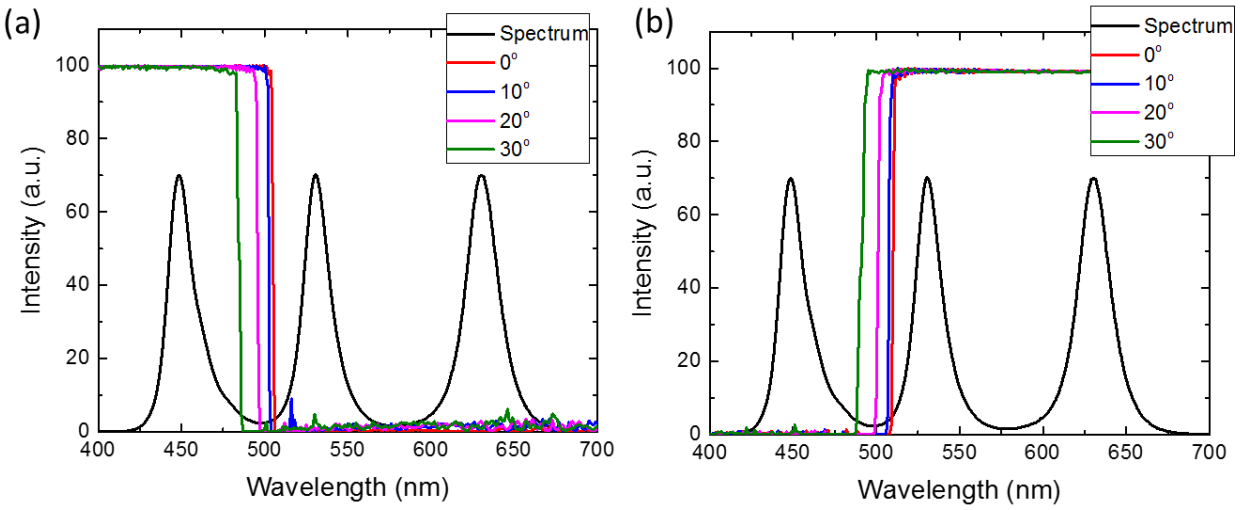

Figure 3.17. Angular dependent transmission spectra of (a) x-polarized incident light, and (b) y-polarized incident light.

Above FRP is a patterned phase retardation film, which is divided into half-wave region and free region. For the light traversing through the λ/2 region, its polarization is rotated by 90°, e.g. x-polarization turns to y-polarization or vice versa. If the light passes through the free region,

then its polarization remains unchanged. To achieve this goal, we employed a patterned LC phase retardation film. In the λ/2 region, the LC has 90° twist, while in the free region it has homogeneous (HG) alignment. The detailed structure and working principle are illustrated in Figures 3.18(a) and 3.18(b). With the help of photo-alignment technology [100, 101], we have successfully fabricated a patterned half-wave plate. The captured polarized optical microscope (POM) images under crossed and parallel polarizers are shown in Figures 3.18(c) and 3.18(d), respectively. As expected, it performs quite well.

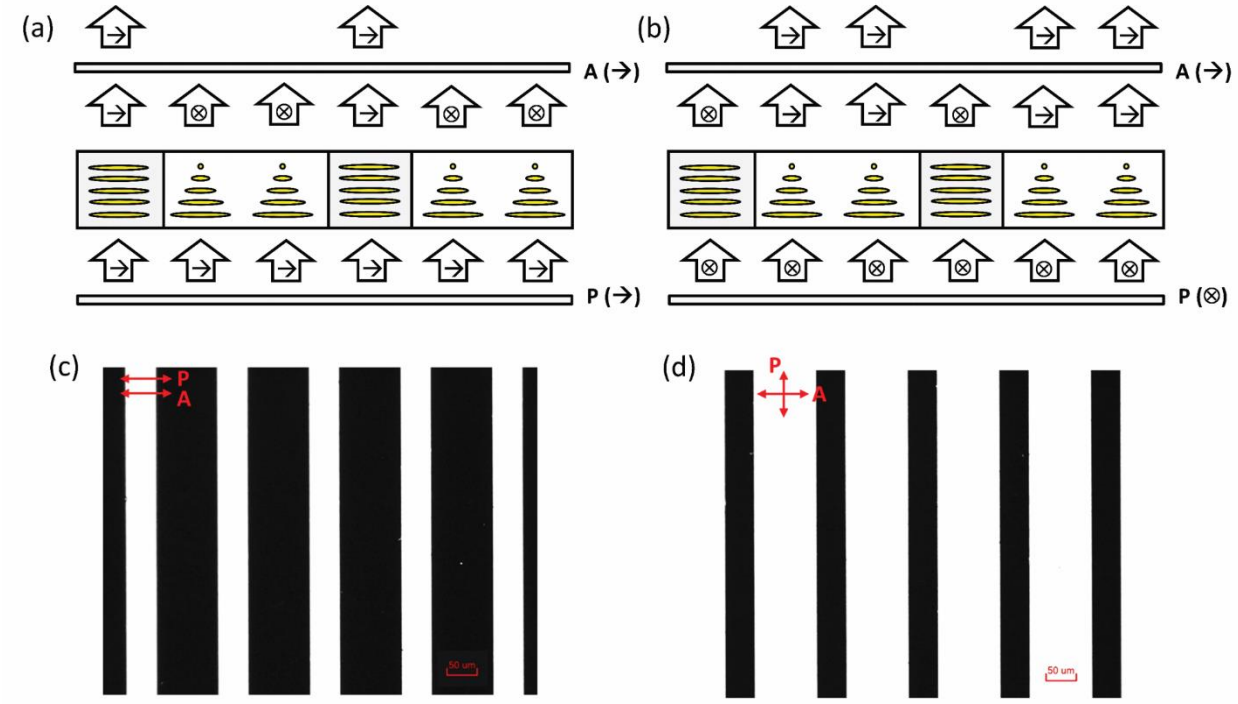

Figure 3.18. Working principle of a patterned half-wave plate for (a) x-polarized incident light and (b) y-polarized incident light; Captured POM images under (c) parallel polarizers and (d) crossed polarizers. (Scale bar: 50 μm; P: polarizer; A: analyzer)

For the system configuration shown in Figure 3.16, this patterned half-wave plate should register with the R/G/B sub-pixels. Here, the half-wave region is right below the green/red sub-pixels, and free region corresponds to the blue sub-pixel. After FRP, the blue light is polarized

along x-axis, while the green and red lights are along y-axis. After passing through the patterned half-wave plate, no change happens to the light in free region (corresponding to blue sub-pixel), which means blue light is still polarized along x-axis. On the other hand, in the half-wave region (corresponding to green and red sub-pixels), the polarization of outgoing lights changes 90°, turning to y-polarized blue light and x-polarized green/red lights. Therefore, R/G/B lights could traverse through the front linear polarizer (with transmission axis along x-axis) and enter the corresponding R/G/B sub-pixels. Please note that only blue light can enter the blue sub-pixels, because green/red lights are absorbed by the linear polarizer due to mismatched polarization. Similar situation occurs to the green and red sub-pixels. Therefore, *no crosstalk* exists between the blue and green/red regions, leading to a much wider color gamut.

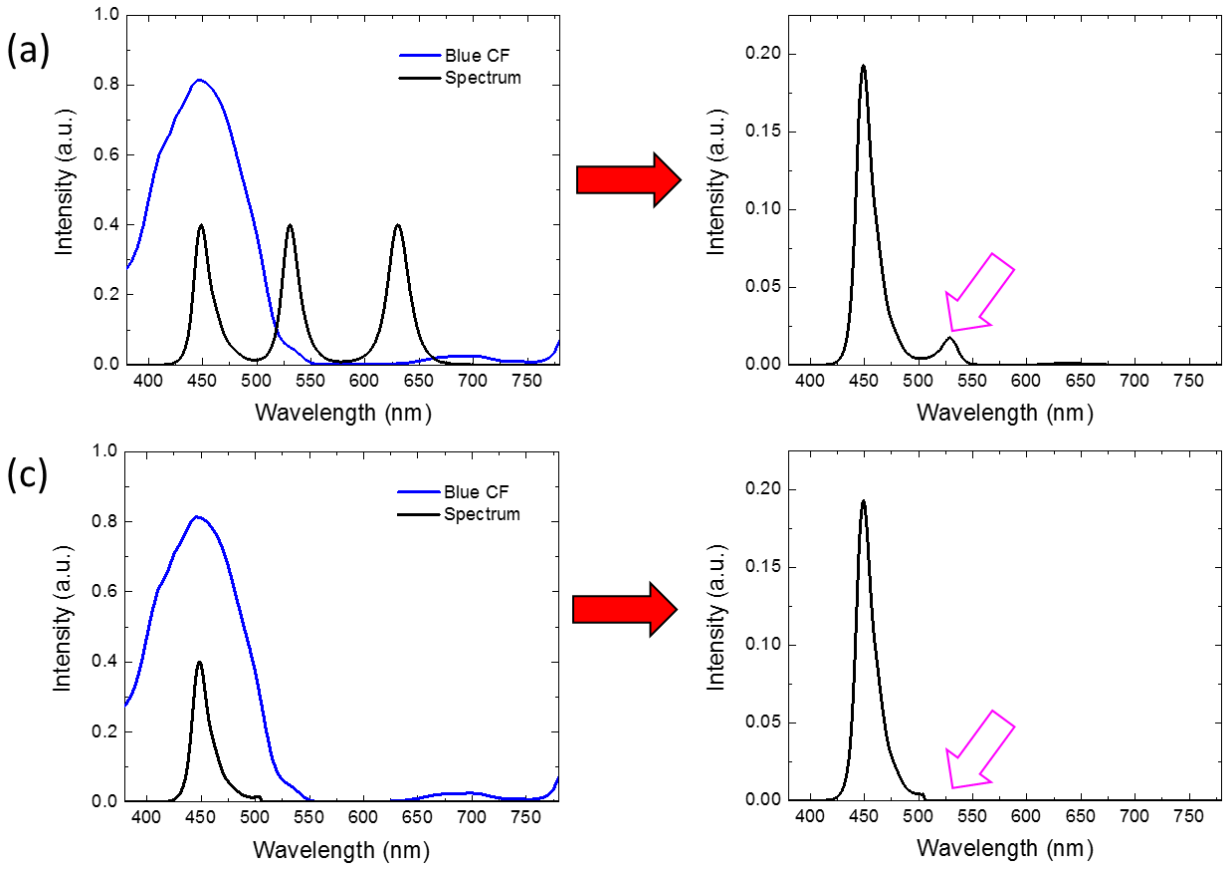

Figure 3.19. Output SPD of blue primary color for (a) conventional backlight, and (b) newly proposed backlight.

Figure 3.19 illustrate this effect. Let us assume the LCD backlight spectrum is shown in Figure 3.9. When the input white light (black line in Figure 3.19(a)) passes through blue color filter (blue line), there is noticeable light leakage in the green region (500 nm ~ 550 nm), which in turn deteriorates the color purity. But for our new structure with a patterned half-wave plate, blue light and green/red lights are decoupled in terms of polarization direction [98]. As discussed above, only blue light can enter blue color filter; the crosstalk in the green region is eliminated almost completely [Figure 3.19(b)]. Similarly, more saturated green and red primary colors are realized. Thus, the color gamut is enhanced from 82.8% to 89.0% Rec. 2020.

3.2.4 Experiment results

With the white light source shown in Figure 3.9, we can obtain 89% Rec. 2020. To further improve it, we need to choose the RGB central wavelengths carefully. In experiment, we tried multiple combinations of blue LED, green OIP and red QD to generate a desired white light. If we use Gaussian-fitted spectra, then it is fairly easy to simulate the color gamut before searching for suitable light source. However, the actual emission spectrum often contains a long tail and it is challenging to predict the final color gamut accurately. After dozens of experiments, we found an optimal combination, as plotted in Figure 3.20(a). The RGB color coordinates overlap quite well with Rec. 2020 standard, as Figures 3.20(b) and 3.20(c) show. The corresponding color gamut is 95.8% Rec. 2020 in CIE 1931, and 97.3% Rec. 2020 in CIE 1976. Here, high efficient color filter (CF-1 in Figure 3.14) is employed. Compared to the theoretical limit (93.5% Rec. 2020 for 1-nm FWHM) shown in Figure 3.13, we have successfully overcome this limitation for LCDs. At the

best of our knowledge, this is the record-high color gamut of an LCD. What's more, this is realized using commercial high-efficiency color filters, intended for TV applications.

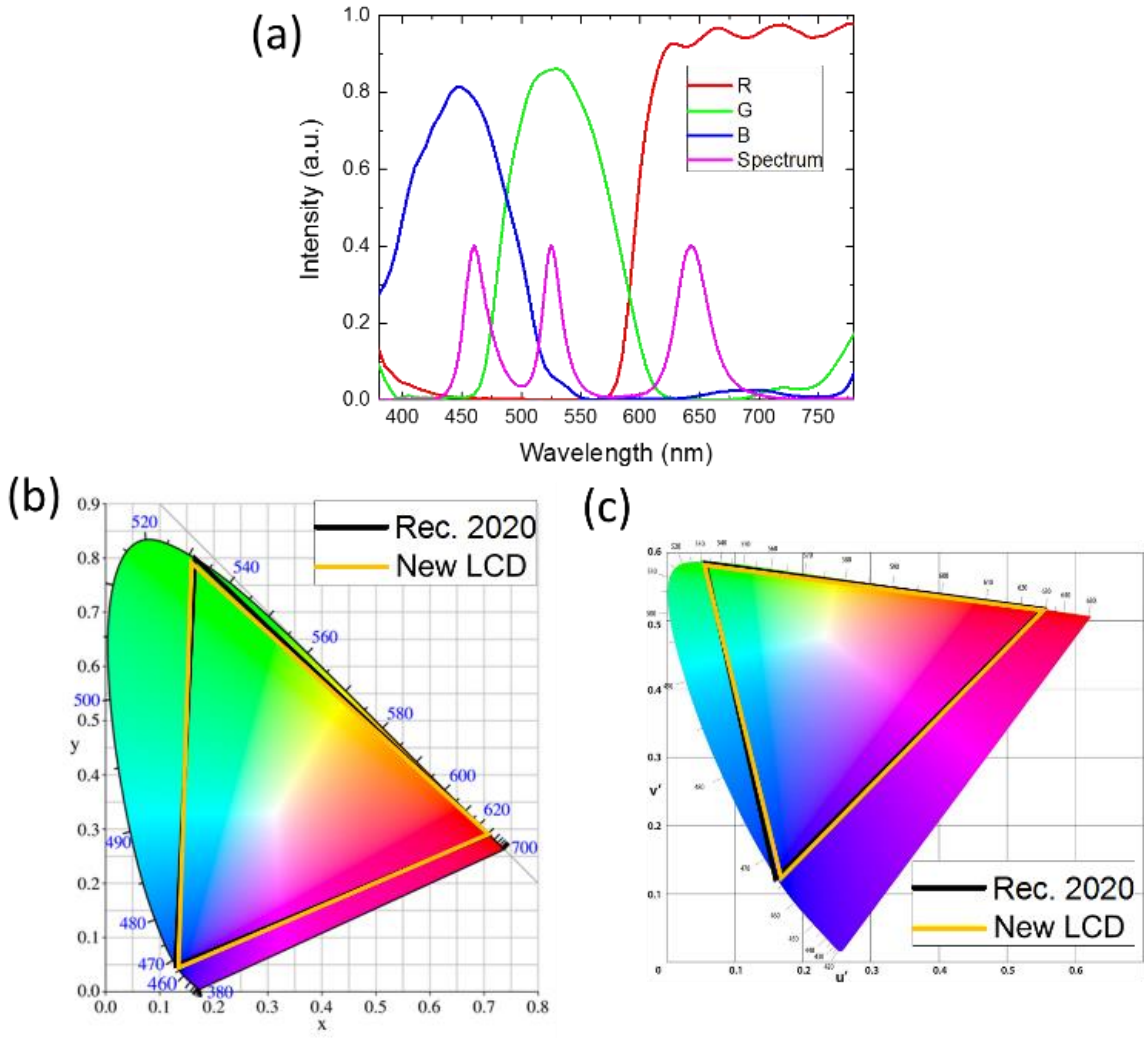

Figure 3.20. (a) Measured spectra for optimized white light source, and corresponding color gamut in (b) CIE 1931 color space and (c) CIE 1976 color space.

3.2.5 Discussion

So far, our design is aimed at breaking the color gamut limit of an LCD using QD/OIP-enhanced backlight. Next, we want to extend this approach to other backlight technologies, like 2pc-WLED. By packaging QD/OIP into an LED chip, both lifetime and quantum yield would be

sacrificed because of the high junction temperature [33]. Therefore, 2pc-WLED still holds the advantages in stability, long lifetime, low cost and simple optical configuration. The major drawback is its relatively broad green and red spectra, leading to 70%-80% Rec. 2020, depending on the employed color filter. When incorporating 2pc-WLED (β-sialon:Eu^{2+} as green phosphor and K_2SiF_6:Mn^{4+} as red phosphor) into our design, the color gamut can be enhanced from 80% to 89% using high efficiency CF-1 color filters, as Figure 3.21 depicts. If CF-2 is employed, the color gamut is boosted to 91.5% Rec. 2020, except that the light efficiency is decreased by about 25%. This enables 2pc-WLED to compete directly with the state-of-the-art Cd-based QD technology in terms of color performance.

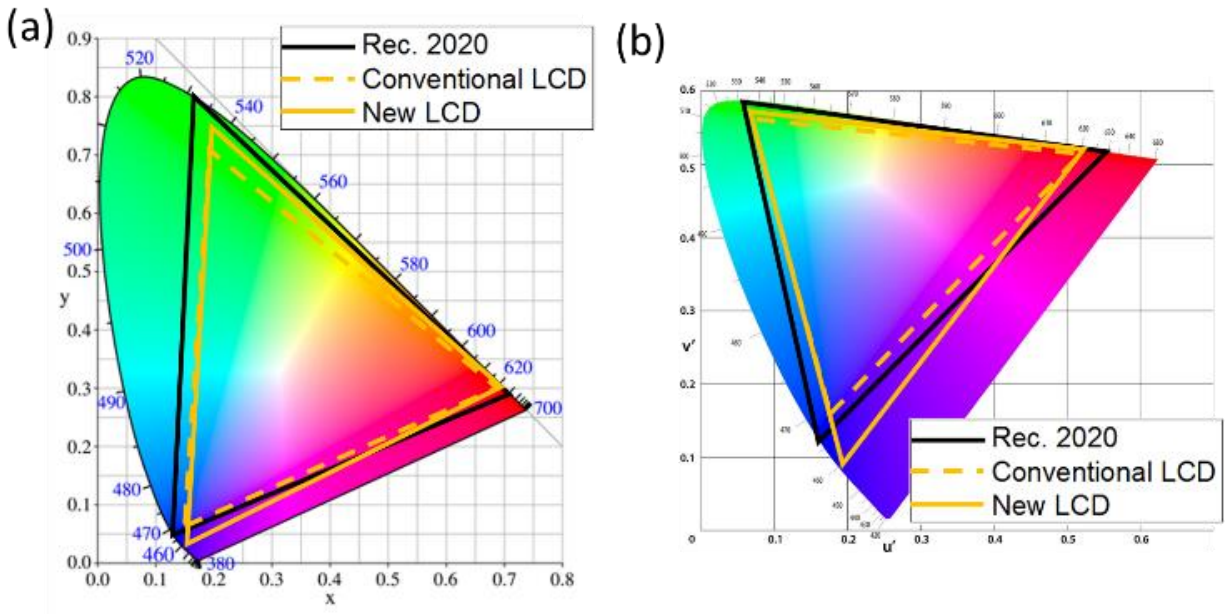

Figure 3.21. Color gamut defined in (a) CIE 1931 and (b) CIE 1976 using 2pc-WLED backlight. (CF-1 is used as color filter)

3.3 Summary

In this chapter, we analyze in detail how the backlight's peak wavelength, FWHM and color filters affect the color gamut of an LCD device. To get better color performance, we propose two novel backlight configurations. One is a simple yet efficient approach using a so-called functional reflective polarizer (FPR). It acts as a notch filter to block the light which would leak through the color filters, while transmitting the rest wavelength at high efficiency. When integrated with a commercial 2pc-WLED, the color gamut of the LCD can be improved from 96.7% to 108.6% NTSC in CIE 1931, or from 112.9% to 133.9% NTSC in CIE 1976, which is comparable to the cadmium-based quantum dot backlight. Our design offers an alternative approach to quantum dots, while keeping low cost, long lifetime, and high brightness.

Another approach is using a FRP and a patterned half-wave plate. The design decouples the polarization of blue light and green/red lights, which effectively suppresses the crosstalk between these color bands, thus, boosting the color gamut. In experiment, we prepared a white-light source using blue LED to pump green perovskite and red quantum dot, and demonstrated an exceedingly high color gamut (95.8% Rec. 2020 in CIE 1931 color space, and 97.3% Rec. 2020 in CIE 1976 color space) with commercial high-efficiency color filters. The results are beyond the color gamut limit that a conventional LCD can achieve.

CHAPTER FOUR: HIGH CONTRAST RATIO

4.1 Depolarization effect in an LCD panel

High contrast ratio (CR) is another equally important parameter to achieve supreme image quality. However, for a non-emissive LCD, its CR is inherently limited, due to the unwanted light leakage at voltage-off state. Currently, a commercial VA LCD TV shows CR ~ 5000:1, for FFS-based LCD smartphones and tablets, their CR is only ~2000:1. While for TN-based notebook and desktop computers, it is even lower (CR ~ 1000:1) [4].

To improve CR, increasing the polarizer thickness is a straightforward approach. However, more evidences reveal that polarizer is no longer the limiting factor [102-104]. In fact, it is fairly easy to get CR > 100,000:1 with two high-quality crossed polarizers, but the final CR of an LCD is still limited to 5,000:1, which is mainly governed by the depolarization effect inside the LCD panel. The origins for this depolarization are rather complicated [105-110], including diffraction effect, scattering effect, misalignment effect, etc. After extensive studies, the underlying physical mechanisms have been gradually understood, and their contributions to the total depolarization can be evaluated quantitatively [111, 112], as will be discussed later.

Although the depolarization effect has been verified experimentally and investigated systematically, how to incorporate this effect into the simulation model remains to be a big challenge [113]. Actually, for the commercial software DIMOS or TechWiz, this depolarization effect is completely neglected, and the calculated CR is solely determined by the polarizers without considering the depolarization or scattering effect. Therefore, it is quite common to obtain CR > 10,000:1 in simulations, but in reality it is much lower. If the CR is not accurate, let alone the viewing angle. Therefore, there is urgent need to build a more rigorous model taking the

depolarization effect into consideration, which helps not only understand the underlying physical mechanisms but also guide the device and material optimizations.

In this part, we build a physical model by introducing a depolarization coefficient (A). With that, we could accurately simulate the contrast ratio and viewing angle [114]. Then, based on this model, we propose a new device structure to mitigate the depolarization effect, leading to a much improved CR. Other possible approaches to enlarge CR will also be discussed.

4.1.1 New simulation model

(a) Polarizer effect

Before introducing the new simulation model, firstly we have to know how the conventional model works. Here, we choose a commercial software TechWiz (Sanayi, Korea) as an example. In our simulation, the parameters for polarizer and analyzer are: n_o = 1.5, k_o = 0.000306, n_e = 1.5, and k_e = 0.019027. As usual, n_o (k_o) and n_e (k_e) represent the real (imaginary) part of ordinary and extraordinary refractive index, respectively. Then, polarizer (analyzer) thickness is varied from 15 μm to 30 μm, and the obtained results are shown in Figure 4.1. As expected, when the thickness of polarizer (or analyzer) increases, the transmittance of both bright state and dark state decreases, but at different rates [Figure 4.1(a)]. As a result, the corresponding CR increases exponentially [Figure 4.1(b)], and CR > 100,000:1 can be realized by simply increasing the polarizer thickness to over 29 μm. However, this is only for the ideal case. In reality, due to the depolarization effect of LCD components, the CR is limited to ~5000:1 for VA mode and ~2000:1 for FFS mode.

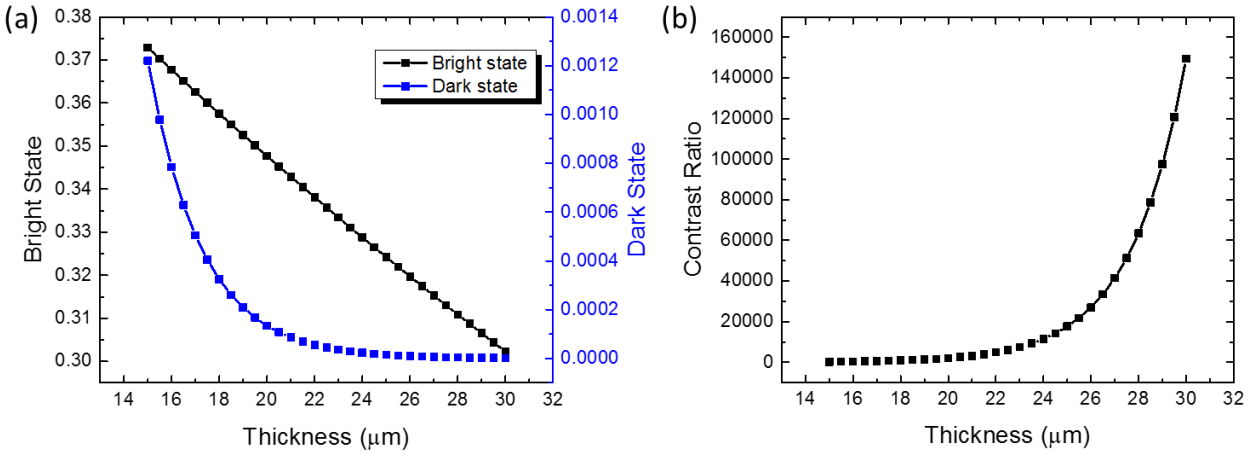

Figure 4.1. (a) Simulated transmittance of bright state and dark state, and (b) simulated CR as a function of polarizer thickness. No depolarization effect is considered.

(b) Origins of depolarization

The origins for depolarization are rather complicated; they may come from the diffraction effect of patterned thin-film transistors (TFTs) and electrode, scattering effect from LC layer and color filter (CF) array, misalignment of crossed polarizers, and rubbing scratches, etc. [106-112] Figure 4.2 schematically depicts some of them. Moreover, these physical origins make different contributions for different LC modes. For example, in FFS and in-plane switching (IPS) modes, scattering effect from LC director's thermal fluctuation contributes 50%-60% to the total depolarization effect (also known as degree of imperfection), while CF pigment scattering makes 30%-40% [111, 112]. But in VA mode, LC scattering is greatly reduced, thus CF scattering turns out to be the dominant factor [115].

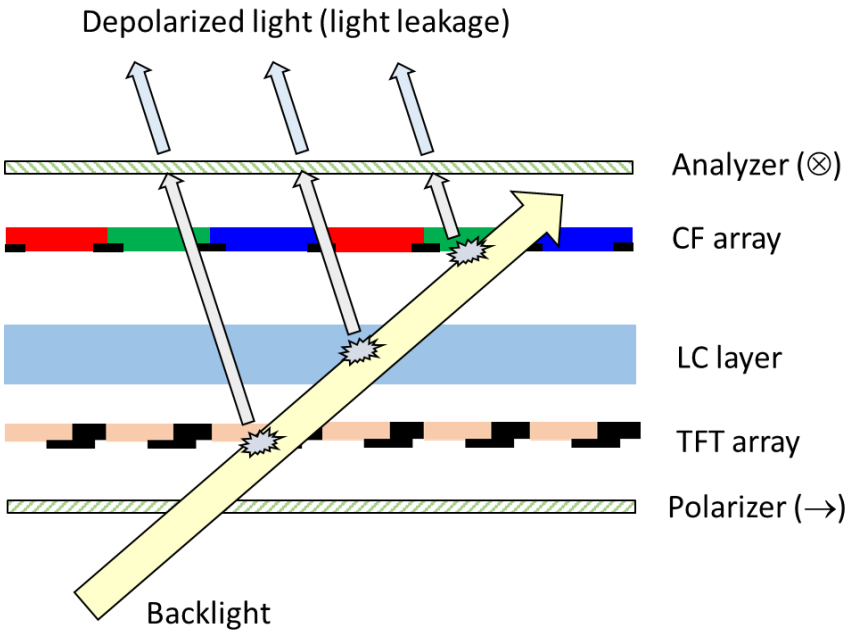

Figure 4.2. Schematic diagram for accounting the depolarization effect in an LCD panel. CF: color filter; LC: liquid crystal; TFT: thin-film transistor.

(c) Depolarization coefficient (A)

Next, to quantify the depolarization effect we introduce a depolarization coefficient (A), which is described by:

$$I_x^{'} = I_x \cdot (1-A) + I_y \cdot A, \tag{4.1}$$

$$I_y^{'} = I_x \cdot A + I_y \cdot (1-A), \tag{4.2}$$

where I_x (I_y) and I_x' (I_y') represent the intensity of original light and scattered light along two orthogonal polarization directions, respectively. In theory, each depolarization mechanism should have one coefficient, like A_1 for electrode diffraction, A_2 for LC scattering, A_3 for CF scattering, etc. But for simplicity we can define an *effective* depolarization coefficient (A_{eff}), which is the sum of each individual coefficient:

$$A_{eff} = A_1 + A_2 + A_3 + \cdots. \tag{4.3}$$

This could be illustrated as follows. Let us start from the simplest case: A_1 and A_2. They are governed by these equations:

$$\begin{aligned} I'_{1x} &= I_{1x} \cdot (1 - A_1) + I_{1y} \cdot A_1 \\ I'_{1y} &= I_{1x} \cdot A_1 + I_{1y} \cdot (1 - A_1) \\ I'_{2x} &= I'_{1x} \cdot (1 - A_2) + I'_{1y} \cdot A_2 \\ I'_{2y} &= I'_{1x} \cdot A_2 + I'_{1y} \cdot (1 - A_2) \end{aligned} \tag{4.4}$$

With simple algebra, we obtain:

$$\begin{aligned} I'_{2x} &= I_{1x} \cdot [1 - (A_1 + A_2) + 2A_1A_2] + I_{1y} \cdot [(A_1 + A_2) - 2A_1A_2], \\ I'_{2y} &= I_{1x} \cdot [(A_1 + A_2) - 2A_1A_2] + I_{1y} \cdot [1 - (A_1 + A_2) + 2A_1A_2]. \end{aligned} \tag{4.5}$$

In practice, A_1 and A_2 are relatively small and we can neglect the higher order term $2A_1A_2$. Under such condition, Eq. (4.5) is simplified to:

$$\begin{aligned} I'_{2x} &\approx I_{1x} \cdot (1 - A_{eff}) + I_{1y} \cdot A_{eff}, \\ I'_{2y} &\approx I_{1x} \cdot A_{eff} + I_{1y} \cdot (1 - A_{eff}). \end{aligned} \tag{4.6}$$

In Eq. (4.6), $A_{eff} = A_1 + A_2$. Similarly, although multiple depolarization factors could coexist in an LCD panel, we could treat them as a single coefficient A in the simulation.

4.1.2 Simulated contrast ratio

With the introduction of depolarization coefficient A, now we can perform the calculations. Figure 4.3 depicts the flow chart of our new simulation model [114]. Compared to the conventional one, the only difference is the introduction of a scattering module. Next, to illustrate the effectiveness of our new model, we choose MVA and FFS as two examples.

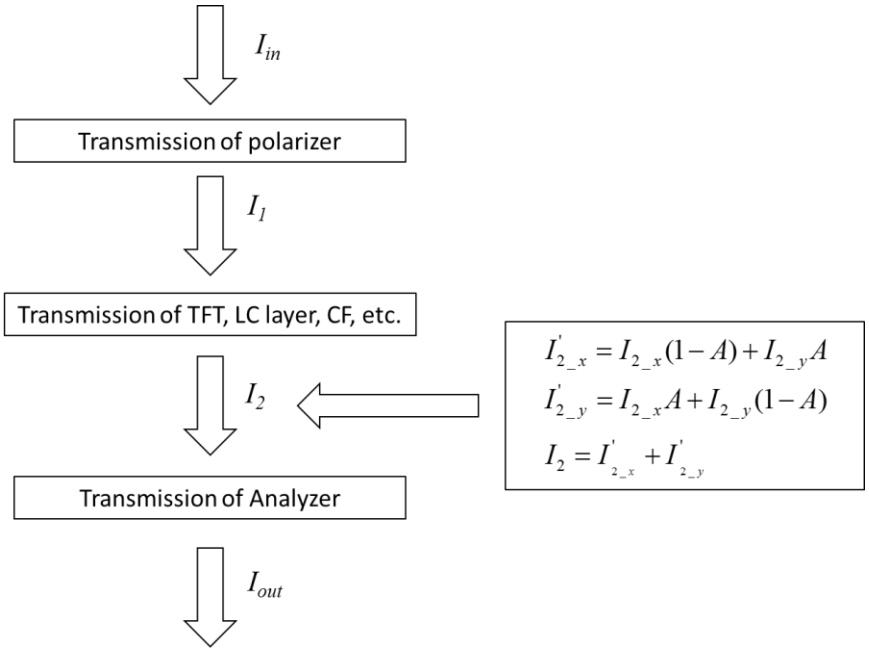

Figure 4.3. Flow chart of the proposed simulation model.

(a) MVA mode

Due to the fast response time and high contrast ratio, MVA has been widely used in large-sized TVs [4]. Here, we choose it as an example to elucidate the simulation procedures. The employed LC mixture and electrode structure are the same as those reported in [116]: MLC-6608 (Merck), electrode width w = 6 μm, electrode gap g = 42 μm, and cell gap d = 4 μm. Compensation films are implemented to suppress the color shift and gamma shift at large oblique angles. Polarizer and analyzer are 24-μm thick with n_o = 1.5, k_o = 0.000306, n_e = 1.5, and k_e = 0.019027. Unless otherwise stated, all the contrast ratios presented here are evaluated at λ = 550 nm.

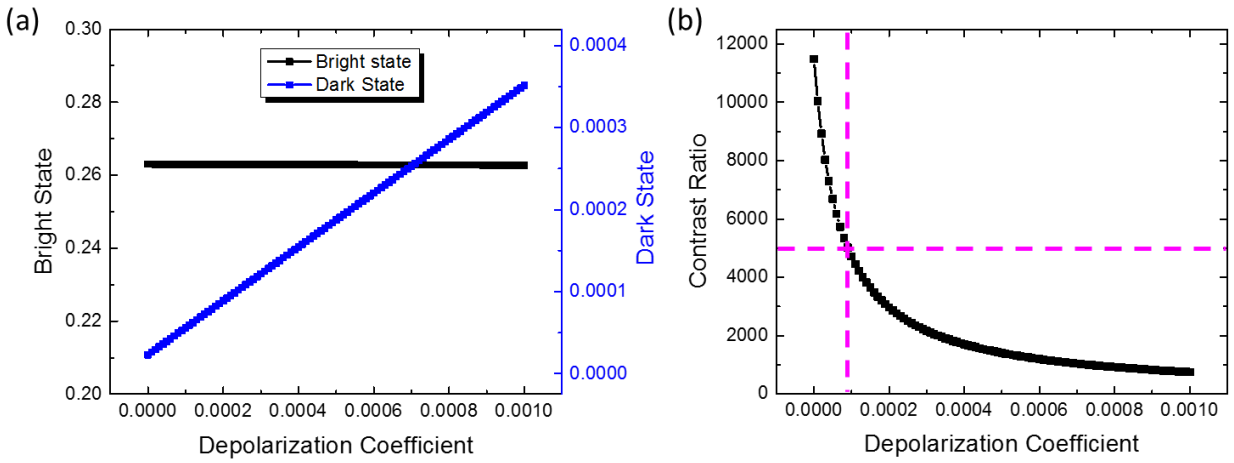

Figure 4.4. (a) Simulated transmittance of bright state and dark state, and (b) simulated CR as a function of depolarization coefficient for MVA mode. Depolarization effect is considered.

With all other parameters being known, the depolarization coefficient *A* can be extracted easily from the measured contrast ratio. Figure 4.4(a) shows the transmittance of bright state and dark state as a function of *A*, where bright state is not affected but dark state is degraded significantly as *A* increases. Figure 4.4(b) shows the corresponding CR. When $A = 0$ (ideal case without depolarization effect), CR is ~12,000:1. As *A* increases (real case with strong depolarization effect), CR decreases almost exponentially. According to the measured result, MVA shows CR ≈ 5000:1. Thus, from Figure 4.4(b) we find $A \sim 0.00009$ for the MVA mode.

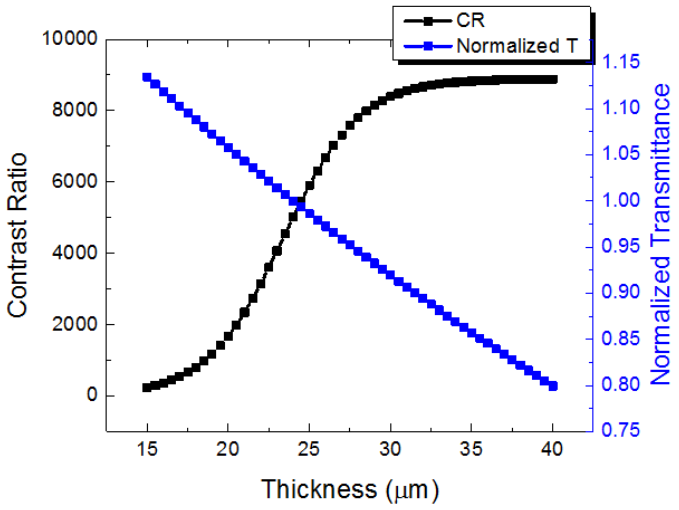

Figure 4.5. Simulated contrast ratio and normalized transmittance for MVA mode with depolarization coefficient A = 0.00009. Note: 24-μm thick polarizer is the reference with CR ≈ 5000:1 and efficiency = 1.

With the obtained coefficient A, we can evaluate the real CR for the MVA mode by varying the polarizer thickness. Results are depicted in Figure 4.5. Interestingly, as the polarizer gets thicker, CR increases first but then saturates gradually. This trend is quite different from the result using conventional model [Figure 4.1(b)]. It indicates that keeps on increasing the polarizer thickness would eventually reach a theoretical limit (CR_{lim}), which is governed by the depolarization coefficient (A) and peak transmittance (T_p):

$$CR_{\text{lim}} = T_p / A. \tag{4.7}$$

Based on our new model, we could also perform the optimization for polarizer. For example, in Figure 4.5, let us set 24-μm thick polarizer as the reference with CR ≈ 5000:1 and efficiency = 1. As the polarizer thickness increases, CR increases and then saturates but transmittance keeps decreasing. A good balance occurs at 29 μm, where CR is increased by 60%

(≈ 8000:1) while the transmittance is reduced by 6.8% (93.2%). For comparison, it is unlikely to do the similar optimization with conventional models because the true CR information is obscured.

(b) FFS mode

FFS mode exhibits several outstanding features, such as high transmittance, wide viewing angle, weak color shift, and robust to touch pressure [4, 10]. Both positive (p-FFS) and negative (n-FFS) dielectric anisotropy ($\Delta\varepsilon$) LC materials can be used in FFS [28, 29]. Here, we focus on n-FFS with zigzag electrode configuration. The employed LC mixture is ZOC-7003 (JNC, Japan), cell gap is 3.11 μm, electrode width is 2.5 μm, and electrode gap is 3.5 μm. The simulated results are plotted in Figure 4.6. Due to stronger scattering effect of the LC layer, FFS exhibits a slightly lower CR (≈ 2000:1). The corresponding *A* for FFS is 0.00039, which is about 4x larger than that of MVA (*A*≈ 0.00009).

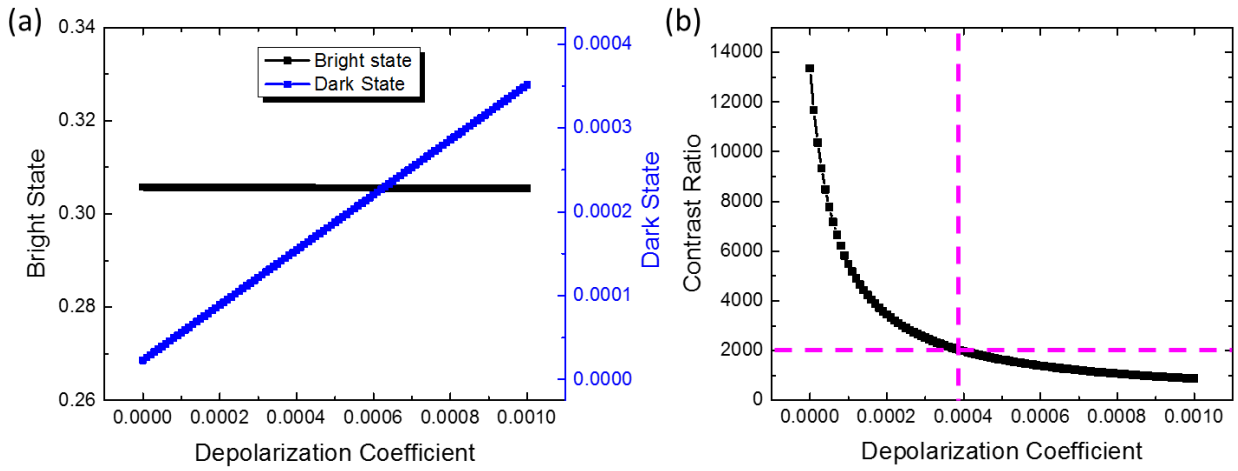

Figure 4.6. (a) Simulated transmittance of bright state and dark state, and (b) simulated CR as a function of depolarization coefficient for FFS mode, where depolarization effect is considered.

Figure 4.7 shows how the polarizer thickness affects the CR and optical efficiency of FFS mode. A similar trend, where CR saturates at 2400:1, is observed. However as the polarizer

thickness increases from 24 μm to 29 μm, the CR only improves by 15% (from 2000:1 to 2300:1), which is much less significant than that of MVA mode (15% vs. 60%).

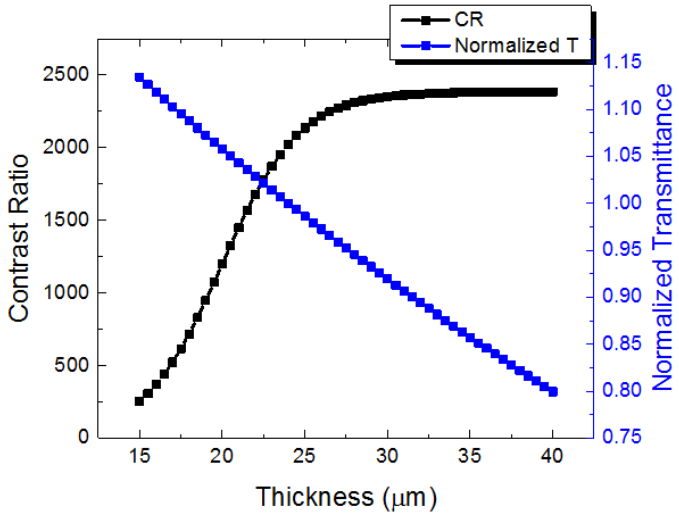

Figure 4.7. Simulated contrast ratio and normalized transmittance for FFS mode with depolarization coefficient A = 0.00039. Note: 24-μm thick polarizer is the reference for CR ≈ 2000:1 and efficiency = 1.

(c) CR improvement

As discussed above, FFS shows less CR improvement when increasing the polarizer thickness. This can be further investigated by varying the depolarization coefficient, and results are plotted in Figure 4.8. As A increases, the CR improvement ($CR_{T=29\mu m}/CR_{T=24\mu m}$) gradually saturates. This trend is quite reasonable because CR is jointly determined by the polarizer and the depolarization effect. If depolarization is weaker (smaller A), then the polarizer would make a larger impact, just like MVA mode. On the other hand, if depolarization is strong (large A), then the CR would not be affected too much by the polarizer. Thus, to improve CR of an FFS LCD, the most effective approach is to reduce A rather than increasing the polarizer's thickness. To do so,

several methods can be considered, such as optimizing LC alignment [109], choosing a proper LC mixture [103], and reducing the CF pigment size [102].

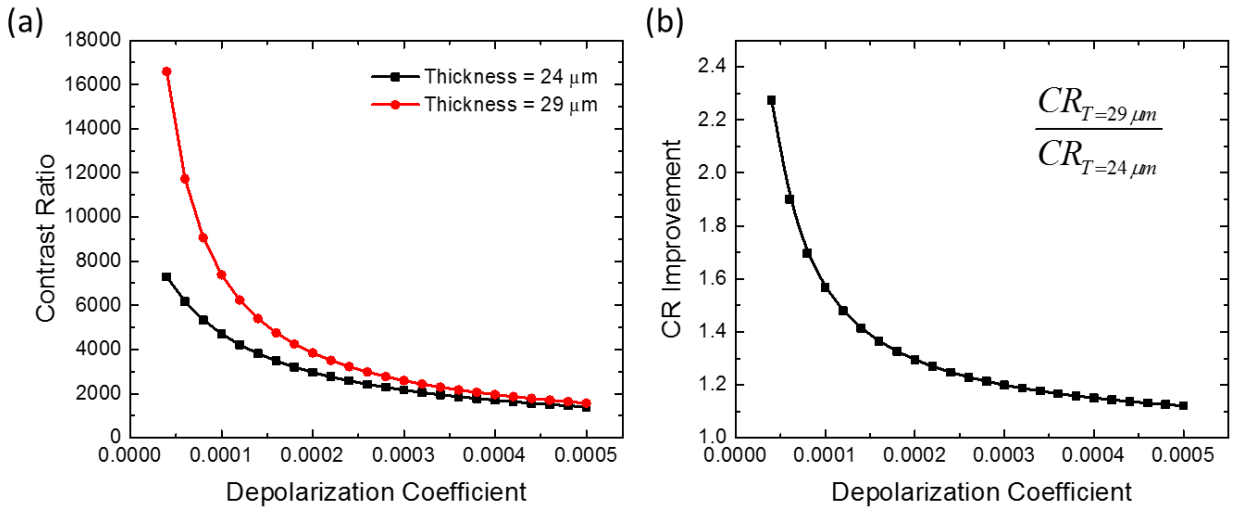

Figure 4.8. (a) Simulated contrast ratio and (b) contrast ratio improvement as a function of depolarization coefficient.

4.1.3 Simulated viewing angle

So far, we only concentrate on the CR at normal angle. Next, we examine the CR at different viewing angles. Please note that, here for simplicity, we assume the depolarization coefficient is constant for the entire viewing zone. In practice, we have to extract these coefficients at each viewing angle, using the method illustrated in Figure 4.4(b) and Figure 4.6(b). However, as will be discussed later, at large oblique angles, CR is much lower. In that case, depolarization coefficient will not make too much impact.

(a) MVA mode

Figure 4.9 shows the simulated isocontrast contours for the MVA mode. Without considering the scattering or depolarization effect [Figure 4.9(a)], the maximum CR obtained by

TechWiz is 11,437:1. But when A (≈ 0.00009) is introduced using our new model [Figure 4.9(b)], this value is reduced to CR_{max} = 5011:1. Clearly, our result is more realistic and representative for practical products. Also, by comparing these two figures we can find a very interesting phenomenon: the high CR region (> 4000:1) shrinks noticeably, while the low CR region (< 500:1) remains almost the same. This finding is consistent with our previous result shown in Figure 4.8, which indicates higher CR is more sensitive to the depolarization effect.

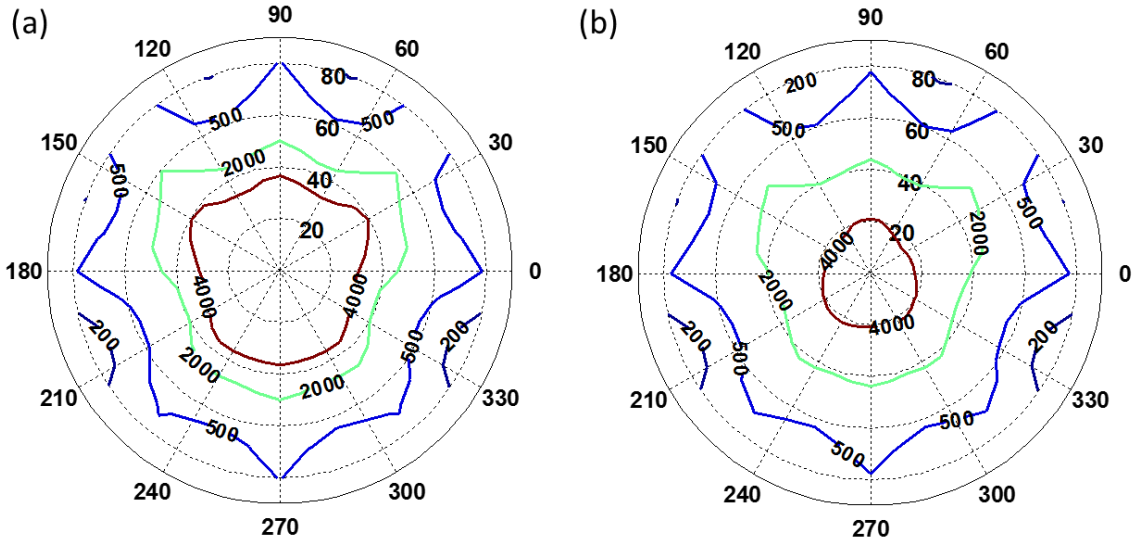

Figure 4.9. Simulated isocontrast contour for (a) ideal MVA mode using TechWiz, where CR_{max} = 11,437:1, CR_{min} = 132:1, and CR_{ave} = 4350:1. (b) Real MVA with A≈ 0.00009, where CR_{max} = 5011:1, CR_{min} = 130:1, and CR_{ave} = 2392:1. For both cases, the polarizer thickness is 24 μm.

Now the maximum CR is about 5000:1. To enlarge this value, we could increase the polarizer thickness from 24 μm to 29 μm, as described above. The obtained CR_{max} is 8000:1, and meanwhile the viewing angle is widened, especially in the central part [Figure 4.10(a)]. If we can further reduce the depolarization coefficient by 20% (from 0.00009 to 0.000071 using the methods mentioned above), then the maximum CR would increase to 10,066:1 [Figure 4.10(b)].

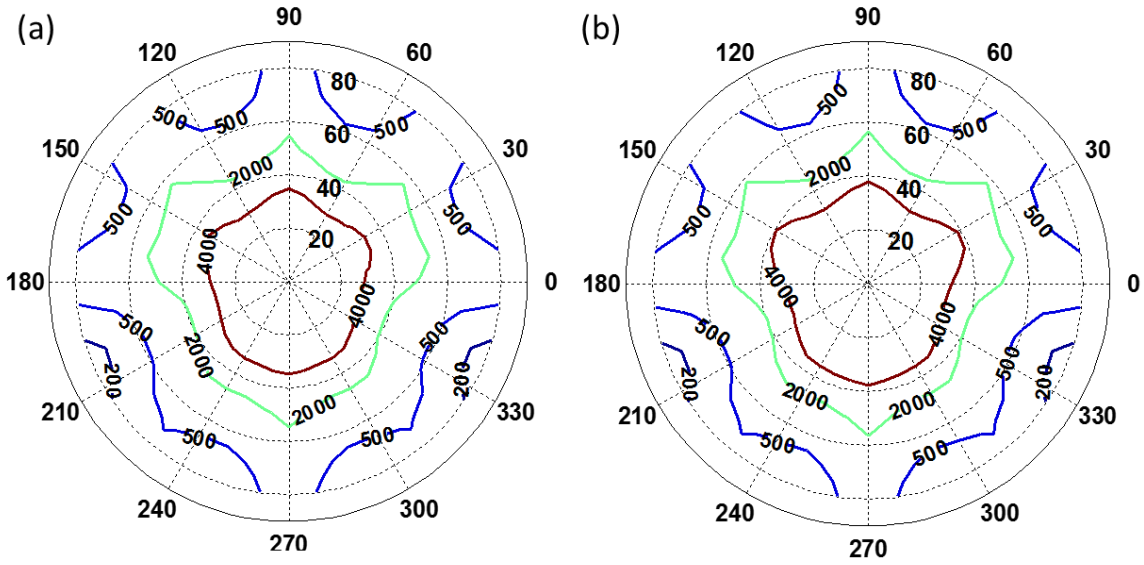

Figure 4.10. Simulated isocontrast contour for (a) a realistic MVA with polarizer thickness = 29 μm and A = 0.00009, where CR_{max} = 8129:1, CR_{min} = 147:1, and CR_{ave} = 3501:1. (b) Same MVA but with polarizer thickness = 29 μm and A = 0.000071, where CR_{max} = 10,066:1, CR_{min} = 148:1, and CR_{ave} = 4077:1.

(b) FFS mode

Next, we examine the viewing angle property of FFS mode, and results are shown in Figure 4.11. A big difference is observed between conventional model (ideal case) and our new model with depolarization coefficient A = 0.00039. For example, in Figure 4.11(a), the maximum CR is as high as 13,150:1, and CR > 5000:1 covers a large region. But using our new model [Figure 4.11(b)], CR_{max} is only 2024:1, and the contrast ratio in the central viewing zone is reduced to 1500:1, which is more consistent to the measured results.

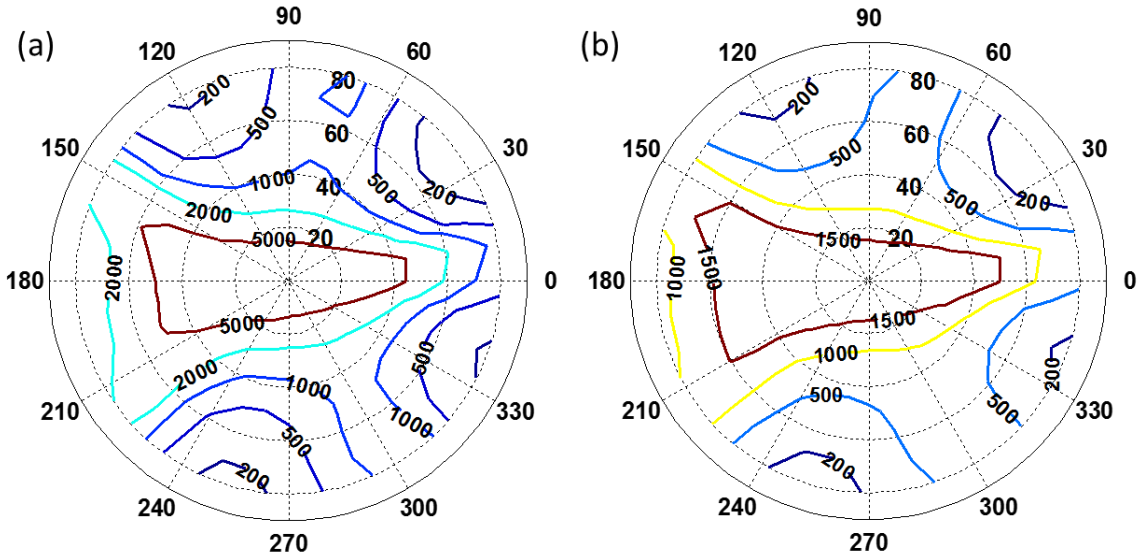

Figure 4.11. Simulated isocontrast contour for (a) an ideal FFS mode using TechWiz, where CR_{max} = 13,150:1, CR_{min} = 105:1, and CR_{ave} = 4467:1. (b) A realistic FFS with depolarization coefficient A = 0.00039, where CR_{max} = 2024:1, CR_{min} = 100:1, and CR_{ave} = 1184:1. For both cases, the polarizer thickness is 24 μm.

4.2 High CR LCD with an in-cell polarizer

4.2.1 Structure design

As aforementioned, depolarization (scattering) coefficient A plays a key role for improving the contrast ratio and viewing angle. To reduce A, here we propose a new device structure, as Figure 4.12 depicts, by adding an in-cell polarizer between the LC layer and the color filters [117]. The remaining structure remains the same as conventional LCD panel. Please note that the transmission axis of in-cell polarizer is parallel to that of analyzer. Because of the introduction of in-cell polarizer, the depolarization coefficients for each layer are decoupled. That is to say, below the in-cell polarizer, depolarization is mainly from TFT substrate and LC layer, which is marked as A_1; while above the in-cell polarizer, depolarization is mainly governed by the scattering effect

of color filter pigment, marked as A_2. Then A_1 and A_2 should be treated separately, as will be discussed later.

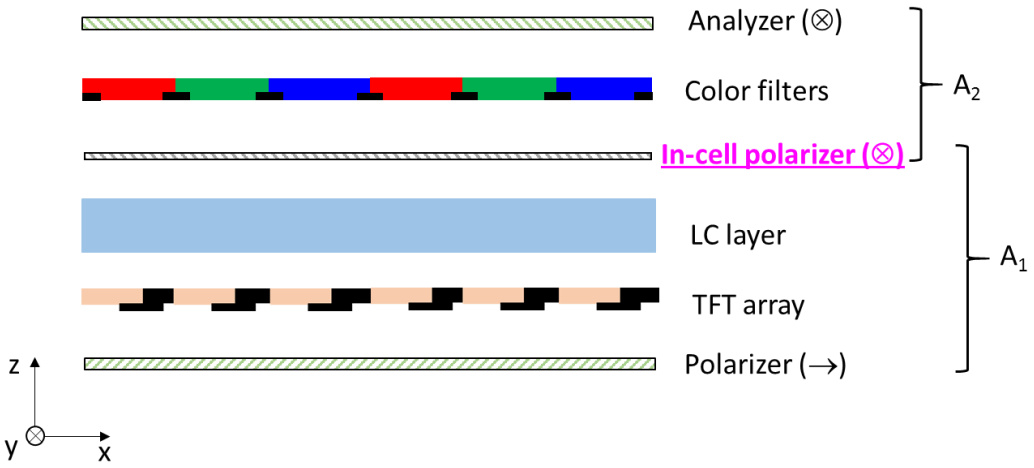

Figure 4.12. Schematic diagram of the proposed device structure with an in-cell polarizer.

4.2.2 Operation principles

Figure 4.13 shows the detailed working mechanism. For conventional one [Figure 4.13(a)], when backlight goes through the front polarizer, it becomes linearly polarized, say along x-axis. Then after passing through the TFT substrate and LC layer, there is some light leakage along y-axis due to scattering effect. Here, it is governed by A_1. After the light passing through color filters, the depolarization becomes more severe, represented by A_1+A_2. When entering the analyzer, the x-polarized (dominant polarization direction) light is blocked as expected, while only the depolarized light (jointly determined by A_1+A_2) could traverse through the analyzer. This undesirable light leakage degrades the contrast ratio [111, 112].

For our proposed device structure [Figure 4.13(b)], the depolarization effect remains the same for the TFT substrate and LC layer, which is A_1. But above the LC layer, there is an in-cell polarizer to absorb the x-polarized light; only the scatted light could leak through and enter the

color filter array (although it has strong scattering effect). In this case, the depolarized light is still governed by A_1, and it becomes the final light leakage. Therefore, the effective CR would be enhanced greatly.

Another important point should be mentioned here is that the extinction ratio of in-cell polarizer is not too critical. As long as most of the x-polarized light (dominant polarization direction) is absorbed by the in-cell polarizer, the whole system should work equally well. In that way, high transmittance would be realized. In fact, in our simulation as will be shown later, a 1-μm-thick lyotropic LC-based in-cell polarizer is employed. Its extinction ratio is only ~2000:1. Even if this in-cell polarizer has an extinction ratio as low as 100:1, according to our analysis, the final CR performance would not degrade too much, because only 1% of the leaked light would be scattered by the CF pigments. As a result, the final light leakage remains negligible for the MVA and FFS mode.

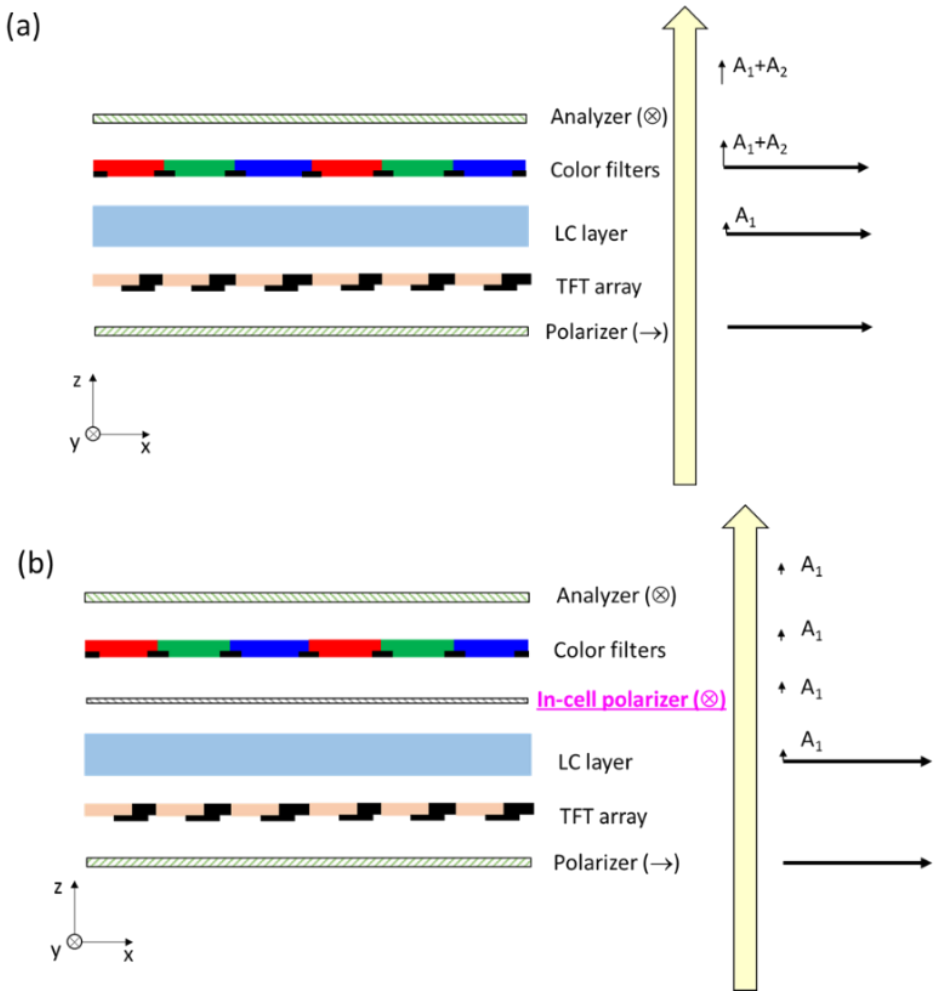

Figure 4.13. Working mechanism of (a) conventional LCD panel with depolarization effects, and (b) the proposed LCD panel with decoupled depolarization effects.

4.2.3 Simulation results

In our simulation, we assume the in-cell polarizer is 1-μm thick with n_o = 1.5, k_o = 0.0003, n_e = 1.5, and k_e = 0.364. Since the depolarization coefficients are decoupled intentionally, the calculation flow chart would be slightly different from previous one, as shown in Figure 4.14.

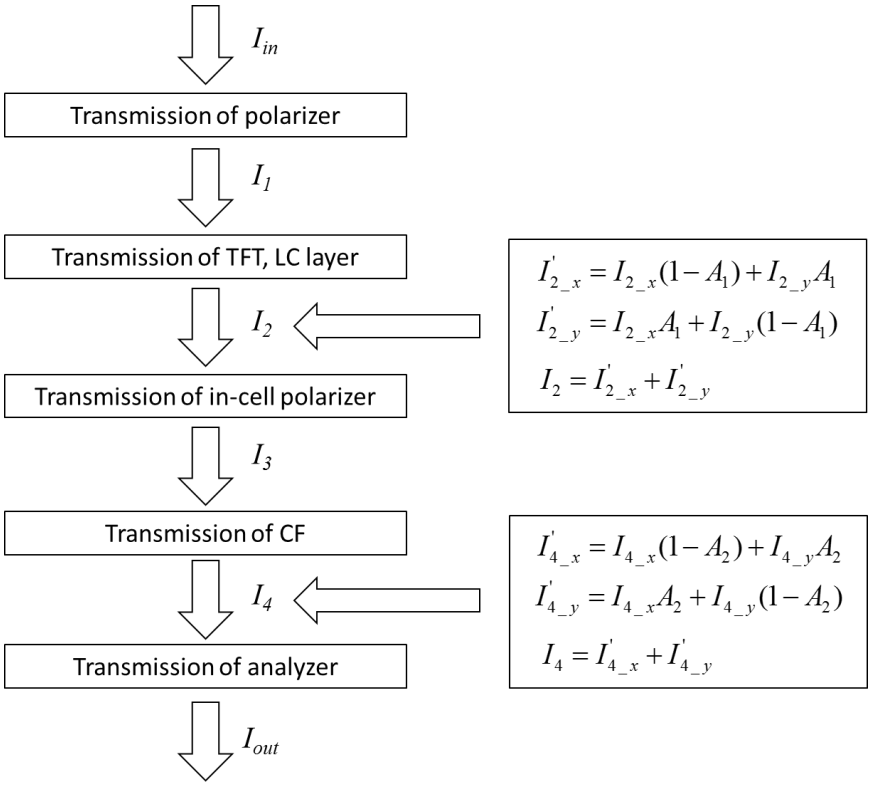

Figure 4.14. Flow chart of the proposed simulation model for new structure configuration.

(a) MVA mode

According to the analyses from both experiment [107] and simulation [115], LC scattering in MVA mode is more forgiven than that in FFS mode due to their different alignment directions (homeotropic vs. homogeneous). Therefore, in MVA calculations, we set A_1 = 0.00003 and A_2 = 0.00006 ($A_1 < A_2$); while in FFS mode it is reversed, i.e. $A_1 > A_2$, as will be discussed later. Figure 4.15 shows the simulated viewing angle of new MVA mode. For conventional 24 μm thick polarizer [Figure 4.15(a)], the maximum CR is improved to 12,277:1, which is about 2.4x higher than that of conventional one shown in Figure 4.9(b). Also, the high CR region is greatly widened, and the average CR for entire viewing zone is > 4,500:1. If we slightly increase the polarizer thickness to 29 μm [Figure 4.15(b)], the maximum CR is improved to 23,163:1. This is a record-

high CR for LCD. Please note that all these results are realized using our new model which includes the depolarization effect.

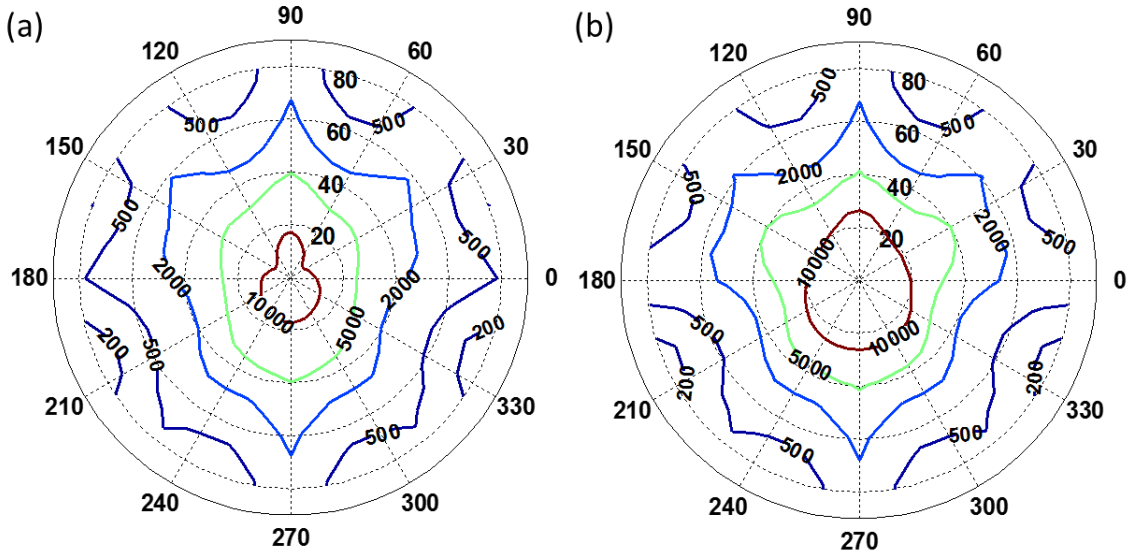

Figure 4.15. Simulated isocontrast contour for the proposed device configuration in MVA mode. (a) Polarizer thickness is 24 µm, and (b) Polarizer thickness is 29 µm. For the 24-µm thick polarizer: CR_{max} = 12,277:1, CR_{min} = 132:1, and CR_{ave} = 4685:1. For the 29-µm thick polarizer: CR_{max} = 23,163:1, CR_{min} = 149:1, and CR_{ave} = 7223:1.

(b) FFS mode

Figure 4.16 depicts the isocontrast contour of the new FFS mode with an in-cell polarizer. Here, we set A_1 = 0.00026 and A_2 = 0.00013, since the light leakage mainly originates from LC scattering [111, 112]. From Figure 4.16(a), the maximum CR is improved to 3000:1, which is higher than the theoretical limit of 2400:1 shown in Figure 4.7. Similarly, increasing the polarizer thickness to 29 µm [Figure 4.16(b)] would further boost the CR_{max} to 3349:1. And CR > 3000:1 is extended to ± 60° in the horizontal viewing direction.

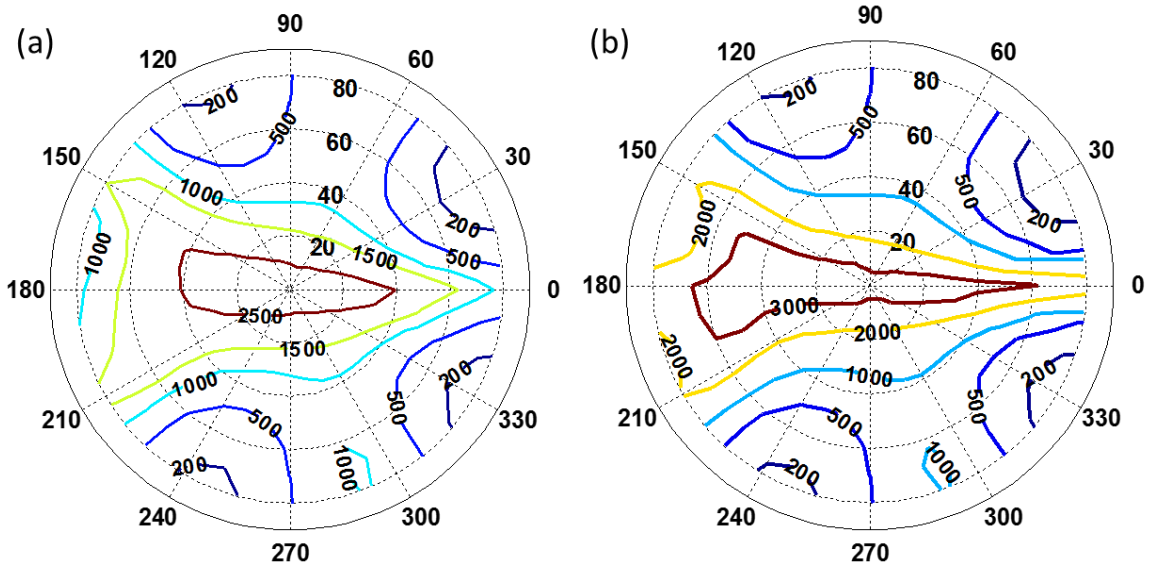

Figure 4.16. Simulated isocontrast contour for the new FFS with an in-cell polarizer. (a) Polarizer thickness is 24 μm, and (b) polarizer thickness is 29 μm. For the 24-μm thick polarizer: CR_{max} = 3002:1, CR_{min} = 115:1, and CR_{ave} = 1576:1. For the 29-μm thick polarizer: CR_{max} = 3349:1, CR_{min} = 115:1, and CR_{ave} = 1819:1.

4.2.4 Discussion

So far, high CR (> 10,000:1) has been realized by adding an in-cell polarizer between LC layer and color filter array to decouple the depolarization effect. Actually, based on the same concept, various device configurations can be considered.

(a) Dual in-cell polarizers

For practical applications, the in-cell polarizer can be placed in other places to decouple the depolarization coefficient of desired layers. Of course, we could also add more than one in-cell polarizer to the LCD panel to decouple each layer. For example, in Figure 4.17 we add two in-cell polarizers on both sides of the LC cell. Under such condition, the depolarization coefficient of TFT and LC layer is decoupled so that the CR can be further enhanced. Besides, if the in-cell polarizer

exhibits a high polarization ratio, then the crossed polarizer and analyzer can be removed. The device thickness would be much reduced. It could become a strong contender for flexible displays while keeping a high contrast ratio.

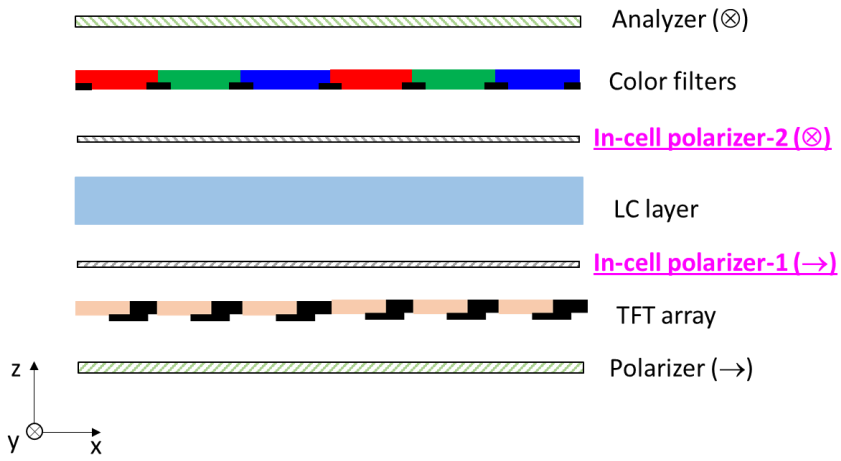

Figure 4.17. Schematic diagram of the proposed structure with dual in-cell polarizers. In this case, the polarizer and the analyzer could be removed.

(b) Reflective polarizer

Figure 4.18 shows another modification, where in-cell polarizer is replaced by a reflective polarizer, or wire-grid polarizer [118, 119]. In this configuration, the light after LC layer is reflected and recycled, thus higher optical efficiency could be achieved while keeping a high CR. Also, since the transmission axis of this reflective polarizer is parallel to that of analyzer, it will only reflect light from LC side (i.e. backlight side). For ambient light, there is no side effects.

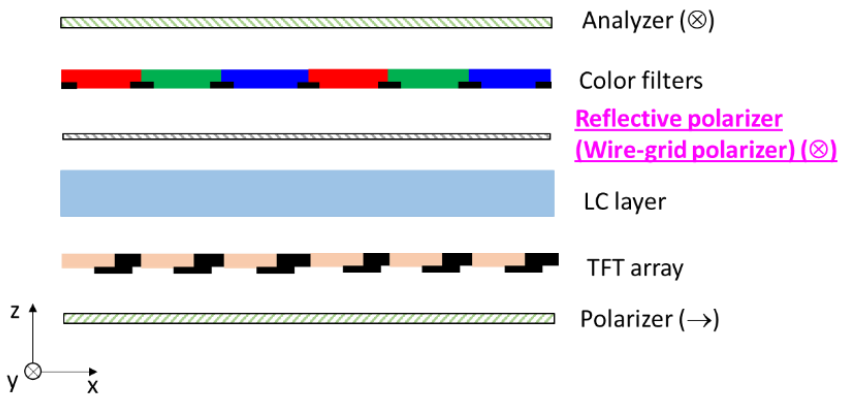

Figure 4.18. Schematic diagram of the proposed structure with a reflective polarizer or wire-grid polarizer.

(c) Field-sequential color display

In a field-sequential color (FSC) display, the color filter array is removed [59, 60, 120]. With a fast-switching LC, both red, green and blue (RGB) sub-frames are obtained in sequential time, as illustrated in Figure 4.19, so that both optical efficiency and resolution density are tripled. What's more, based on our analysis, the device contrast ratio could be improved significantly (compared to conventional LCD), because the depolarization effect of color filters is eliminated completely.

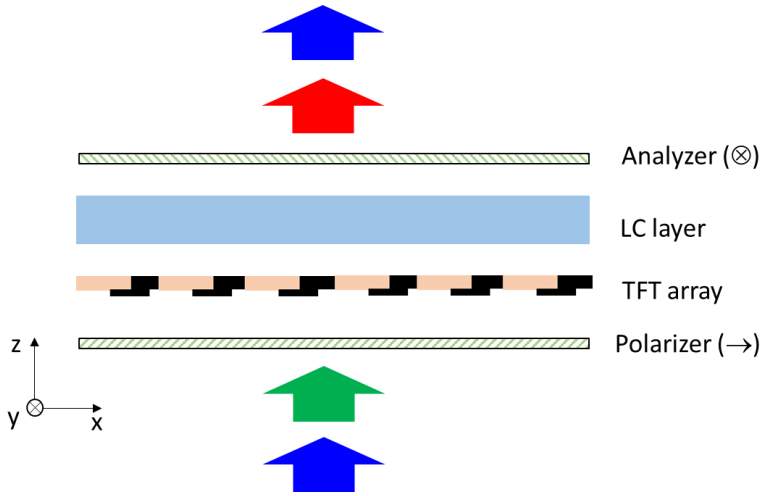

Figure 4.19. Schematic diagram of the field-sequential color display.

4.3 Dual-panel LCD system

4.3.1 High dynamic range

HDR is an emerging technology that can significantly improve the picture quality. So far, multiple HDR formats have been proposed, like HDR10, Dolby Vision, etc. [121-123]. In general, HDR requires a higher contrast ratio (CR ≥ 100,000:1), deeper dark state, higher peak brightness, richer gray scale (≥ 10 bits), and more vivid color.

Both LCD and OLED are HDR-compatible. Currently, the best HDR LCDs can produce brighter highlights than OLED, but OLED has a better overall contrast ratio thanks to its superior black level. To enhance an LCD's CR, local dimming backlight is commonly used [124-127]. By tailoring the brightness of segmented backlight, the dynamic CR could be boosted to 1,000,000:1. But as the name indicates, local dimming can only be modulated locally, and its dimming accuracy is limited by the number of LED segmentations.

To improve that, recently, a dual-panel LCD system has been proposed and explored [128, 129]. Its dimming accuracy could reach pixel-level, just like an OLED. Next, we will briefly discuss its advantages and the potential concerns.

4.3.2 Advantages and disadvantages

Just as the name indicates, a dual-panel LCD system consists of two LCD panels stacking together. Let us assume the contrast ratio of the two LCD panels is CR_1 and CR_2, respectively. Thus, for the cascaded display system, the effective contrast ratio should be $CR_1 * CR_2$ [128, 129]. So the first advantage of such an LCD system is high contrast. In experiment, CR > 1,000,000:1 has been demonstrated.

Another advantage is higher bit depth. By combining two 8-bit LCD panels, 14-bit signal depth modulation could be realized. While for conventional LCD, 14-bit driving is a great challenge for current TFT capability. Here, we simply use two LCD panels with $V_{on} \sim 5$ V to get 14-bit signal depth. The power consumption and design complexity are dramatically reduced. Also, the viewing angle of this dual-panel LCD system is widened, due to the much improved contrast ratio.

However, the tradeoff is also obvious. For example, the optical efficiency would be sacrificed significantly due to multiple reflections and aperture ratio reduction [129]. To improve that, the second LCD panel (close to backlight) could have lower pixel density than the master LCD panel. It has two advantages: 1) higher efficiency due to increased aperture ratio; and 2) easier for dual panel alignment.

Another potential issue is increased thickness and weight. However, this is not so critical, especially for TVs and desktop computers. They are mostly positioned in one place, and no need to be portable. As a result, the device thickness or weight is much more forgiven.

For dual panel system, cost would inevitably increase. The good news is with extensive material research and development, device innovation, and heavy investment on advanced manufacturing technologies, TFT LCD has gradually matured in all aspects. The panel cost is pretty low, especially compared to other display technologies, like OLED.

The other issue is Moiré effect, which is induced by patterned TFT backplanes. To improve that, a strong diffuser is needed. Recently, a polarization dependent scattering film (PDSF) was proposed and demonstrated. It could mitigate Moiré effect while maintaining high CR [129].

4.4 Summary

In this chapter, we have analyzed the depolarization effect in an LCD panel. It limits the final contrast ratio of LCD. Then we build a new model with the consideration of this depolarization effect. It could accurately simulate CR and viewing angle of an LCD. Based on that, we propose a novel LCD configuration by adding an in-cell polarizer between LC layer and CF array. The depolarization is decoupled, leading to much suppressed light leakage. Thus CR for a VA LCD is improved to > 20,000:1, and CR for an FFS LCD is improved to > 3000:1.

To further enlarge CR to fulfill the HDR requirement (CR ≥ 100,000:1), we propose and investigate a dual-panel LCD system. In experiment, exceedingly high contrast ratio (> 1,000,000:1) and high bit-depth (> 14 bits) were realized at merely 5 volts. Also, the potential concerns including efficiency, cost, thickness, and Moiré effect are discussed.

CHAPTER FIVE: CONCLUSION

Displays have multiple metrics to evaluate the performance. In this dissertation, we mainly focus on three of them: fast response time, wide color gamut, and high contrast ratio. These three are the key parameters affecting the final perceived image quality.

For response time, the annoying image motion blur issue would arise if LCD is not fast enough. To quantify this effect, motion picture response time (MPRT) was proposed and mostly practiced. By analysis, a "2 ms-rule" is found, that is, 1) if LC response time is 2 ms or less, its MPRT is comparable to that of an OLED, although OLED's response is 100x faster; 2) if MPRT is 2 ms or less, the image motion blur is unnoticeable.

To get 2 ms response, firstly, we developed an ultra-low viscosity LC mixture with negative dielectric anisotropy. The average GTG response time in a VA test cell is only 1.29 ms, and the corresponding MPRT is 6.88 ms at 120 fps. In comparison, OLED's MPRT is 6.66 ms. Their performance is indeed comparable. Next, with the help of duty ratio modulation, LCD's MPRT is reduced to 2 ms. The image blur is suppressed to unnoticeable level.

New LC mixture is the most straightforward approach, but in some grayscale transitions, the response time is still > 2x slower than the requirement. To further improve that, we propose a novel single-rubbing VA-FIS mode. It can achieve sub-millisecond response time in all gray scale transitions, with commonly used overdrive and undershoot driving. This is highly desirable to reduce the image motion blur and even work for field sequential color (FSC) displays. However, the degraded dark state and much reduced threshold voltage may be two potential concerns. To solve that, we propose to add a small biased voltage to the bottom common electrode. Good performance is obtained.

PS-BPLC is another option to get fast response time. But high operation voltage is the main hurdle for practical applications. Here, a new diamond-shape protruded IPS structure is proposed, the operation voltage could be reduced to 15V with ~75% transmittance. Moreover, all these are achieved with an industrially proven blue phase material, which shows high voltage holding ratio and good long-term stability. However, multiple (3-4) TFTs and 2 capacitors per pixel are still required in order to overcome the slow charging issue due to the large capacitance of employed BPLC.

As for color gamut, in the past two decades, its evaluation metric has gradually advanced from sRGB to NTSC, DCI-P3, and now to Rec. 2020 standard, whose coverage area in color space is nearly twice wider than that of sRGB. At the same time, multiple light sources have been developed to fulfill these ever-growing demands for vivid colors. Now the FWHM has been pushed to 20 nm. It becomes more and more difficult to make the bandwidth further narrower.

To relieve this burden, we propose two novel backlight configurations. One is a simple yet efficient approach using a so-called functional reflective polarizer (FRP). It acts as a notch filter to block the unwanted light, thus increasing the color purity. In simulation, a commercial 2pc-WLED is employed, and the color gamut is improved from 96.7% to 108.6% NTSC in CIE 1931, or from 112.9% to 133.9% NTSC in CIE 1976, which is comparable to the cadmium-based quantum dot backlight. Our design offers an alternative approach to quantum dots, while keeping low cost, long lifetime, and high brightness.

Another approach is to use a FRP and a patterned half-wave plate. This design decouples the polarization of blue light and green/red lights, which effectively suppresses the color crosstalk, thus, boosting the color gamut. In experiment, we prepared a white-light source using blue LED to pump green perovskite and red quantum dot, and demonstrated an exceedingly high color gamut

(95.8% Rec. 2020 in CIE 1931 color space, and 97.3% Rec. 2020 in CIE 1976 color space) with commercial high-efficiency color filters. These results are beyond the color gamut limit that a conventional LCD can achieve.

For contrast ratio, a non-emissive type LCD has its inherent constrains, i.e., the CR of a commercial VA LCD TV is only ~ 5000:1, let along other LCD modes. According to analysis, the limiting factor is the so-called depolarization effect inside each LCD panel. However, due to the complexity, most LCD simulation software neglects this effect, thus, the obtained CR or viewing angle property is incorrect.

Here, we built a more rigorous model by considering the depolarization effect of some key components in an LCD system. It is found that there is an inherent theoretical limit of CR, due to the depolarization effect in TFT substrate, LC layer, CF array, etc. Also, we propose a new device structure, where an additional in-cell polarizer is placed between LC layer and CF array to decouple the depolarization effect. The maximum CR of a MVA LCD could reach over 20,000:1, while the n-FFS mode could reach > 3000:1.

To further enlarge CR to fulfill the HDR requirement (CR ≥ 100,000:1), we propose and investigate a dual-panel LCD system. The device performance is quite promising, including high contrast ratio (> 1,000,000:1), high bit depth (> 14 bits), and pixel-level local dimming.

In summary, we have investigated three key display metrics: fast response time, wide color gamut, and high contrast ratio. They jointly determine the final perceived image quality. Fortunately, with great efforts in theoretical analysis and structure design, LCD has gained substantial improvement in all three aspects: unnoticeable image motion blur as CRT, vivid color as laser projector, and high contrast as OLED. It is seen that LCDs with supreme image qualities can be realized. Along with other outstanding features, like high peak brightness, high resolution

density, long lifetime, low cost, etc., LCD would continue to maintain its dominance in consumer electronics market for a long time.

APPENDIX: STUDENT PUBLICATIONS

JOURNAL PUBLICATIONS

1. H. Chen, R. Zhu, J. He, W. Duan, W. Hu, Y.Q. Lu, M. C. Li, S. L. Lee, Y. Dong, and S. T. Wu, "Going beyond the limit of an LCD's color gamut," Light: Science and Applications **6**, e17043 (2017).
2. (*Invited paper*) H. Chen, J. He, and S. T. Wu, "Recent advances on quantum-dot-enhanced liquid crystal displays," IEEE J. Selected Topics in Quantum Electronics **23**(5), 1900611 (2017).
3. H. Chen, G. Tan, M. C. Li, S. L. Lee, and S. T. Wu, "Depolarization effect in liquid crystal displays," Opt. Express **25**(10), 11315-11328 (2017).
4. F. Gou, F. Peng, Q. Ru, Y. H. Lee, H. Chen, Z. He, T. Zhan, K. L. Vodopyanov, and S. T. Wu, "Mid-wave infrared beam steering based on high-efficiency liquid crystal diffractive waveplates, " Opt. Express **25**(19), 22404-22410 (2017).
5. R. Zhu, H. Chen, and S. T. Wu, "Achieving 12-bit perceptual quantizer curve with liquid crystal display," Opt. Express **25**(10), 10939-10946 (2017).
6. J. He, H. Chen, J. Chen, Y. Wang, S. T. Wu, and Y. Dong, "Hybrid downconverters with green perovskite-polymer composite films for wide color gamut displays," Opt. Express **25**(11), 12915-12925 (2017).
7. F. Gou, H. Chen, M. C. Li, S. L. Lee, and S. T. Wu, "Submillisecond-response liquid crystal for high-resolution virtual reality displays," Opt. Express **25**(7), 7984-7997 (2017).
8. H. Chen, R. Zhu, M. C. Li, S. L. Lee, and S. T. Wu, "Pixel-by-pixel local dimming for high-dynamic-range liquid crystal displays," Opt. Express **25**(3), 1973-1984 (2017).

9. Y. Huang, H. Chen, G. Tan, H. Tobata, S-I Yamamoto, E. Okabe, Y. F. Lan, C. Y. Tsai, and S. T. Wu, "Optimized blue-phase liquid crystal for field-sequential-color displays," Opt. Mater. Express **7**(2), 641-650 (2017).

10. F. Peng, H. Chen, F. Gou, Y. H. Lee, M. Wand, M. C. Li, S. L. Lee, and S. T. Wu, "Analytical equation for the motion picture response time of display devices," J. Appl. Phys. **121**, 023108 (2017).

11. H. Chen, G. Tan, Y. Huang, Y. Weng, T. H. Choi, T. H. Yoon and S. T. Wu, "A low voltage liquid crystal phase grating with switchable diffraction angles," Sci. Rept. **7**, 39923 (2017).

12. H. Chen, F. Gou, and S. T. Wu, "A submillisecond-response nematic liquid crystal for augmented reality displays," Opt. Mater. Express **7**(1), 195-201 (2017).

13. H. Chen, R. Zhu, G. Tan, M.C. Li, S.-L. Lee, and S. T. Wu, "Enlarging the color gamut of liquid crystal displays with a functional reflective polarizer," Opt. Express **25**(1), 102-111 (2017).

14. H. Chen, Y.F. Lan, C. Y. Tsai, and S. T. Wu, "Low-voltage blue-phase liquid crystal display with diamond-shape electrodes," Liq. Cryst. **44**(7), 1124-1130 (2017).

15. H. Chen, F. Peng, F. Gou, Y. H. Lee, M. Wand, and S. T. Wu, "Nematic LCD with motion picture response time comparable to organic LEDs," Optica **3**(9), 1033-1034 (2016).

16. M. Hu, Z. An, J. Li, H. Chen, F. Peng, S. T. Wu, X. Wang and M. Li, "Low mid-infrared absorption tolane liquid crystals terminated by 2, 2-difluorovinyloxy: synthesis, characterization and properties," J. Mater. Chem. C. **4**(22), 4939-4945 (2016).

17. J. Li, W. Du, A. Gao, G. Bie, M. Hu, H. Chen, and S. T. Wu, "Enlarging the Kerr constant of polymer-stabilised blue phases with a novel chiral monomer," Liq. Cryst. **43**(7), 937-943 (2016).

18. F. Peng, F. Gou, H. Chen, Y. Huang, and S. T. Wu, "A submillisecond-response liquid crystal for color sequential projection displays," J. Soc. Inf. Disp. **24**(4), 241-245 (2016).

19. R. Zhu, H. Chen, T. Kosa, P. Coutino, G. Tan, and S. T. Wu, "High-ambient-contrast augmented reality with a tunable transmittance liquid crystal film and a functional reflective polarizer," J. Soc. Inf. Disp. **24**(4), 229-233 (2016).

20. H. Chen, Y. Weng, D. Xu, N.V. Tabiryan, and S. T. Wu, "Beam steering for virtual/augmented reality displays with a cycloidal diffractive waveplate," Opt. Express **24**(7), 7287-7298 (2016).

21. H. Chen, R. Zhu, Y. H. Lee, and S. T. Wu, "Correlated color temperature tunable white LED with a dynamic color filter," Opt. Express **24**(6), A731-A739 (2016).

22. H. Chen, R. Zhu, J. Zhu, and S. T. Wu, "A simple method to measure the twist elastic constant of a nematic liquid crystal," Liq. Cryst. **42**(12), 1738-1742 (2015).

23. H. Chen, F. Peng, M. Hu, and S. T. Wu, "Flexoelectric effect and human eye perception on the image flickering of a liquid crystal display," Liq. Cryst. **42**(12), 1730-1737 (2015).

24. R. Zhu, Z. Luo, H. Chen, Y. Dong, and S.T. Wu, "Realizing Rec. 2020 color gamut with quantum dot displays," Opt. Express **23**(18), 23680-23693 (2015).

25. H. Chen, Z. Luo, R. Zhu, Q. Hong, and S. T. Wu, "Tuning the correlated color temperature of white LED with a guest-host liquid crystal," Opt. Express **23**(10), 13060-13068 (2015).

26. F. Peng, Y. H. Lee, H. Chen, Z. Li, A. E. Bostwick, R. J. Twieg, and S. T. Wu, "Low absorption chlorinated liquid crystals for infrared applications," Opt. Mater. Express **5**(6), 1281-1288 (2015).

27. H. Chen, M. Hu, F. Peng, J. Li, Z. An, and S. T. Wu, "Ultra-low viscosity liquid crystals," Opt. Mater. Express **5**(3), 655-660 (2015).

28. H. Chen, Z. Luo, D. Xu, F. Peng, S.T. Wu, M.C. Li, S.L. Lee, and W.C. Tsai, "A fast-response A-film-enhanced fringe field switching liquid crystal display," Liq. Cryst. **42**(4), 537-542 (2015).

29. Z. Luo, H. Chen, Y. Liu, S. Xu, and S. T. Wu, "Color-tunable light emitting diodes based on quantum dot suspension," Appl. Opt. **54**(10), 2845-2850 (2015).

30. Z. Luo, F. Peng, H. Chen, M. Hu, J. Li, Z. An, and S. T. Wu, "Fast-response liquid crystals for high image quality wearable displays," Opt. Mater. Express **5**(3), 603-610 (2015).

31. D. Xu, H. Chen, S. T. Wu, M.C. Li, S. L. Lee, and W. C. Tsai, "A fringe field switching liquid crystal display with fast grayscale response time," J. Display Technol. **11**(4), 353-359 (2015).

32. F. Peng, D. Xu, H. Chen, and S. T. Wu, "A low voltage polymer network liquid crystal for infrared spatial light modulators," Opt. Express **23**(3), 2361-2368 (2015).

33. F. Peng, H. Chen, S. Tripathi, R. J. Twieg, and S. T. Wu, "Fast-response infrared phase modulator based on polymer network liquid crystal," Opt. Mater. Express **5**(2), 265-273 (2015).

34. D. Xu, F. Peng, H. Chen, J. Yuan, S. T. Wu, M. C. Li, S. L. Lee, and W. C. Tsai, "Image sticking in liquid crystal displays with lateral electric fields," J. Appl. Phys. **116**, 193102 (2014).

35. H. Chen, F. Peng, Z. Luo, D. Xu, S.T. Wu, M.C. Li, S. L. Lee, and W. C. Tsai, "High performance liquid crystal displays with a low dielectric constant material," Opt. Mater. Express **4**(11), 2262-2273 (2014).

36. F. Peng, Y. Chen, J. Yuan, H. Chen, and S.T. Wu, "Low temperature and high frequency effects of polymer-stabilized blue phase liquid crystals with a large dielectric anisotropy," J. Mater. Chem. C. **2**(18), 3597-3601 (2014).

37. X. Zhao, Z. Zheng, L. Liu, Q. Wang, H. Chen, and J. Liu, "Fast, long-scan-range pump-probe measurement based on asynchronous sampling using a dual-wavelength mode-locked fiber laser," Opt. Express **20**(23), 25584-25589 (2012).

CONFERENCE PROCEEDINGS

1. H. Chen, F. Gou, and S. T. Wu, "Submillisecond-response nematic LC for wearable displays," SID Symp. Dig. Tech. Pap. **48**(1), 377-380 (2017).
2. H. Chen, R. Zhu, M. C. Li, S. L. Lee, and S. T. Wu, "High dynamic range LCD with pixel-level local dimming," SID Symp. Dig. Tech. Pap. **48**(1), 890-893 (2017).
3. H. Chen, Y. F. Lan, C. Y. Tsai, and S. T. Wu, "Single-TFT-driving blue-phase LCD with diamond-shape electrodes," SID Symp. Dig. Tech. Pap. **48**(1), 1903-1906 (2017).
4. H. Chen, R. Zhu, G. Tan, M. C. Li, S. L. Lee, and S. T. Wu, "Wide-color-gamut LCD with a functional reflective polarizer," SID Symp. Dig. Tech. Pap. **48**(1), 1659-1662 (2017).
5. D. Wyatt, H. Chen, and S. T Wu, "Wide-color-gamut LCDs with Vivid Color LED technology," SID Symp. Dig. Tech. Pap. **48**(1), 992-995 (2017).
6. Y. H. Lee, H. Chen, R. Martinez, Y. Sun, S. Pang and S. T. Wu, "Multi-image plane display based on polymer-stabilized cholesteric texture," SID Symp. Dig. Tech. Pap. **48**(1), 760-762 (2017).

7. F. Peng, H. Chen, F. Gou, Y. H. Lee, M. Wand, M. C. Li, S. L. Lee, and S. T. Wu, "An LCD with submillisecond motion picture response time," SID Symp. Dig. Tech. Pap. **48**(1), 1826-1829 (2017).

8. J. He, H. Chen, H. Chen, Y. Wang, S T Wu, and Y. Dong, "Wide color gamut display based on ultrastable perovskite-polymer film and red QDs/phosphors," SID Symp. Dig. Tech. Pap. **48**(1), 349-352 (2017).

9. (*Invited talk*) H. Chen, F. Peng, F. Gou, M. Wand, and S. T. Wu, "Fast-response LCDs for virtual reality applications," Proc. SPIE **10125**, 101251E (2017).

10. J. He, H. Chen, H. Chen, Y. Wang, J. Chen, R. Zhu, S. T. Wu, and Y. Dong, "Wide color gamut LCDs with narrow green emitting films," Proc. SPIE **10125**, 101251D (2017).

11. (*Distinguished student paper*) H. Chen, F. Peng, M. Hu, and S. T. Wu, "Flexoelectric effect on image flickering of fringe field switching LCDs," SID Symp. Dig. Tech. Pap. **47**(1), 274-277 (2016).

12. H. Chen, R. Zhu, K. Käläntär, and S. T. Wu, "Quantum dot-enhanced LCDs with wide color gamut and broad angular luminance distribution," SID Symp. Dig. Tech. Pap. **47**(1), 1413-1416 (2016).

13. H. Chen, R. Zhu, Y. H. Lee, and S. T. Wu, "Correlated color temperature tunable WLED for smart lighting," SID Symp. Dig. Tech. Pap. **47**(1), 46-49 (2016).

14. (*Distinguished student paper*) F. Peng, H. Chen, F. Gou, Y. Huang, and S. T. Wu, "A submillisecond-response liquid crystal for color sequential projection displays," SID Symp. Dig. Tech. Pap. **47**(1), 179-182 (2016).

15. R. Zhu, Z. Luo, H. Chen, Y. Dong, and S. T. Wu, "Quantum dot LCDs for Rec. 2020," SID Symp. Dig. Tech. Pap. **47**(1), 765-767 (2016).

16. (*Distinguished student paper*) R. Zhu, H. Chen, G. Tan, T. Kosa, P. Coutino, and S. T. Wu, "A high-ambient-contrast augmented reality system," SID Symp. Dig. Tech. Pap. **47**(1), 1025-1028 (2016).

17. (*Distinguished student paper*) Z. Luo, F. Peng, H. Chen, M. Hu, J. Li, Z. An, and S. T. Wu, "High image quality wearable displays with a fast-response liquid crystal," SID Symp. Dig. Tech. Pap. **46**(1), 1-4 (2015).

18. H. Chen, F. Peng, S. T. Wu, M. Hu, J. Li, Z. An, M. C. Li, S. L. Lee, and W. C. Tsai, "Low dielectric constant materials for high performance LCDs," SID Symp. Dig. Tech. Pap. **46**(1), 450-453 (2015).

19. D. Xu, H. Chen, S. T. Wu, M. C. Li, S. L. Lee, and W. C. Tsai, "Fast-response fringe field switching LCD with patterned common electrode," SID Symp. Dig. Tech. Pap. **46**(1), 652-655 (2015).

20. (*Distinguished student paper*) H. Chen, Z. Luo, D. Xu, F. Peng, S. T. Wu, M. C. Li, S. L. Lee, and W. C. Tsai, "A fast-response A-film-enhanced fringe field switching LCD," SID Symp. Dig. Tech. Pap. **46**(1), 656-660 (2015).

21. (*Invited talk*) H. Chen, Y. Gao and S. T. Wu, "n-FFS vs. p-FFS: Who wins?" SID Symp. Dig. Tech. Pap. **46**(1), 735-738 (2015).

22. D. Xu, F. Peng, H. Chen, J. Yuan, S. T. Wu, M. C. Li, S. L. Lee, and W. C. Tsai, "Image sticking reduction of fringe field switching LCDs," SID Symp. Dig. Tech. Pap. **46**(1), 739-742 (2015).

23. F. Peng, D. Xu, H. Chen, and S. T. Wu, "A low-voltage and fast-response infrared spatial light modulator," SID Symp. Dig. Tech. Pap. **46**(1), 831- 834 (2015).

24. F. Peng, Y. Chen, J. Yuan, H. Chen, S. T. Wu, and Y. Haseba, "Low temperature and high frequency effects on blue phase liquid crystals," SID Symp. Dig. Tech. Pap. **45**(1), 164-167 (2014)

PATENTS

1. H. Chen, S. T. Wu, Y. F. Lan, C. Y. Tsai, "Liquid crystal display systems and related methods with pixel elements driven at different frequencies," US patent (2016, pending).
2. H. Chen, S. T. Wu, W. Duan, M. C. Li, S. L. Lee, "Display devices and related methods involving patterned phase retarding," US patent (2017, pending).

REFERENCES

[1] J. A. Castellano, ed. *Handbook of Display Technology*. Elsevier, 2012.

[2] M. Schadt, "Milestone in the history of field-effect liquid crystal displays and materials," Jpn. J. Appl. Phys. **48**(3S2), 03B001 (2009).

[3] Y. Ukai, "TFT-LCDs as the future leading role in FPD," SID Symp. Dig. Tech. Pap. **44**(1), 28-31 (2013).

[4] D. K. Yang and S. T. Wu . *Fundamentals of Liquid Crystal Devices.* John Wiley & Sons, 2014.

[5] 3M Optical Systems. *Vikuiti™ Brightness Enhancement Film (BEF) III*. 3M, 2010.

[6] 3M Optical Systems. *Vikuiti™ Dual Brightness Enhancement Film (DBEF)*. 3M, 2008.

[7] M. Schadt and W. Helfrich, "Voltage-dependent optical activity of a twisted nematic liquid crystal," Appl. Phys. Lett. **18**(4), 127-128 (1971).

[8] M. F. Schiekel and K. Fahrenschon, "Deformation of nematic liquid crystals with vertical orientation in electrical fields," Appl. Phys. Lett. **19**(10), 391-393 (1971).

[9] R. A. Soref, "Transverse field effects in nematic liquid crystals," Appl. Phys. Lett. **22**(4), 165-166 (1973).

[10] S. H. Lee, S. L. Lee, and H. Y. Kim, "Electro-optic characteristics and switching principle of a nematic liquid crystal cell controlled by fringe-field switching," Appl. Phys. Lett. **73**(20), 2881-2883 (1998).

[11] M. Schadt, H. Seiberle, and A. Schuster, "Optical patterning of multi-domain liquid-crystal displays with wide viewing angles," Nature **381**(6579), 212 (1996).

[12] H. Mori, Y. Itoh, Y. Nishiura, T. Nakamura, and Y. Shinagawa, "Performance of a novel optical compensation film based on negative birefringence of discotic compound for wide-viewing-angle twisted-nematic liquid-crystal displays," Jpn. J. Appl. Phys. **36**(1R),143 (1997).

[13] Y. Ito, J. Watanabe, Y. Saitoh, K. Takada, S. I. Morishima, Y. Takahashi, T. Oikawa, and T. Arai, "Innovation of optical films using polymerized discotic materials: past, present and future," SID Symp. Dig. Tech. Pap. **44**(1), 526-529 (2013).

[14] E. Yamamoto, H. Yui, S. Katsuta, Y. Asaoka, T. Maeda, Y. Tsuda, and K. Kondo, "Wide viewing LCDs using novel microstructure film," SID Symp. Dig. Tech. Pap. **45**(1), 385-388 (2014).

[15] K. Ohmuro, S. Kataoka, T. Sasaki, and Y. Koike, "Development of super-high-image-quality vertical-alignment-mode LCDs," SID Symp. Dig. Tech. Pap. **28**(1), 845-848 (1997).

[16] A. Takeda, S. Kataoka, T. Sasaki, H. Chida, H. Tsuda, K. Ohmuro, T. Sasabayashi, Y. Koike, and K. Okamoto, "A Super-high image quality multi-domain vertical alignment LCD by new rubbing-less technology," SID Symp. Dig. Tech. Pap. **29**(1), 1077-1080 (1998).

[17] K. H. Kim, K. Lee, S. B. Park, J. K. Song, S. N. Kim, and J. H. Souk, "Domain divided vertical alignment mode with optimized fringe field effect," Proc. Asia Display **98**, 383-386 (1998).

[18] S. H. Lee, S. M. Kim, and S. T. Wu, "Emerging vertical-alignment liquid-crystal technology associated with surface modification using UV-curable monomer," J. Soc. Inf. Disp. **17**(7), 551-559 (2009).

[19] S. S. Kim, B. H. You, J. H. Cho, D. G. Kim, B. H. Berkeley, and N. D. Kim, "An 82-in. ultra-definition 120-Hz LCD TV using new driving scheme and advanced Super PVA technology," J. Soc. Inf. Disp. **17**(2), 71-78 (2009).

[20] K. H. Vepakomma, T. Ishikawa, and R. G. Greene, "Stress induced substrate mura in curved LCD," SID Symp. Dig. Tech. Pap. **46**(1), 634-636 (2015).

[21] K. Hsiao, G. Tang, G. Yu, Z. Zhang, X. Xu, P. Zhang, C. Lv, and A. Lien, "Development and analysis of technical challenges in the world's largest (110-in.) curved LCD," SID Symp. Dig. Tech. Pap. **46**(1), 1059-1062 (2015).

[22] M. Oh-e and K. Kondo, "Electro-optical characteristics and switching behavior of the in-plane switching mode," Appl. Phys. Lett. **67**(26), 3895-3897 (1995).

[23] M. Oh-e and K. Kondo, "Response mechanism of nematic liquid crystals using the in-plane switching mode," Appl. Phys. Lett. **69**(5), 623-625 (1996).

[24] S. H. Hong, I. C. Park, H. Y. Kim, and S. H. Lee, "Electro-optic characteristic of fringe-field switching mode depending on rubbing direction," Jpn. J. Appl. Phys. **39**(6A), L527 (2000).

[25] I. H. Yu, I. S. Song, J. Y. Lee, and S. H. Lee, "Intensifying the density of a horizontal electric field to improve light efficiency in a fringe-field switching liquid crystal display," Jpn. J. Appl. Phys. **39**(11), 2367 (2006).

[26] H. Chen, F. Peng, Z. Luo, D. Xu, S.T. Wu, M.C. Li, S.L. Lee, and W.C. Tsai, "High performance liquid crystal displays with a low dielectric constant material," Opt. Mater. Express **4**(11), 2262-2273 (2014).

[27] H. J. Yun, M. H. Jo, I. W. Jang, S. H. Lee, S. H. Ahn, and H. J. Hur, "Achieving high light efficiency and fast response time in fringe field switching mode using a liquid crystal with negative dielectric anisotropy," Liq. Cryst. **39**(9), 1141-1148 (2012).

[28] H. Chen, Y. Gao, and S. T. Wu, "n-FFS vs. p-FFS: Who wins?" SID Symp. Dig. Tech. Pap. **46**(1), 735-738 (2015).

[29] Y. Chen, Z. Luo, F. Peng, and S. T. Wu, "Fringe-field switching with a negative dielectric anisotropy liquid crystal," J. Display Technol. **9**(2), 74-77 (2013).

[30] J. K. Yoon, E. M. Park, J. S. Son, H. W. Shin, H. E. Kim, M. Yee, H. G. Kim, C. H. Oh, and B. C. Ahn, "The study of picture quality of OLED TV with WRGB OLEDs structure," SID Symp. Dig. Tech. Pap. **44**(1), 326-329 (2013).

[31] M. Anandan, "Progress of LED backlights for LCDs," J. Soc. Inf. Displ. **16**(2), 287-310 (2008).

[32] H. T. Huang, Y. P. Huang, and C. C. Tsai, "Planar lighting system using array of blue LEDs to excite yellow remote phosphor film," J. Disp. Technol. **7**(1), 44-51 (2011).

[33] H. Chen, J. He, and S. T. Wu, "Recent advances on quantum-dot-enhanced liquid crystal displays," IEEE J. Sel. Topics Quantum Electron. **23**(5), 1900611 (2017).

[34] R. J. Xie, N. Hirosaki, and T. Takeda, "Wide color gamut backlight for liquid crystal displays using three-band phosphor-converted white light-emitting diodes," Appl. Phys. Express **2**(2), 022401 (2009).

[35] L. Wang, X. Wang, T. Kohsei, K. Yoshimura, M. Izumi, N. Hirosaki, and R. J. Xie, "Highly efficient narrowband green and red phosphors enabling wider color-gamut LED backlight for more brilliant displays," Opt. Express **23**(22), 28707-28717 (2015).

[36] T. Yamamoto, Y. Aono, and M. Tsumura, "Guiding principles for high quality motion picture in AMLCDs applicable to TV monitors," SID Symp. Dig. Tech. Pap. **31**(1), 456-459 (2000).

[37] T. Kurita, "Moving picture quality improvement for hold-type AM-LCDs," SID Symp. Dig. Tech. Pap. **32**(1), 986-989 (2001).

[38] Y. Igarashi, T. Yamamoto, Y. Tanaka, J. Someya, Y. Nakakura, M. Yamakawa, Y. Nishida, and T. Kurita, "Summary of moving picture response time (MPRT) and futures," SID Symp. Dig. Tech. Pap. **35**(1), 1262-1265 (2004).

[39] J. Someya and H. Sugiura, "Evaluation of liquid-crystal-display motion blur with moving-picture response time and human perception," J. Soc. Inf. Disp. **15**(1), 79-86 (2007).

[40] F. Peng, H. Chen, F. Gou, Y. H. Lee, M. Wand, M.C. Li, S.L. Lee, and S. T. Wu, "Analytical equation for the motion picture response time of display devices," J. Appl. Phys. **121**(2), 023108 (2017).

[41] H. Chen, F. Peng, F. Gou, Y. H. Lee, M. Wand, and S. T. Wu, "Nematic LCD with motion picture response time comparable to organic LEDs," Optica **3**(9), 1033-1034 (2016).

[42] S. T. Wu, U. Efron, and L. D. Hess, "Birefringence measurements of liquid crystals," Appl. Opt. **23**(21), 3911-3915 (1984).

[43] I. Haller, "Thermodynamic and static properties of liquid crystals," Prog. Solid State Chem. **10**(2), 103-118 (1975).

[44] S. T. Wu, "Birefringence dispersions of liquid crystals," Phys. Rev. A **33**(2), 1270-1274 (1986).

[45] S. T. Wu and C. S. Wu, "Rotational viscosity of nematic liquid crystals A critical examination of existing models," Liq. Cryst. **8**(2), 171-182 (1990).

[46] W. H. De Jeu, "Physical properties of liquid crystalline materials in relation to their applications," Mol. Cryst. Liq. Cryst. (Phila. Pa.) **63**(1), 83-109 (1981).

[47] S. T. Wu and C. S. Wu, "Experimental confirmation of the Osipov-Terentjev theory on the viscosity of nematic liquid crystals," Phys. Rev. A **42**(4), 2219-2227 (1990).

[48] S. T. Wu, "Nematic liquid crystal modulator with response time less than 100 μs at room temperature," Appl. Phys. Lett. **57**(10), 986-988 (1990).

[49] J. H. Lee, D. N. Liu, and S. T. Wu. *Introduction to Flat Panel Displays*. John Wiley & Sons, 2008.

[50] J. I. Hirakata, A. Shingai, Y. Tanaka, K. Ono, and T. Furuhashi, "Super-TFT-LCD for moving picture images with the blink backlight system," SID Symp. Dig. Tech. Pap. **32**(1), 990-993 (2001).

[51] T. Furuhashi, K. Kawabe, J. I. Hirakata, Y. Tanaka, and T. Sato, "High quality TFT-LCD system for moving picture," SID Symp. Dig. Tech. Pap. **33**(1), 1284-1287 (2002).

[52] T. Yamamoto, S. Sasaki, Y. Igarashi, and Y. Tanaka, "Guiding principles for high-quality moving picture in LCD TVs," J. Soc. Inf. Disp. **14**(10) 933-940, 2006.

[53] H. Chen, F. Penga, F.Goua, M. Wand, and S. T. Wu, "Fast-response LCDs for virtual reality applications," Proc. SPIE **10125**, 101251E-1 (2017).

[54] Y. Iwata, M. Murata, K. Tanaka, T. Ohtake, H. Yoshida, and K. Miyachi, "Novel super fast response vertical alignment-liquid crystal display with extremely wide temperature range," J. Soc. Inf. Disp. **22**(1), 35-42 (2014).

[55] J. W. Park, Y. J. Ahn, J. H. Jung, S. H. Lee, R. Lu, H. Y. Kim, and S. T. Wu, "Liquid crystal display using combined fringe and in-plane electric fields," Appl. Phys. Lett. **93**(8), 081103 (2008).

[56] A. Lien, "Extended Jones matrix representation for the twisted nematic liquid-crystal display at oblique incidence," Appl. Phys. Lett. **57**(26), 2767-2769 (1990).

[57] H. Okumura and H. Fujiwara, "A new low-image-lag drive method for large-size LCTVs," J. Soc. Inf. Disp. **1**(3), 335-339 (1993).

[58] M. Baba, G. Itoh, and H. Okumura, "Software-processed edge-and level-adaptive overdrive (SELAO) method for high-quality motion pictures," J. Soc. Inf. Disp. **15**(3), 205-211 (2007).

[59] C. H. Chen, F. C. Lin, Y. T. Hsu, Y. P Huang, and H. P. Shieh, "A field sequential color LCD based on color fields arrangement for color breakup and flicker reduction," J. Disp. Technol. **5**(1), 34-39 (2009).

[60] F. C. Lin, Y. P. Huang, C. M. Wei, and H. P. Shieh, "Color-breakup suppression and low-power consumption by using the Stencil-FSC method in field-sequential LCDs," J. Soc. Inf. Disp. **17**(3), 221-228 (2009).

[61] S. S. Kim, B. H. Berkeley, K. H. Kim, and J. K. Song, "New technologies for advanced LCD-TV performance," J. Soc. Inf. Disp. **12**(4), 353-359 (2004).

[62] H. Kikuchi, M. Yokota, Y. Hisakado, H. Yang, and T. Kajiyama, "Polymer-stabilized liquid crystal blue phases," Nat. Mater. **1**(1), 64-68 (2002).

[63] J. Yan, L. Rao, M Jiao, Y. Li, H. C. Cheng, and S. T. Wu, "Polymer-stabilized optically isotropic liquid crystals for next-generation display and photonics applications," J. Mater. Chem. **21**(22), 7870-7877 (2011).

[64] C.D. Tu, C.L. Lin, J. Yan, Y. Chen, P.C. Lai, and S. T. Wu, "Driving scheme using bootstrapping method for blue-phase LCDs," J. Disp. Technol. **9**(1), 3-6 (2013).

[65] C. L. Lin, C. D. Tu, M. H. Cheng, C. C. Hung, C. H. Lin, and N. Sugiura, "Novel dual-coupling pixel circuit to achieve high transmittance of blue-phase liquid crystal," IEEE Electron Device Lett. **36**(4), 354-356 (2015).

[66] L. Rao, J. Yan, S. T. Wu, S. Yamamoto, and Y. Haseba, "A large Kerr constant polymer-stabilized blue phase liquid crystal," Appl. Phys. Lett. **98**(8), 081109 (2011).

[67] M. Wittek, N. Tanaka, D. Wilkes, M. Bremer, D. Pauluth, J. Canisius, A. Yeh, R. Yan, K. Skjonnemand, and M. Klasen-Memmer, "New materials for polymer-stabilized blue phase," SID Symp. Dig. Tech. Pap. **43**(1), 25-28 (2012).

[68] Y. Haseba, S. I. Yamamoto, K. Sago, A. Takata, and H. Tobata, "Low-voltage polymer-stabilized blue-phase liquid crystals," SID Symp. Dig. Tech. Pap. **44**(1), 254-257 (2013).

[69] Y. Chen, D. Xu, S.T. Wu, S. Yamamoto, and Y. Haseba, "A low voltage and submillisecond-response polymer-stabilized blue phase liquid crystal," Appl. Phys. Lett. **102**(14), 141116 (2013).

[70] C. Y. Tsai, F. C. Yu, Y. F. Lan, P. J. Huang, S. Y. Lin, Y. T. Chen, T. I. Tsao, C. T. Hsieh, B. S. Tseng, C. W. Kuo, and C. H. Lin, "A novel blue phase liquid crystal display applying wall-electrode and high driving voltage circuit," SID Symp. Dig. Tech. Pap. **46**(1), 542-544 (2015).

[71] J. Yan, H. C. Cheng, S. Gauza, Y. Li, M. Jiao, L. Rao, and S. T. Wu, "Extended Kerr effect in polymer-stabilized blue-phase liquid crystals," Appl. Phys. Lett. **96**(7), 071105 (2010).

[72] S. Yoon, M. Kim, M. S. Kim, B. G. Kang, M. K. Kim, A. K. Srivastava, S. H. Lee, Z. Ge, L. Rao, S. Gauza, and S. T. Wu, "Optimization of electrode structure to improve the electro-optic characteristics of liquid crystal display based on Kerr effect," Liq. Cryst. **37**(2), 210-208 (2010).

[73] T. Yamamoto, M. Ikenaga, A. Yamashita, D. Kubota, M. Nakano, T. Ishitani, H. Shishido, Y. Hirakata, S. Yamazaki, R. Sato, and K. Okazaki, "Crystalline OS-LCD using blue-phase liquid crystal having characteristic texture," SID Symp. Dig. Tech. Pap. **43**(1), 201-204 (2012).

[74] L. Rao, Z. Ge, and S. T. Wu, "Zigzag electrodes for suppressing the color shift of Kerr effect-based liquid crystal displays," J. Disp. Technol. **6**(4), 115-120 (2010).

[75] E. Jang, S. Jun, H. Jang, J. Lim, B. Kim, and Y. Kim, "White-light-emitting diodes with quantum dot color converters for display backlights," Adv. Mater. **22**(28), 3076-3080 (2010).

[76] Z. Luo, D. Xu, and S. T. Wu, "Emerging quantum-dots-enhanced LCDs," J. Disp. Technol. **10**(7), 526-539 (2014).

[77] R. Zhu, Z. Luo, H. Chen, Y. Dong, and S. T. Wu, "Realizing Rec. 2020 color gamut with quantum dot displays," Opt. Express **23**(18), 23680-23693 (2015).

[78] J. S. Steckel, J. Ho, C. Hamilton, J. Xi, C. Breen, W. Liu, P. Allen, and S. Coe-Sullivan, "Quantum dots: The ultimate down-conversion material for LCD displays," J. Soc. Inf. Displ. **23**(7), 294-305 (2015).

[79] S. H. Lee, K. H. Lee, J. H. Jo, B. Park, Y. Kwon, H. S. Jang, and H. Yang, "Remote-type, high-color gamut white light-emitting diode based on InP quantum dot color converters," Opt. Mater. Express **4**(7), 1297-1302 (2014).

[80] N. L. Pickett, N. C. Gresty, and M. A. Hines, "Heavy metal-free quantum dots making inroads for consumer applications," SID Symp. Dig. Tech. Pap. **47**(1), 425-427 (2016).

[81] J. Chen, V. Hardev, J. Hartlove, J. Hofler, and E. Lee, "High-efficiency wide-color-gamut solid-state backlight system for LCDs using quantum dot enhancement film," SID Symp. Dig. Tech. Pap. **43**(1), 895-896 (2012).

[82] N. Hirosaki, R. J. Xie, K. Kimoto, T. Sekiguchi, Y. Yamamoto, T. Suehiro, and M. Mitomo, "Characterization and properties of green-emitting β-SiAlON:Eu^{2+} powder phosphors for white light-emitting diodes," Appl. Phys. Lett. **86**(21), 211905 (2005).

[83] R. J. Xie, N. Hirosaki, H. L. Li, Y. Q. Li, and M. Mitomo, "Synthesis and photoluminescence properties of β- sialon:Eu^{2+} ($Si_{6-z}Al_zO_zN_{8-z}$:Eu^{2+}) - A promising green oxynitride phosphor for white light-emitting diodes," J. Electrochem. Soc. **154**(10), J314-J319 (2008).

[84] S. Adachi and T. Takahashi, "Direct synthesis and properties of K_2SiF_6:Mn^{4+} phosphor by wet chemical etching of Si wafer," J. Appl. Phys. **104**(2), 023512 (2008).

[85] T. Takahashi and S. Adachi, "Synthesis of K_2SiF_6:Mn^{4+} red phosphor from silica glasses by wet chemical etching in HF/KMnO4 solution," Electrochem. Solid-State Lett. **12**(8), J69-J71 (2009).

[86] J. E. Murphy, F. Garcia-Santamaria, A. A. Setlur, and S. Sista, "PFS, K_2SiF_6: Mn^{4+}: the red-line emitting LED phosphor behind GE's TriGain Technology™ platform," SID Symp. Dig. Tech. Pap. **46**(1), 927-930 (2015).

[87] H. Chen, R. Zhu, G. Tan, M.C. Li, S.-L. Lee, and S. T. Wu, "Enlarging the color gamut of liquid crystal displays with a functional reflective polarizer," Opt. Express **25**(1), 102-111 (2017).

[88] M. F. Weber, C. A. Stover, L. R. Gilbert, T. J. Nevitt, and A. J. Ouderkirk, "Giant birefringent optics in multilayer polymer mirrors," Science **287**(5462), 2451-2456 (2000).

[89] Y. Li, T. X. Wu, and S.-T. Wu, "Design optimization of reflective polarizers for LCD backlight recycling," J. Disp. Technol. **5**(8), 335-340 (2009).

[90] R. Zhu, G. Tan, J. Yuan, and S. T. Wu, "Functional reflective polarizer for augmented reality and color vision deficiency," Opt. Express **24**(5), 5431-441 (2016).

[91] K. Käläntär, "A directional backlight with narrow angular luminance distribution for widening the viewing angle for an LCD with a front-surface light-scattering film," J. Soc. Inf. Displ. **20**(3), 133-142 (2012).

[92] R. Zhu, Q. Hong, Y. Gao, Z. Luo, S. T. Wu, M. C. Li, S. L. Lee, and W. C. Tsai, "Tailoring the light distribution of liquid crystal display with freeform engineered diffuser," Opt. Express **23**(11), 14070-14084 (2015).

[93] Y. Gao, Z. Luo, Z. Zhu, Q. Hong, S. T. Wu, M. C. Li, S. L. Lee, and W. C. Tsai, "A high performance singledomain LCD with wide luminance distribution," J. Disp. Technol. **11**(4), 315-324 (2015).

[94] E. K. Macdonald and M. P. Shaver, "Intrinsic high refractive index polymers," Polym. Int. **64**(1), 6-14 (2015).

[95] Y. Wang, J. He, H. Chen, J. Chen, R. Zhu, P. Ma, A. Towers, Y. Lin, A. J. Gesquiere, S. T. Wu, and Y. Dong, "Ultrastable, highly luminescent organic-inorganic Perovskite-polymer composites," Adv. Mater. **28**(48), 10710-10717 (2016).

[96] Q. Zhou, Z. Bai, W. G. Lu, Y. Wang, B. Zou, and H. Zhong, "In situ fabrication of halide perovskite nanocrystal-embedded polymer composite films with enhanced photoluminescence for display backlights," Adv. Mater. **28**(41), 9163-9168 (2016).

[97] J. Chen, S. Gensler, J. Hartlove, J. Yurek, E. Lee, J. Thielen, J. Van Derlofske, J. Hillis, G. Benoit, J. Tibbits, and A. Lathrop, "Quantum dots: optimizing LCD systems to achieve Rec. 2020 color performance," SID Symp. Dig. Tech. Pap. **46**(1), 173-175 (2015).

[98] H. Chen, R. Zhu, J. He, W. Duan, W. Hu, Y.Q. Lu, M. C. Li, S. L. Lee, Y. Dong, and S. T. Wu, "Going beyond the limit of an LCD's color gamut," Light Sci. Appl. **6**(9), e17043 (2017).

[99] C. A. C. Coello and G. B. Lamont. *Applications of Multi-Objective Evolutionary Algorithms.* World Scientific, 2004.

[100] M. Schadt, K. Schmitt, V. Kozinkov, and V. G. Chigrinov, "Surface-induced parallel alignment of liquid crystals by linearly polymerized photopolymers," Jpn. J. Appl. Phys. **31**(7R), 2155-2164 (1992).

[101] V. G. Chigrinov, V. M. Kozenkov, and H. S. Kwok. *Photoalignment of Liquid Crystalline Materials: Physics and Applications.* John Wiley & Sons, 2008.

[102] Y. Utsumi, I. Hiyama, Y. Tomioka, K. Kondo, and S. Matsuyama, "Analysis of light leakage caused by color filter between crossed polarizers," Jpn. J. Appl. Phys. **46**(3R), 1047-1050 (2007).

[103] Y. Utsumi, S. Takeda, I. Hiyama, Y. Tomioka, M. Ishii, and K. Ono, "Light leakage behaviors of homogenously aligned liquid crystal layers placed between crossed polarizers," Jpn. J. Appl. Phys. **47**(4R), 2144-2148 (2008).

[104] K. Sumiyoshi, "Light leakage analysis of in-plane-switching liquid crystal displays," Jpn. J. Appl. Phys. **48**(2R), 121601 (2009).

[105] Y. Utsumi, D. Kajita, S. Takeda, H. Kagawa, I. Hiyama, Y. Tomioka, and K. Ono, "Correlation of light scattering of homogenous alignment liquid crystal layers with material properties of liquid crystals," Jpn. J. Appl. Phys. **47**(4R), 2205-2208 (2008).

[106] Y. Utsumi, I. Hiyama, Y. Tomioka, and K. Ono, "Quantitative analysis method for measuring light leakage intensity of three primary color filters placed between crossed polarizers," Jpn. J. Appl. Phys. **47**(5R), 3518-3521 (2008).

[107] J. S. Hsu, Y. H. Lin, H. C. Lin, and K. H. Yang, "Thermally induced light leakage in in-plane-switching liquid crystal displays," J. Appl. Phys. **105**(3), 033503 (2009).

[108] J. S. Park, "Contrast ratio of colorant film: Theoretical consideration and effect of polymeric binder," J. Appl. Polym. Sci. **117**(1), 428-433 (2010).

[109] M. Akimoto, J. Iwakawa, N. Kobayashi, S. Kobayashi, and K. Takatoh, "Evaluation of liquid crystal alignment ability of polyimide by analyzing the black state of homogeneous alignment liquid crystal display," Mol. Cryst. Liq. Cryst. **543**(1), 69-835 (2011).

[110] H. Takemoto, T. Fuchida, and M. Miyatake, "Analysis of depolarized light-scattering in LCD panel and proposal of LCD systems for enhancing contrast ratio," SID Symp. Dig. Tech. Papers **40**(1), 514-517 (2009).

[111] Y. Utsumi, S. Takeda, H. Kagawa, D. Kajita, I. Hiyama, Y. Tomioka, T. Asakura, M. Shimura, M. Ishii, K. Miyazaki, and K. Ono, "Improved contrast ratio in IPS-Pro LCD TV by using quantitative analysis of depolarized light leakage from component materials," SID Symp. Dig. Tech. Papers **39**(1), 129-132 (2008).

[112] K. J. Kim, T. R. Lee, H. H. Son, D. K. Kim, J. H. Baek, J. H. Kim, and M. Jun, "Realization of true black quality in in-plane switching mode for LCD TV applications," SID Symp. Dig. Tech. Papers **41**(1), 487-490 (2010).

[113] K. Okumoto, T. Tsuchiya, K. Yonemura, S. Nagano, O. Tanina, A. Yuuki, T. Fujino, and T. Satake, "A novel simulation method in in-plane switching mode panel with considering light scattering behavior," SID Symp. Dig. Tech. Papers **46**(1), 1555-1558 (2015).

[114] H. Chen, G. Tan, M. C. Li, S. L. Lee, and S. T. Wu, "Depolarization effect in liquid crystal displays," Opt. Express **25**(10), 11315-11328 (2017).

[115] M. Yoneya, Y. Utsumi, and Y. Umeda, "Depolarized light scattering from liquid crystals as a factor for black level light leakage in liquid-crystal displays," J. Appl. Phys. **98**(1), 016106 (2005).

[116] R. Lu, Q. Hong, S. T. Wu, K. H. Peng, and H. S. Hsieh, "Quantitative comparison of color performances between IPS and MVA LCDs," J. Disp. Technol. **2**(4), 319-326 (2006).

[117] Y. Ukai, T. Ohyama, L. Fennell, Y. Kato, M. Paukshto, P. Smith, O. Yamashita, and S. Nakanishi, "Current status and future prospect of in-cell-polarizer technology," J. Soc. Inf. Disp. **13**(1), 17-24 (2005).

[118] S. H. Kim, J. D. Park, and K. D. Lee, "Fabrication of a nano-wire grid polarizer for brightness enhancement in liquid crystal display," Nanotechnology **17**(17), 4436-4438 (2006).

[119] Z. Ge and S. T. Wu, "Nanowire grid polarizer for energy efficient and wide-view liquid crystal displays," Appl. Phys. Lett. **93**(12), 121104 (2008).

[120] F. Yamada, H. Nakamura, Y. Sakaguchi, and Y. Taira, "Sequential-color LCD based on OCB with an LED backlight," J. Soc. Inf. Disp. **10**(1), 81-85 (2002).

[121] E. Reinhard, W. Heidrich, P. Debevec, S. Pattanaik, G. Ward, and K. Myszkowski. *High Dynamic Range Imaging: Acquisition, Display, and Image-Based Lighting.* Morgan Kaufmann, 2010.

[122] J. U. Kwon, S. Bang, D. Kang, and J. J. Yoo, "The required attribute of displays for high dynamic range," SID Symp. Dig. Tech. Pap. **47**(1), 884-887 (2016).

[123] R. Zhu, H. Chen, and S. T. Wu, "Achieving 12-bit perceptual quantizer curve with liquid crystal display," Opt. Express **25**(10), 10939-10946 (2017).

[124] H. Chen, J. Sung, T. Ha, Y. Park, and C. Hong, "Backlight local dimming algorithm for high contrast LCD-TV," Proc. ASID **6**, 168-171 (2006).

[125] F. C. Lin, Y. P. Huang, L. Y. Liao, C. Y. Liao, H. P. D. Shieh, T. M. Wang, and S. C. Yeh, "Dynamic backlight gamma on high dynamic range LCD TVs," J. Disp. Technol. **4**(2), 139-146 (2008).

[126] H. Chen, T. H. Ha, J. H. Sung, H. R. Kim, and B. H. Han, "Evaluation of LCD local-dimming-backlight system," J. Soc. Inf. Disp. **18**(1), 57-65 (2010).

[127] O. Yoo, S. Nam, J. Choi, S. Yoo, K. J. Kim, J. Kim, D. Lee, J. Lee, and M. C. Jun, "Contrast enhancement based on advanced local dimming system for high dynamic range LCDs," SID Symp. Dig. Tech. Pap. **48**(1), 1667-1669 (2017).

[128] Y. Kitagawa, H. Ikeno, S. Uehara, and T. Yatsushiro, "Dual panel liquid crystal display device," U.S. Patent 7,916,223 (2011).

[129] H. Chen, R. Zhu, M. C. Li, S. L. Lee, and S. T. Wu, "Pixel-by-pixel local dimming for high-dynamic-range liquid crystal displays," Opt. Express **25**(3), 1973-1984 (2017).